Molecular Beam Epitaxial Growth of Monocrystalline $Mg_xCd_{1-x}Te/Mg_yCd_{1-y}Te$ ($x<y$) Double Heterostructures and Solar Cells

by

Calli Michele Campbell

A Dissertation Presented in Partial Fulfillment
of the Requirements for the Degree
Doctor of Philosophy

Approved April 2019 by the
Graduate Supervisory Committee

Yong-Hang Zhang, Chair
Candace K. Chan
Richard R. King

ARIZONA STATE UNIVERSITY

May 2019

ABSTRACT

This dissertation details a study of wide-bandgap molecular beam epitaxy (MBE)-grown single-crystal $Mg_xCd_{1-x}Te$. The motivation for this study is to open a pathway to reduced $/W solar power generation through the development of a high-efficiency 1.7-eV II-VI top cell current-matched to low-cost 1.1-eV silicon. This paper reports the demonstration of monocrystalline 1.7-eV $Mg_xCd_{1-x}Te/Mg_yCd_{1-y}Te$ (y>x) double heterostructures (DHs) with a record carrier lifetime of 560 nanoseconds, along with a 1.7-eV $Mg_xCd_{1-x}Te/Mg_yCd_{1-y}Te$ (y>x) single-junction solar cell with a record active-area efficiency of 15.2% and a record open-circuit voltage (V_{OC}) of 1.176 V. A study of indium-doped n-type 1.7-eV $Mg_xCd_{1-x}Te$ with a carrier activation of up to 5×10^{17} cm^{-3} is presented with promise to increase device V_{OC}. Finally, this paper reports an epitaxial lift-off (ELO) technology using water-soluble MgTe for the creation of free-standing MBE-grown II-VI single-crystal CdTe and 1.7-eV $Mg_xCd_{1-x}Te$ solar cells freed from lattice-matched InSb(001) substrates. Photoluminescence (PL) spectroscopy measurements comparing intact and free-standing films reveal the survival of optical quality in CdTe DHs after ELO. This technology opens up several possibilities to drastically increase cell conversion efficiency through improved light management and transferability into monolithic multijunction devices. Lastly, this report will present considerations for future work in each of the study areas mentioned above.

ACKNOWLEDGEMENTS

I would first and foremost like to thank my parents, Linda and Doug. They have been with me from the beginning, and none of my achievements would be possible without their love and support. I would next like to thank my Arizona family: my amazing boyfriend Wen-Cheng and my wonderful friend Sarah. It has been a joy to watch them grow and succeed as they inspired and supported me through this journey. I would next like to thank my seniors, Dr. Michael DiNezza, Dr. Shi Liu, Dr. Preston Webster, Dr. Jacob Becker, Dr. Xin-Hao Zhao and Dr. Yuan Zhao for guiding me through my first couple of years and turning me into a relatively competent and level-headed MBE grower and researcher. I would like to thank my current labmates, Cheng-Ying Tsai, Jia Ding and Tyler McCarthy, for always offering advice or a helping hand whenever I needed it.

I would like to deeply thank my committee members: Dr. Candace Chan, Dr. Richard King and lastly, my advisor Dr. Yong-Hang Zhang, who saw my potential and has continued to nurture and support my growth as a curious and capable scientist.

I would like to thank our ASU collaborators who have provided invaluable team support; from the Zachary Holman Group: William Weigand, Zhengshan Yu and Jianwei Shi for device processing, from Mariana Bertoni's ASU Defect Lab: Tara Nietzold and Nicholas Theut for their electrochemical capacitance-voltage measurements and from the Robert Nemanich Group: Xingye Wang, for his expertise in X-ray Photoluminescence Spectroscopy.

I would like to acknowledge the funding agencies which have made this research possible, including the DOE Photovoltaic Research and Development program and the

Bay Area Photovoltaic Consortium. And last but certainly not least, I would like to thank my fur baby, Marble, for warming my lap as I write.

TABLE OF CONTENTS

Page

LIST OF TABLES

Table Page

LIST OF FIGURES

Figure Page

CHAPTER 1 – INTRODUCTION

1.1 Background of Cadmium Telluride and Silicon Photovoltaic Industries

In the past decades, greenhouse gas emissions have increased. Carbon dioxide, methane, nitrous oxide and fluorinated hydrocarbons (Fig. 1.1) are the byproducts of fossil fuel use[1] and affect the air, water and overall temperature of the Earth in ways which are unsustainable to the continued health and stability of the planet's atmosphere and inhabitants.

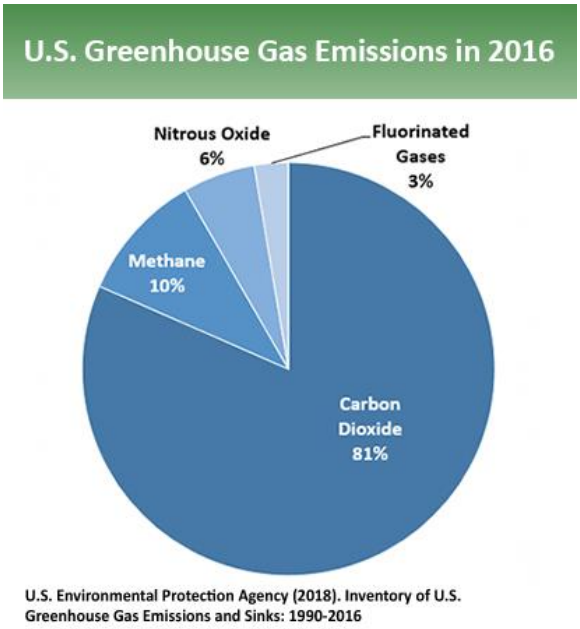

Fig. 1.1 A Breakdown of Greenhouse Gas Emissions Present in The Earth's Atmosphere.

The use of alternative sources of energy are essential in order to maintain and/or improve quality of life while sustaining the health of the environment for the benefit of future generations. Wind, nuclear (fusion and fission), hydroelectric and solar energy are alternatives to the combustion of fossil fuels. There are many sources of renewable

energy, each with their benefits and challenges. Wind power is a versatile option for small- or large-scale energy needs, however the rotating blades can cause injury to wildlife along noise pollution if too close to residential areas[2]. Hydroelectric power harnesses the renewable water cycle, and produces no harmful byproducts, however power plants are often far removed from civilization locations where the infrastructure diverts water currents; this can detrimentally affect an ecosystem's flora and fauna.[3] Biofuels, harnessing power from the combustion of organics like corn, grasses, and algae, are portable and storable for use in vehicles, however balance needs to be considered between energy crops and crops used for food[4]. Each of these energy sources, while viable for specific applications, have qualities which make their utilization challenging to widescale, global use.

For wide-scale deployment, photovoltaic (PV) solar energy is a renewable, highly-accessible and virtually unlimited resource. PV is can be integrated into uses as small as portable electronics or as large as metropolitan energy grids[3]. First-generation semiconductor-based solar cells were patented in 1946 by Russel Ohl from Bell Laboratories.[5] The cost of solar cells was at first prohibitive to wide-spread commercial use. The U.S. government's funding of solar cell research, first to provide power to satellites, helped to bolster the image and evolution of PV. In response to rising oil prices in the 1970's, both private and public sectors championed the increase in solar power generation and use.

In the 1970s, corporate-driven research dropped the cost of Si-based solar cells from $100/W to only $20-40/W while in parallel, the U.S. government passed solar-friendly bills including the Solar Energy Coordination and Management Project and created the

Energy Research and Development Administration and the Solar Energy Research Institute (now known as the National Renewable Energy Laboratory)[6]. Since then, PV technology has continued to drop in price to cater to a broad and varied number of terrestrial consumers.

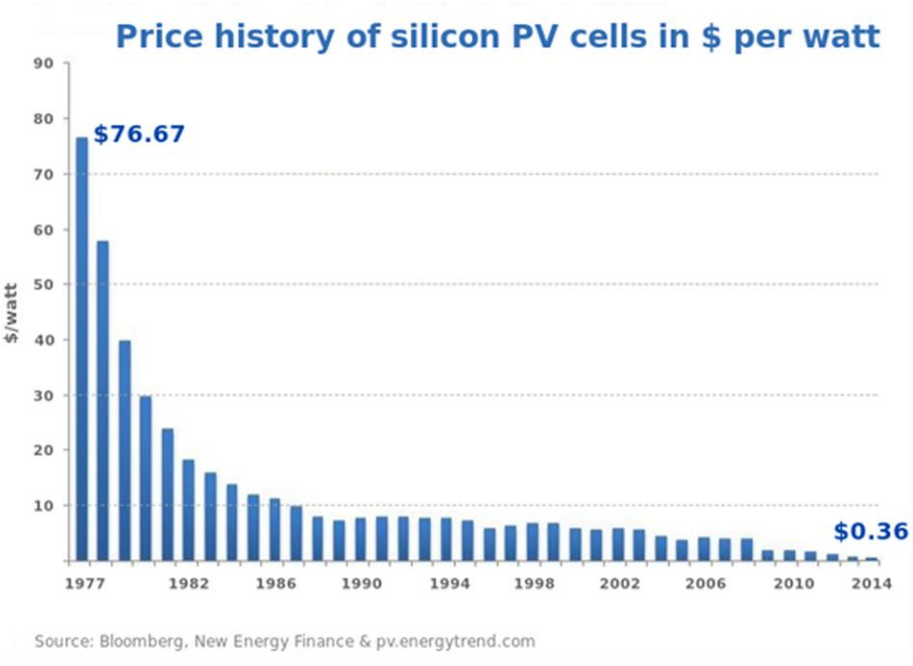

Fig. 1.2 A Look at The Steep Price Drop of Si Over 36 Years. *Bloomberg*

There are a multitude of different PV technologies being researched and manufactured, with materials ranging from perfect Group IV, III-V and II-VI single crystals to amorphous and organic films. A major goal for PV research is the continued reduction the dollar per watt ($/W) of PV energy, balancing out efficiency with cost and manufacturability. Silicon (Si) and Cadmium Telluride (CdTe) PV are two established, economical PV technologies.

Silicon is a powerhouse in the PV world. A practical Si solar cell was first fabricated in 1954 by Bell Laboratories, with an efficiency of 6%. Through the following decades, the manufacturability of Si has become more and more optimized and economical, aided by contribution from both the integrated circuit as well as PV industries. As a result, the $/W of a Si PV module has decreased by a factor of > 200 over only 4 decades (Fig. 1.2)[7].

Cadmium telluride (CdTe) is another powerhouse material in PV. CdTe is a semiconductor material with a bandgap of 1.5 eV, which primes this material for a near ideal absorption of the solar spectrum as shown in Section 1.2 below. CdTe is a direct-bandgap material which allows it to absorb a maximum amount of the solar spectrum within a relatively thin layer of film thickness. This thin-film solar cell material is incredibly manufacturable, allowing for the use of relatively cheap and quick processes, including closed space sublimation, to produce polycrystalline films which are fabricated into high-efficiency PV cells and modules. Over the years, as shown in Fig 1.3, research in private and public sectors has made and will make CdTe PV cheaper and cheaper, on par with that of Si.[8]

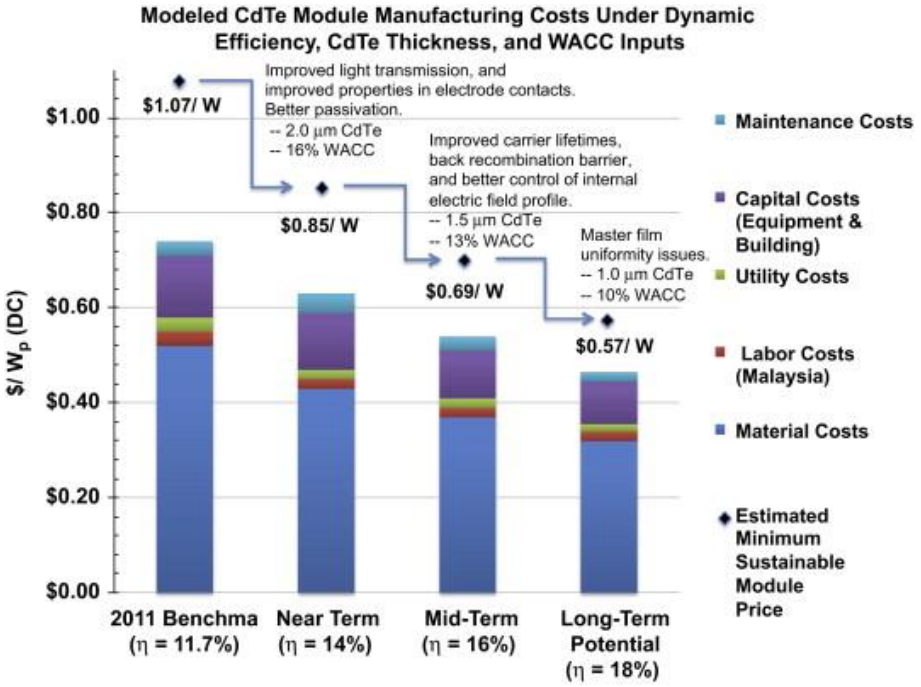

Fig. 1.3 Optimization and Subsequent Reduction in The Cost of CdTe PV Modules.[8]

A marriage of low-cost, high-efficiency CdTe and Si technologies shows incredible potential for low-cost, high-efficiency multijunction cells, which will be explain in further details in the following Sections 1.2 – 1.4.

1.2 Sunlight Absorption of a Photovoltaic Material and Device Operation

It first important to understand the basics of how a solar cell operates. A photovoltaic (PV) material is a semiconductor which absorbs incident photons from sunlight and converts these photons into electrical current. The AM1.5G absorption spectra (Fig. 1.4) is the standard depiction of the photons from the sun which shine through to atmosphere to be incident on the Earth's surface.[9]

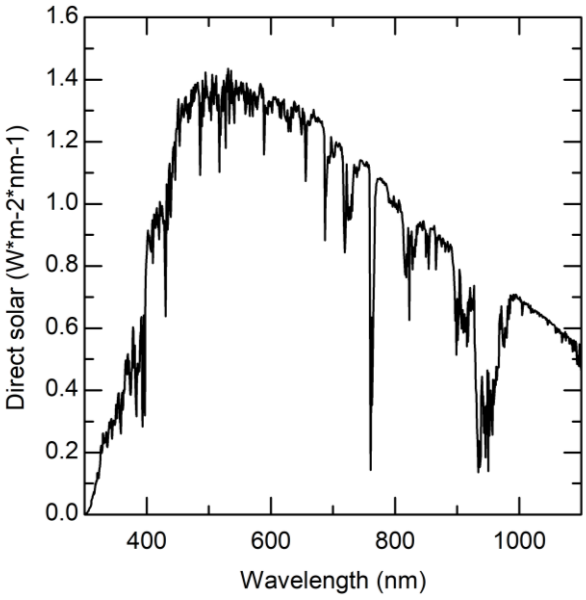

Fig. 1.4 A Depiction of The Irradiance Emitting from The Sun to The Earth's Surface.

The general equation for particle flux is:[10]

$$\varphi(E_a, E_b, \mu, T) = Cf\frac{2\pi}{h^3c^2}\int_{E_a}^{E_b}\frac{E^2}{\exp\left(\frac{E-\mu}{kT}\right)-1}dE \qquad (1.1)$$

where E_a is the low limit of the energy range, $E_b$is the high limit of the energy range, μ is the internal chemical potential, T is the system temperature, C is the correction factor, f is the fraction of the incident solar flux, h is Planck's constant, c is the speed of light, and k is Boltzmann's constant.

The absorption from the sun is given by:

$$\varphi_{sun}(E_G, \infty, 0, T_{sun}) = \frac{2\pi}{h^3c^2}\int_{E_G}^{\infty}\frac{E^2}{\exp\left(\frac{E}{kT_{sun}}\right)-1}dE \qquad (1.2)$$

The absorption from the Earth is given by:

$$\varphi_{Earth}(E_G, \infty, 0, T_{Earth}) = (1 - Cf)\frac{2\pi}{h^3c^2}\int_{E_G}^{\infty}\frac{E^2}{\exp\left(\frac{E}{kT_{Earth}}\right) - 1}dE \tag{1.3}$$

Ultimately the absorption of the solar cell is that of the sun subtracted by that of the Earth:

$$\begin{aligned}\varphi_1 &= \varphi_{sun} - \varphi_{Earth} \\ &= Cf\frac{2\pi}{h^3c^2}\int_{E_a}^{E_b}\frac{E^2}{\exp\left(\frac{E-\mu}{kT}\right) - 1}dE - (1 \\ &\quad - Cf)\frac{2\pi}{h^3c^2}\int_{E_G}^{\infty}\frac{E^2}{\exp\left(\frac{E}{kT_{Earth}}\right) - 1}dE\end{aligned} \tag{1.4}$$

$$\varphi_2(E_G, \infty, 0, T_{Earth}) = \frac{2\pi}{h^3c^2}\int_{E_G}^{\infty}\frac{E^2}{\exp\left(\frac{E-\mu}{kT_{Earth}}\right) - 1}dE \tag{1.5}$$

And finally, the detailed balance efficiency is:

$$\eta = \frac{P_{solar\ cell}}{P_{sun}} = \frac{q(\varphi_1 - \varphi_2)\mu}{\sigma T_{sun}^4} \tag{1.6}$$

where $P_{solar\ cell}$ is the power collected from a solar cell and P_{sun} is the incident power from the sun. A look at the detailed-balance efficiency as it corresponds to each bandgap is shown in Fig 1.5. The bandgap of CdTe holds potential to have one of the highest efficiencies of any single-junction cell.

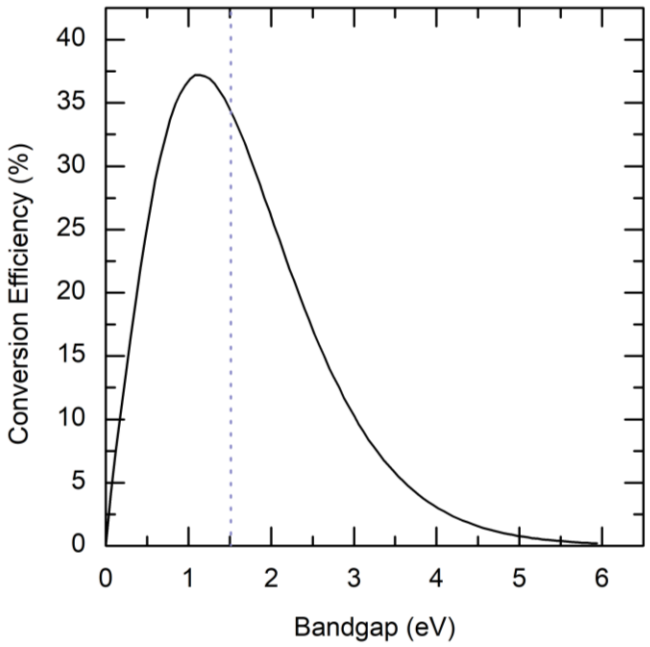

Fig. 1.5 The Detailed Balance Conversion Efficiency for Solar Cells of a Given Bandgap. Note That The Bandgap for CdTe (1.5 eV) is Close to The Peak Indicating That It Has a High Absorption Coefficient.

1.3 Operation of a P-N Junction Based Solar Cell

A PV material is able to transfer absorbed sunlight into electrical current by the formation of an electric field, commonly through a p-n junction device design. A basic p-n junction, shown below in Fig. 1.6, forms at the interface between an n-type and a p-type semiconductor material. Considering an ion core fixed to its lattice position in a materials, an n-type material has an excess of electrons surrounding positively-charged ion cores, while a p-type material has an excess of holes surrounding negatively-charged ion cores [11].

The joining of an n-type and p-type material elicits a balancing out of charges at the junction, forming a depletion region absent of excess carriers. The difference in potential

caused by a distribution of charge across this depletion region creates an electric field which drives the movement of carriers as electrical current in the device.

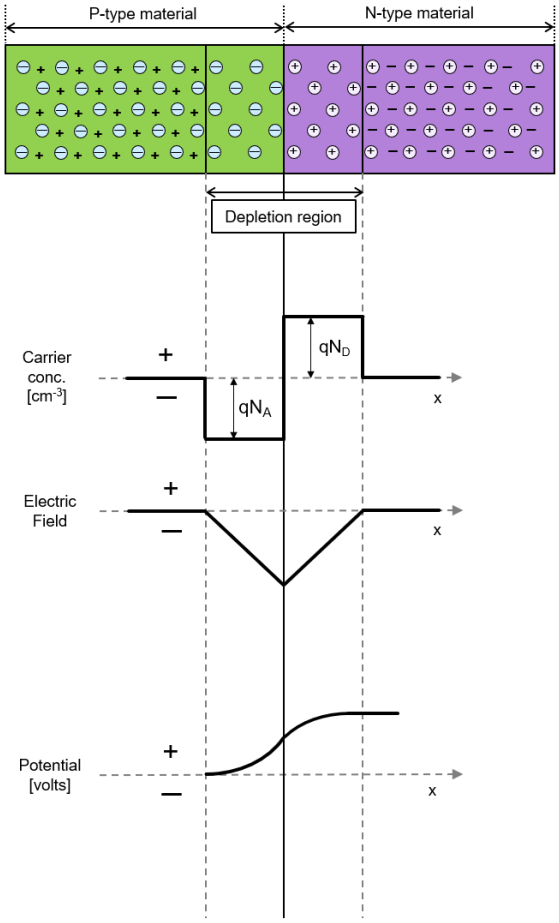

Fig. 1.6 Schematic of a P-N Junction.[11]

When probing the efficiency of a real solar cell, an AM1.5G sun simulator is incident on the cell. The voltage is swept, and the resulting current is collected and analyzed, appearing as a current-voltage curve like the green curve shown in Fig 1.7 below.

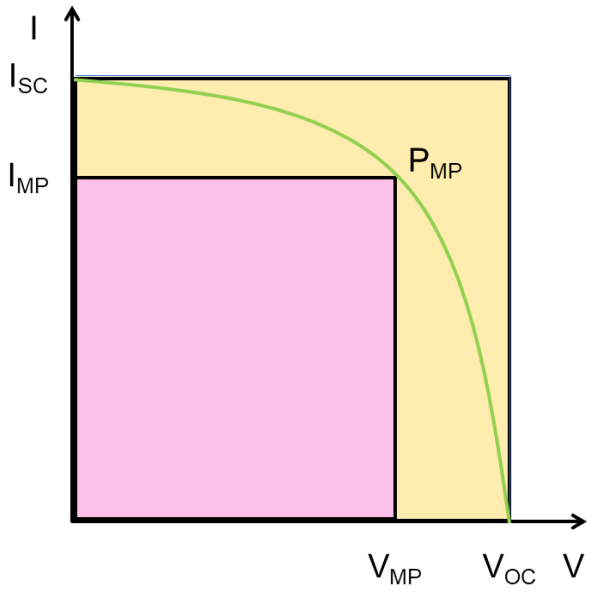

Fig. 1.7 A Breakdown of The Components of an I-V Measurement, Shown in Green.

The solar conversion efficiency is a result of three main parameters shown in the relationship below:

$$\eta = FF * I_{SC} * V_{OC} \tag{1.7}$$

where V_{OC} is the open-circuit voltage, I_{SC} is the short-circuit current, and FF is the fill-factor. The J_{SC}, or the maximum current from the device (at short circuit) divided by the device area, is described by the equation below:

$$J_{SC} = qG * (L_n + L_p) \tag{1.8}$$

where G is the generation rate of the cell and Ln,p is the diffusion length of excited carriers. As such, the value of the J_{SC} is heavily dependent upon the collected photon flux proportional to the generation of carriers, as well as the diffusion length of these generated carriers in order for them to be collected as current. The V_{OC}, or the maximum

voltage at zero current, is a feature of the quasi-Fermi level splitting within the cell seen by the equation:

$$V_{OC} = \frac{nkT}{q} \ln(\frac{I_L}{I_o} + 1) \quad (1.9)$$

where $\frac{kT}{q}$ is a constant (0.026 eV at room-temperature), I_L is light-generated current and I_o is the dark current. The fill factor is the "squareness" of the device I-V curve or:

$$FF = \frac{V_{OC} I_{SC}}{V_{MP} I_{MP}} \quad (1.9)$$

where V_{MP} is the voltage and I_{MP} the current at maximum measured power (P_{max}). The % value of the FF depends on a reduction in parasitic transport losses and a maximization of shunt resistances. The dependence of these parameters on device dimensions is further illuminated in Chapter 3.

1.4 Two-junction Tandem Devices

The theoretical efficiency of solar cells can be improved beyond the limits of single junction cells. This happens with the addition of more junctions with different bandgaps. As shown by Fig. 1.8, multiple bandgaps allow for an overlap of external quantum efficiencies (EQEs) for different wavelength ranges, thus boosting the overall EQE of the tandem device.[12]

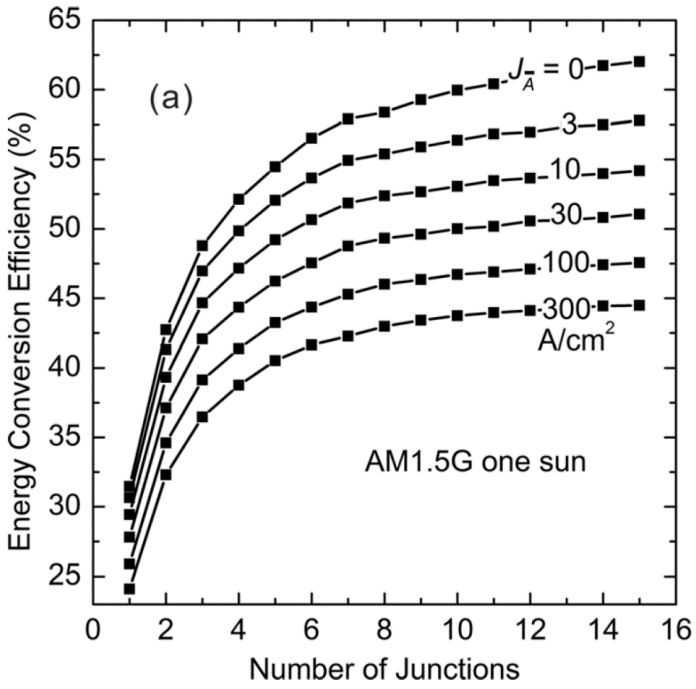

Fig. 1.8 Theoretical Efficiency Versus Number of Junctions.[13]

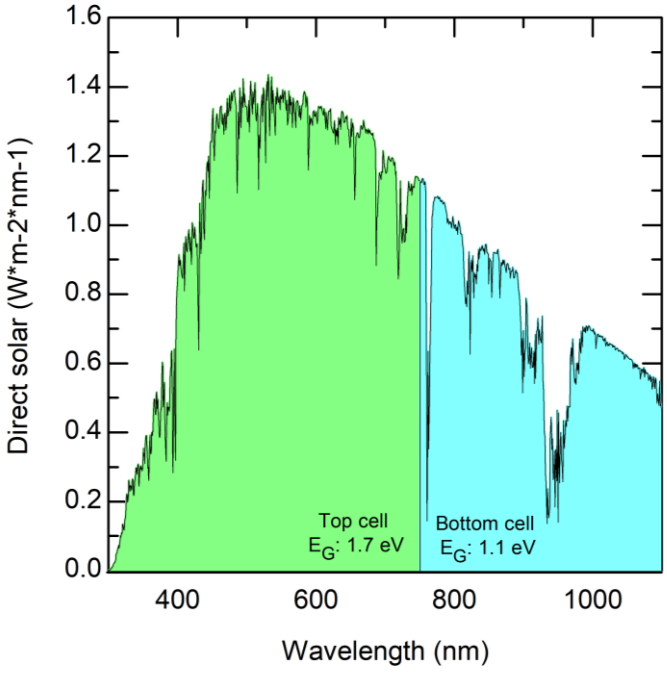

Fig. 1.9 Schematic of The Solar Spectra with Cut Offs at The Wavelengths Corresponding to 1.1-eV and 1.7-eV Bandgaps.[9]

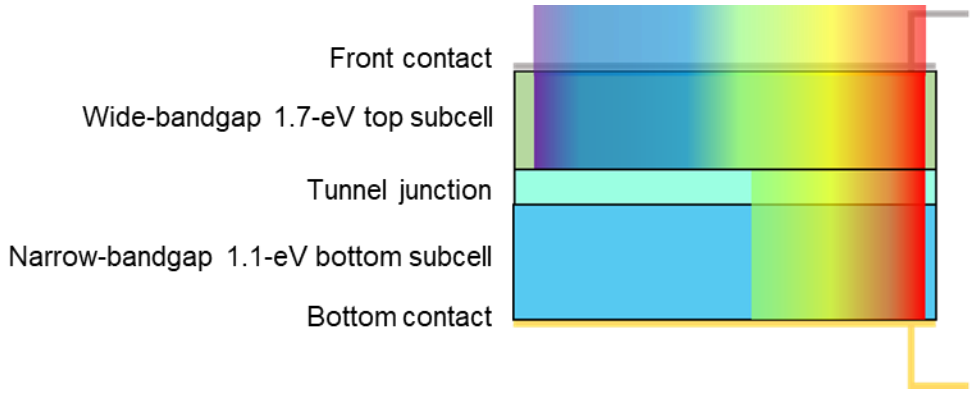

Fig. 1.10 Schematic of a Two-junction 1.7-eV/1.1-eV Tandem Device.

In a series configuration, voltage is additive while the short-circuit current is the same between devices. While the short circuit current of the bottom cells is limited by a reduction in incident photons absorbed by the top cell. An estimate of the total tandem cell efficiency is calculated by the addition of the bottom and top cell efficiency such as in the equation:

$$\eta_{Total} = \eta_{BC,1} * x + \eta_{TC} \tag{1.10}$$

where x is the factor by which the initial efficiency of the bottom cell ($\eta_{BC,1}$) is reduced from being covered by a top cell. An accurate J_{SC} can be calculated from:

$$J_{SC,BC,2} = \int_{1.1\ eV}^{1.7\ eV} EQE\ d\lambda \tag{1.11}$$

where the external quantum efficiency EQE of a device is integrated with respect to the wavelength of the solar spectrum. Since a 1.1-eV Si bottom cell is covered by a 1.7-eV II-VI top cell in a series-connected monolithic design, the photon collection of the Si cell only collects light that is not absorbed by the top cell. Thus, the J_{SC} of the

bottom cell needs to be integrated from at to above the wavelength which corresponds to the top cell bandgap.

$$V_{OC,BC,2} = \frac{nkT}{q} \ln\left(\frac{J_{SC,BC,2}}{J_o}\right) \tag{1.12}$$

Fig. 1.11 below shows the η_{Total} of several combinations of η_{TC} and $\eta_{BC,2}$ considering a series-connected, monolithically-stacked device. While the η_{TC} values are hypothetical, the $\eta_{BC,2}$ values are gathered from real devices[14] and then reduced by a factor of *x*:

$$x = \frac{V_{OC,BC,2} * J_{SC,BC,2}}{V_{OC,BC,1} * J_{SC,BC,1}} * FF_{BC,1} \tag{1.13}$$

where the $V_{OC,BC,1}$, $J_{SC,BC,1}$ and $FF_{BC,1}$ are extracted from real efficiency table, $J_{SC,BC,2}$ is calculated by (1.11), then the $V_{OC,BC,2}$ by (1.12).

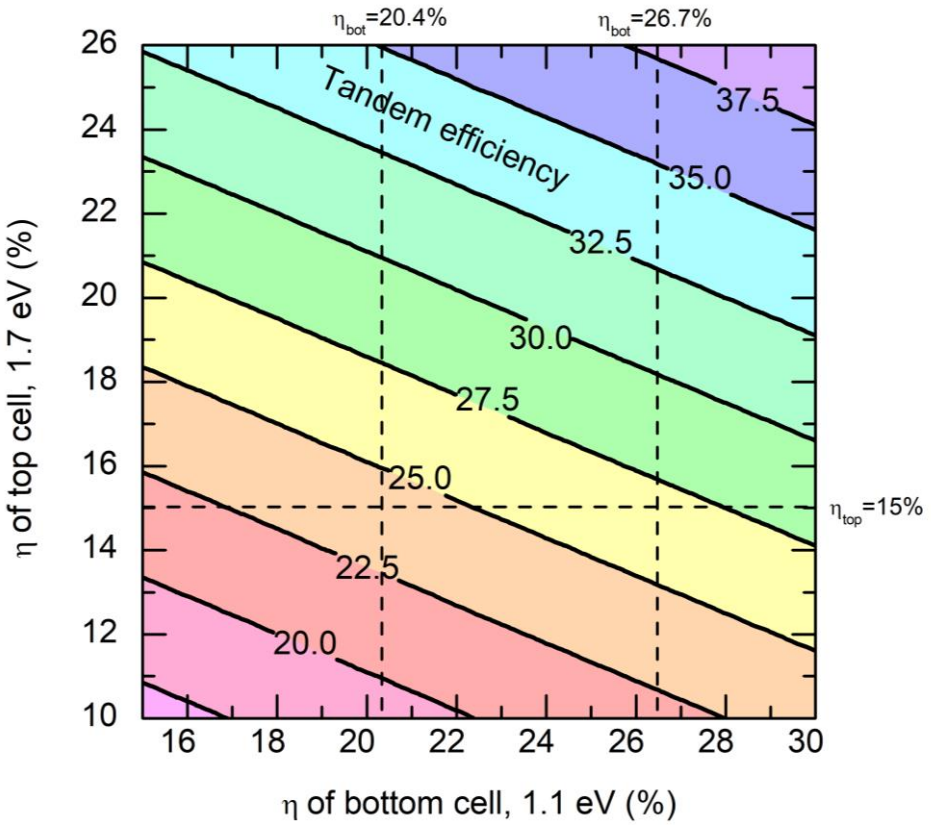

Fig. 1.11 Efficiency of a Tandem Made of a 1.7 eV and a 1.1 eV Top Cell and Bottom Cell. [14], [15]

An η_{TC} of 15% or above is what is needed for a total efficiency gain when a 1.7-eV top cell is matched with a record-efficiency 26.7% Silicon bottom cell. With more practical values for the bottom cell, such as the record Si module cell efficiency of 20.4%, the total efficiency gain for a 1.7-eV/1.1-eV tandem is much higher.

Chapter Summary

This chapter briefly introduces the reader to photovoltaics history and device physics with an emphasis on CdTe and Si solar cell technologies. Notably, CdTe and Si solar cells are low-cost, high efficiency and well-established industries. There is much promise in a II-VI/V 1.7-eV/1.1-eV tandem with $Mg_xCd_{1-x}Te$ acting as the top cell and a Si acting as the bottom cell.

CHAPTER 2 - GROWTH AND CHARACTERIZING OF 1.7 EV $Mg_xCd_{1-x}Te/Mg_yCd_{1-y}Te$ (x<y) DOUBLE HETEROSTRUCTURES

2.1 Introduction

This chapter discusses the growth and characterization of $Mg_xCd_{1-x}Te$ epitaxial films and $Mg_xCd_{1-x}Te/Mg_yCd_{1-y}Te$ (x<y) double heterostructures. This work builds on previous studies from the ASU MBE group which probed the limits of single-crystal CdTe material quality and performance in an optoelectronic and/or photovoltaic device. The first section introduces the molecular beam epitaxy (MBE) growth of CdTe and $Mg_xCd_{1-x}Te$ epitaxial films on lattice-matched InSb(001) substrates. High resolution X-ray diffraction (HR XRD) is utilized to characterize crystal quality and morphology, ellipsometry is utilized to characterize optical properties, and X-ray photoelectron spectroscopy (XPS) is utilized to characterize the characteristics of the CdTe/InSb interface. Each will be discussed in the chapter below.

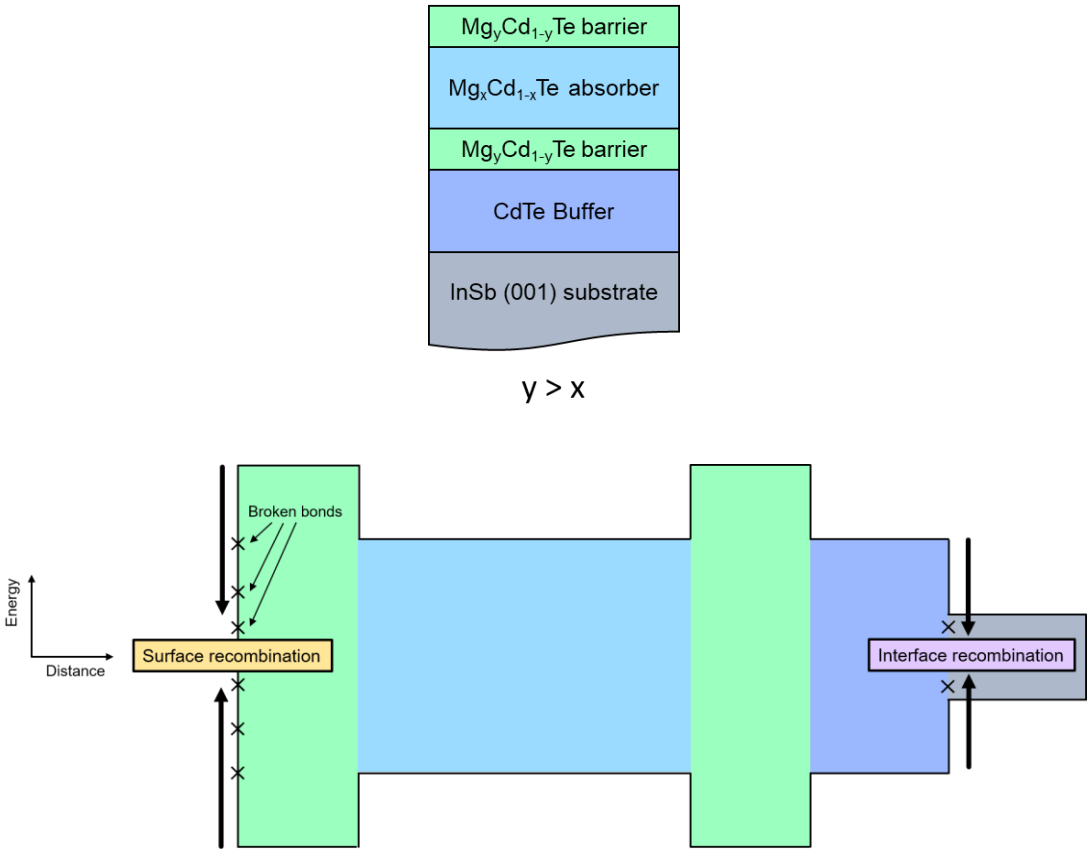

Fig. 2.1 A Basic Double Heterostructure Layer Design and Corresponding Band Diagram.[16]

A rigorously analyzed type of structure used during the past CdTe studies and in this paper's current work is the double heterostructure, an example of which is shown in Fig. 2.1 above. This type of design (coined a Type-II heterostructure) can confine carriers and passivate interfaces. Otherwise, carriers can be trapped and will then recombine nonradiatively, limiting radiative recombination (necessary for an efficient optoelectronic device) and/or carrier collection (necessary for an efficient photovoltaic device). More discussion on recombination and the characterization of optical quality, notably photoluminescence spectroscopy, will be discussed in the following chapter.

2.2 Basics of Molecular Beam Epitaxy

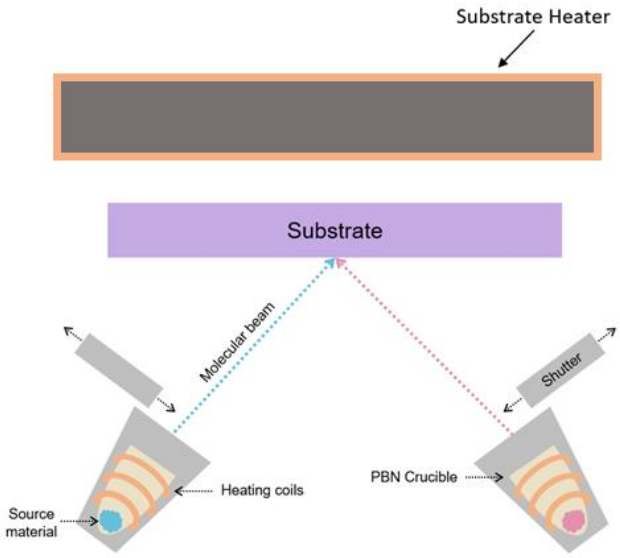

Fig 2.2 Schematic of Molecular Beam Epitaxy Technology. [17]

Molecular beam epitaxy is a deposition technique by which molecular beams (of a single type of atom or molecule) experience an infinite mean free path in ultra-high ($<10^{-10}$ Torr) vacuum. A schematic of MBE basic is shown in Fig 2.2 above. The equation for mean free path of a specific atom is:[17]

$$\lambda = \frac{RT}{\sqrt{2}\pi d^2 N_A P} \tag{2.1}$$

wherein R is the gas constant, T is the temperature, d is the diameter of a specific atom, N_A is Avogadro's number and P is pressure. It is clear that the lower the pressure in a given system, the longer the mean free path of a given molecule. If the pressure is low enough, the mean free path can expand beyond the boundaries of a system (i.e. vacuum chamber walls) becoming virtually infinite.

This infinite mean free path is enabled by ultra-high vacuum within the chamber. In order to ensure minimum impurities and outgassing, ultra-pure (1 ppm or better) source material is used. The beam fluxes are controlled by cell temperatures and/or valves and can be stopped and started abruptly using shutters.

The substrate is heated in order to give the adatoms energy to find the appropriate lattice sites in the crystal surface. As shown by Fig. 2.3, when the molecular beam source is incident on the surface, several mechanisms are possible. With an optimized substrate temperature and flux of source materials, energetically-favorable growth conditions are provided for the adatoms to remain on the sample surface, migrate to a preferred lattice site, and then incorporate into the crystal pattern, slowly building up the epitaxial film.

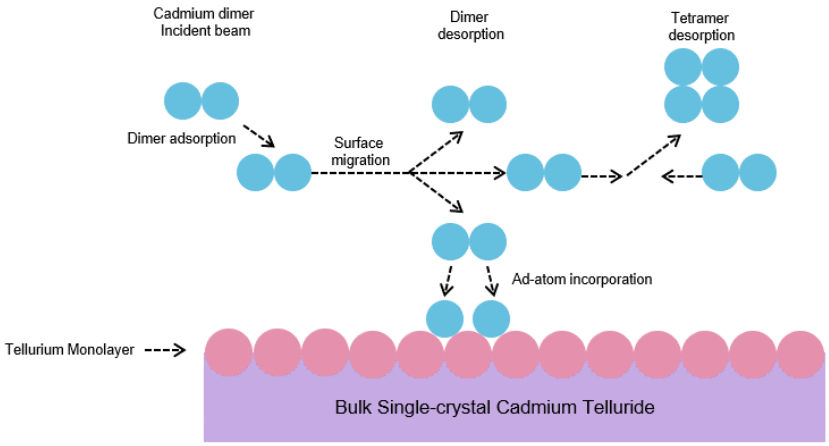

Fig. 2.3 Schematic of The Processes Involved in Molecular-beam-epitaxial Growth. *Adapted from Henini 2012*[17]

The ideal conditions for the growth of CdTe on InSb(001)[16] include a substrate temperature of 280 ℃ and a Cd:Te flux ratio (described in greater detail in Section 2.4 below) of 3:2. While determination of ideal growth conditions is aided by the knowledge of source material vapor pressures, melting points, and other material data, ideal growth

conditions are often optimized empirically, wherein the surface roughness and bulk crystal order of growths are characterized and iterated to maximize film perfection. One important parameter to consider is the critical thickness of an epitaxially-grown materials system.

Critical thickness is determined by the Matthews-Blakeslee equation[18][19]:

$$h_c = \frac{b}{2\pi f}\frac{\left(1 - v\cos^2\alpha\right)}{(1+v)\cos\lambda}\left(\ln\frac{h_c}{b} + 1\right) \quad (2.2)$$

where b is the Burger's vector $\frac{a}{2}\langle 110\rangle$, f is the lattice mismatch, v is the Poisson's ratio and α and λ are angles of the dislocation core, commonly assumed to be 45^0 or 60^0. The lattice mismatch between the growing crystal and the crystal atop which it is growing is:

$$f = \frac{a_s - a_f}{a_f} \quad (2.3)$$

where a_s is the lattice constant of the substrate and a_f is the lattice constant of the epilayer growing atop the substrate. The Burger's vector (b) represents the magnitude and direction of the lattice distortion resulting from a dislocation in a crystal lattice[20] and is determined by the equation:

$$b = \frac{a_f}{2}\sqrt{h^2 + k^2 + l^2} \quad (2.4)$$

where $h, k, and\ l$ are the direction of the Burger's vector. The Poisson's ratio, or the ratio of transverse to axial strain, and can be determined by the equation:

$$v_f = \frac{C_{12}}{C_{12} + C_{11}} \quad (2.5)$$

where C_{12} is the modulus for transverse strain and C_{11} is the modulus for axial strain.

Knowing the estimate for the critical thickness is important. This value can predict the estimated thickness at which strain relief in the growing crystal causes misfit dislocations

which propagate upward as threading dislocations, generating defect sites and increasing nonradiative recombination. A schematic of tensile and compressive misfit is shown in Fig. 2.4 below.

In order to preserve maximum crystalline order in a growing film, it is helpful for said film to be grown on closely lattice-matched substrates. Using parameters from Appendix A, the critical thickness of CdTe on InSb (a lattice mismatch of 0.03%) is ~600 nm. For the materials system of MgTe on CdTe (a lattice mismatch of 1%), the critical thickness is ~10 nm.

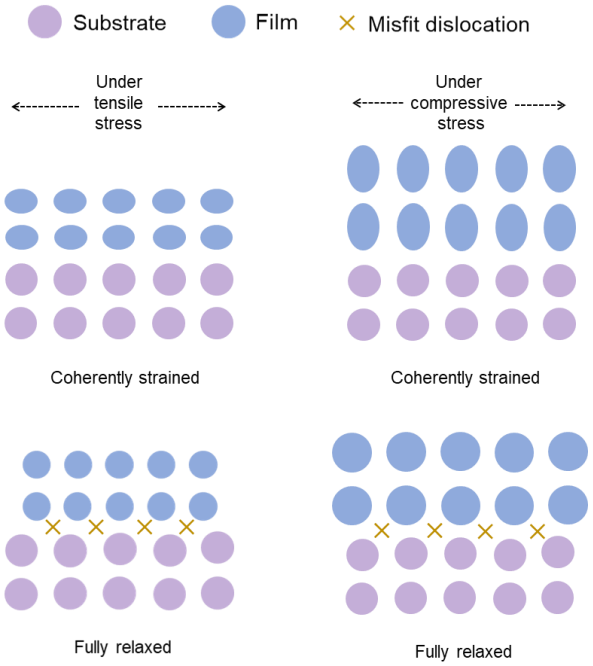

Fig. 2.4 A Schematic of Compressive Versus Tensile Strain, in Both Fully Coherent and Fully Relaxed Conditions.

A look at the band energy and lattice constant of several different semiconductor materials in shown in Fig. 2.5 below. Note that CdTe (6.48 Å), MgTe (6.42 Å) and InSb (6.481 Å) are closely lattice-matched[21].

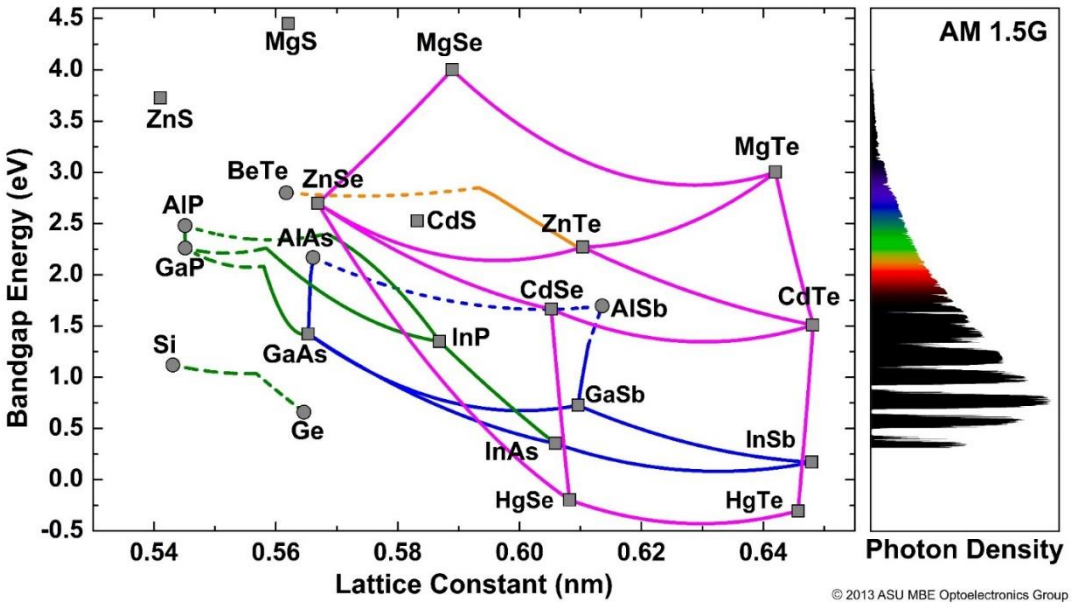

Fig. 2.5 Bandgap Energy Versus Lattice Constant of Various Semiconductors.

2.3 In-Situ Reflection High Energy Electron Diffraction

Reflection High Energy Electron Diffraction (RHEED) is an *in-situ* monitoring tool useful for observing and analyzing an MBE growth process as it is happening. Because it is a diffraction technique, RHEED operates in reciprocal (*k*-space). An electron beam of a specific energy (commonly 15 keV) is incident on the growing surface at a very shallow angle.[22]

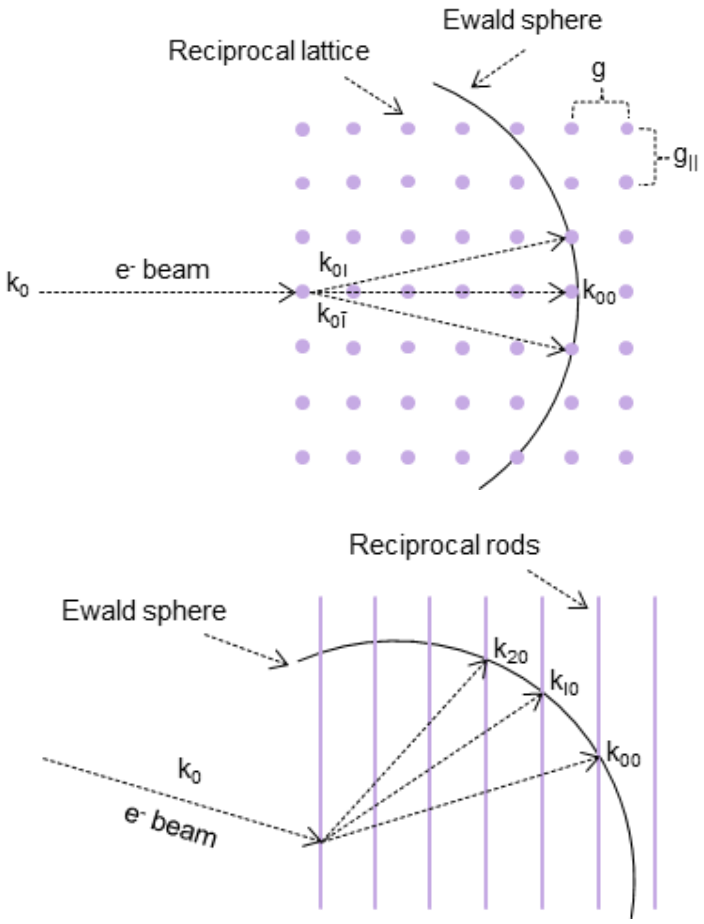

Fig. 2.6 A Schematic of Reciprocal Space Both with X, Y, and Z Constrains (top) and a Degree of Freedom of The Z-direction (bottom).

Whereas the diffraction of a bulk material will show as finite points constrained to the x, y, and z directions (Fig. 2.6 top, described in further detailed in Section 2.5) the growth of MBE is (ideally) so smooth that a degree of freedom reveals itself in the z direction as a rod (Fig. 2.6 bottom). The presence of reciprocal rods in a RHEED images shows that the surface is very smooth.

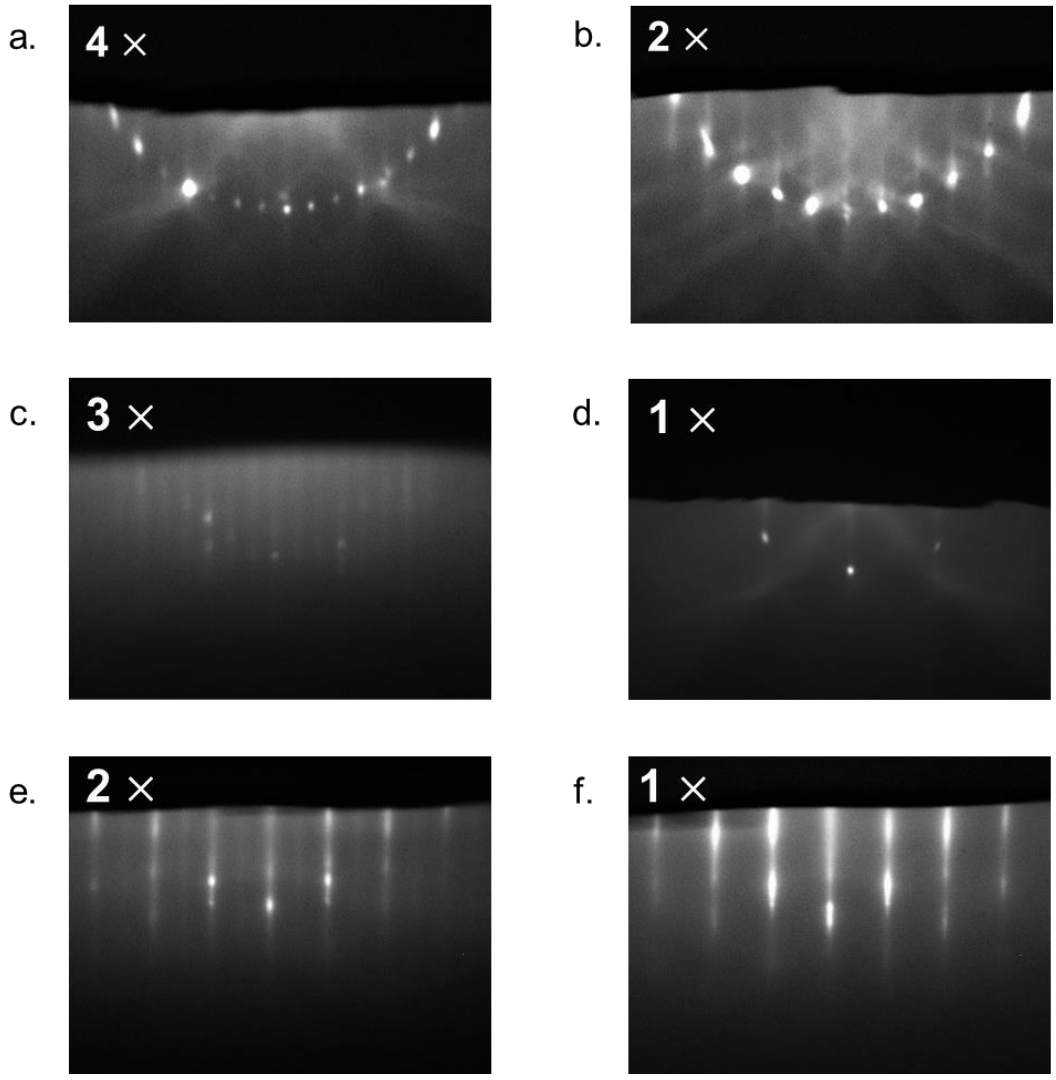

Fig. 2.7 InSb(001) a) 4 × and b) 2 × at 200 ºC, InSb(001) c) 3 × and d) 1 × at 280 ºC, and CdTe e) 2 × and f) 1 × at 280 ºC.

RHEED is an essential tool for MBE growth, as it allows for real-time analysis of the MBE process, saving precious time and material which could be wasted by relying on *ex-situ* analysis techniques. Each material surface has a distinct RHEED pattern at different azimuths. In addition, temperature, as it affects the behavior of a bulk material, also affects RHEED patterns. The top pair of Fig. 2.7 (a and b) depict RHEED images of

InSb(001) at 200℃. The middle pair (c and d) depict the RHEED images of InSb(001) at 280℃. The bottom pair depict RHEED images of CdTe at 280℃.

In addition to real-time analysis of the species and quality of a growth surface, RHEED can also provide other essential information, including the determination of the growth rate of a growing film.

2.4 Growth Rate and Flux Ratio Calibration

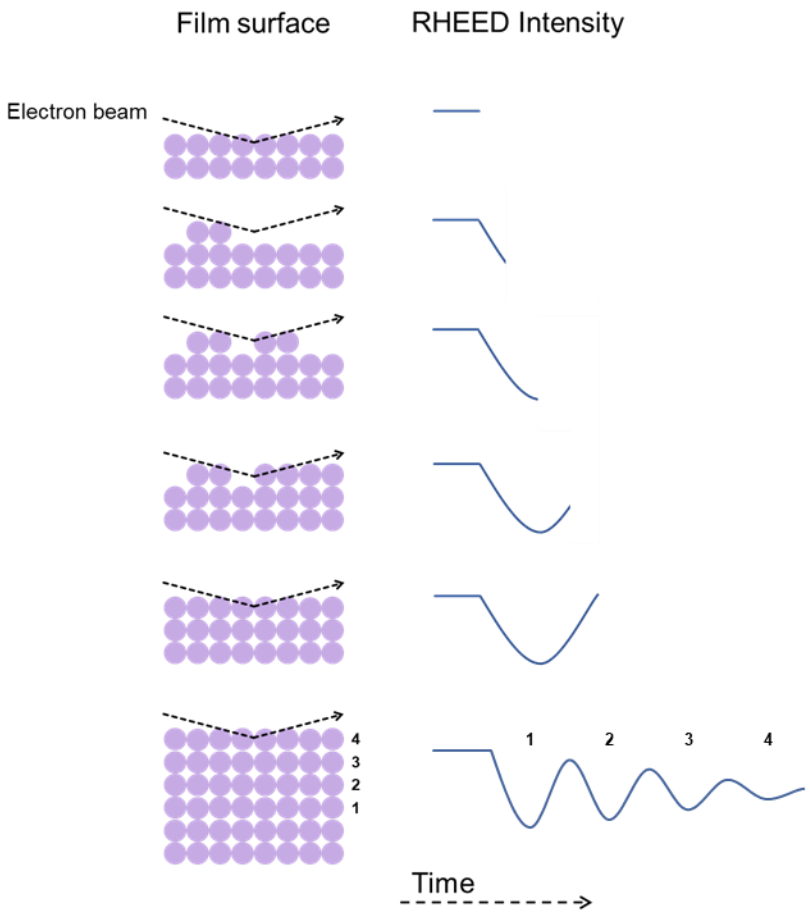

Fig. 2.8 Fitting The Dampening of RHEED Intensity Oscillations Provides a Growth Rate.[17],[23]

The growth rate of a film can be determined *in-situ* by fitting RHEED intensity oscillations (Fig. 2.8).[17],[23] Each period correlates to a monolayer of film being grown. The intensity is at its highest when there is a completely smooth surface (directly before or after a monolayer of growth) and at its lowest, the middle of the growth of a layer. The period of the sinusoidal curve corresponds to an estimated growth rate for a given monolayer thickness.

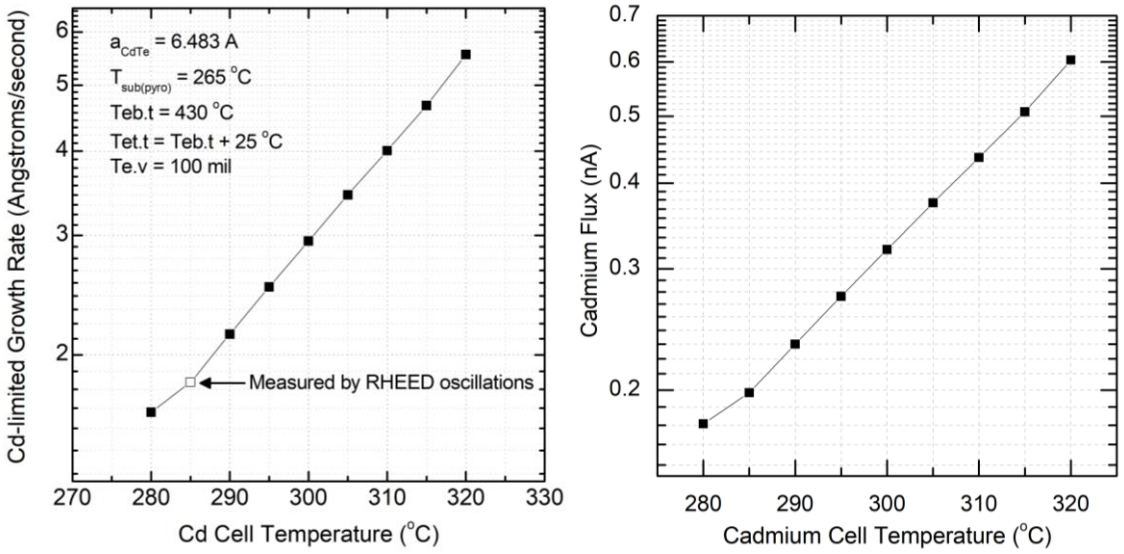

Fig. 2.9 The Cadmium Limited Growth Rate Measured by RHEED Oscillations and Cadmium Flux Versus Cadmium Cell Temperature.

When the growth rate is limited by one of the species, for example a Cd-limited growth in CdTe, a change in limiting species flux changes the periodicity of the sinusoidal curve while the increase of the rich species does not affect the periodicity. The growth rate of CdTe during Cd-limited conditions is directly proportional to the flux of Cd. Thus, the Cd-limited growth rate of CdTe can be calibrated by keeping the shape of the curve constant while calibrating the Cd-limited growth rate at one repeated Cd cell temperature.

An example of the results of growth rate calibrations are shown in Fig. 2.9. In this way, growth rates can be calculated with a minimal amount of time and precious material used.

When considering the growth of a ternary alloy, calibration becomes more complex. The behavior of each individual species is a factor in how quickly and smoothly a film grows. For example, consider the case of magnesium cadmium telluride ($Mg_xCd_{1-x}Te$). The customary procedure for growing $Mg_xCd_{1-x}Te$ is to keep the CdTe conditions the same (growth rate and flux ratio) and then add a Mg flux over the existing CdTe conditions. This slightly affects the growth rate of CdTe, but not enough that drastic changes to the procedure need to be considered. The composition of the $Mg_xCd_{1-x}Te$ needed to be determined by an empirical study of $Mg_xCd_{1-x}Te$ composition for various Mg fluxes. The bandgap versus Mg composition of $Mg_xCd_{1-x}Te$ is given by:[24]

$$E_G = 1.5 + 1.7x + 0.3x^2 \qquad (2.6)$$

where E_G is the bandgap of the $Mg_xCd_{1-x}Te$ and x is the composition of Mg in $Mg_xCd_{1-x}Te$. This results in the relation shown below in Fig. 2.10. The effects of barrier geometry and dopability are discussed in the sections below.

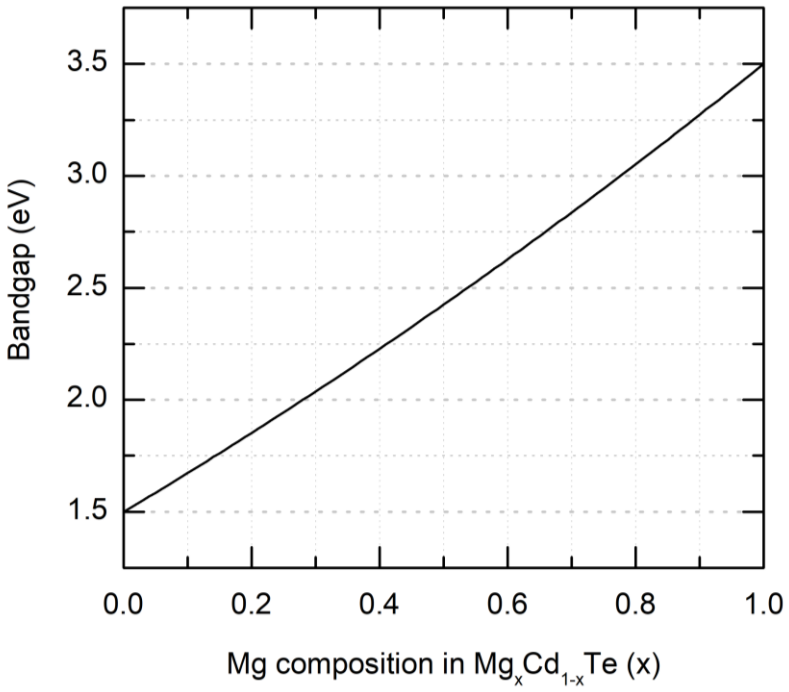

Fig. 2.10 The Relationship of Bandgap Versus Mg Composition in $Mg_xCd_{1-x}Te$.[24]

2.5 High Resolution X-ray Diffraction

In a single-crystal X-ray diffraction measurement (shown by Fig. 2.11), a sample is mounted on a goniometer, a device which allows the mounted sample to be moved to a precise angle corresponding to specific crystallographic directions. The mounted sample is hit with monochromatic X-ray beams, before it is scattered by interactions within the lattice before passing into a detector.

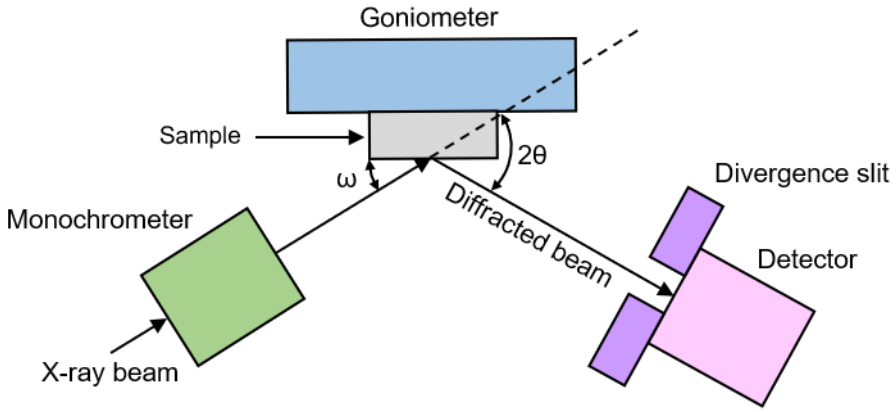

Fig. 2.11 Schematic of High-Resolution X-ray Diffraction Equipment Featuring a Triple-axis Rocking Curve Setup.

This beam can either scatter coherently or incoherently, and diffracts in a way which corresponds to Bragg's Law[25]:

$$n\lambda = 2d \cdot sin\theta \tag{2.7}$$

where n is a positive integer, λ is the wavelength of the incident X-ray, and d is the lattice spacing:

$$d = \frac{a}{\sqrt{h^2 + k^2 + l^2}} \tag{2.8}$$

where a is the lattice constant of a cubic crystal, and h, k, and l correspond to the direction of a Bragg plane. Each Bragg plane (*hkl*) corresponds to an omega (ω – the angle between the incident beam and sample) and the 2Theta (2θ - the Bragg angle, theoretically double the value of ω). A depiction of Bragg's Law at work is shown in Fig. 2.12 below.

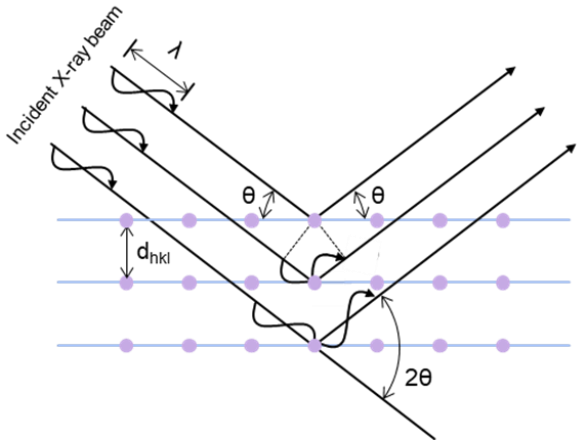

Fig. 2.12 A Schematic of Bragg's Law in a Single Crystal Bulk Film.[25]

For bulk $Mg_xCd_{1-x}Te$ and $Mg_xCd_{1-x}Te/Mg_yCd_{1-y}Te$ (x<y) double heterostructures, high-resolution XRD a powerful tool for characterizing the degree of crystallinity and order in the epitaxially-grown layers. A high-resolution triple-axis rocking curve set-up is used. In this type of set-up, the ω is varied (rocked) while the 2θ is narrowed by a divergence slit and fixed. As the substrate and grown films are zinc blende structures aligned to (001) in the z-direction, an Omega 2θ scan around the (004) peak reveals a great deal about the structure.

A high-resolution XRD scan along the (004) peak of a $Mg_xCd_{1-x}Te/Mg_yCd_{1-y}Te$ double heterostructure on InSb(001) is depicted in Fig. 2.13 below. Note that CdTe and InSb peaks (with a lattice mismatch of only 0.3%) are two distinct peaks, showing the high sensitivity of this high-resolution measurement.

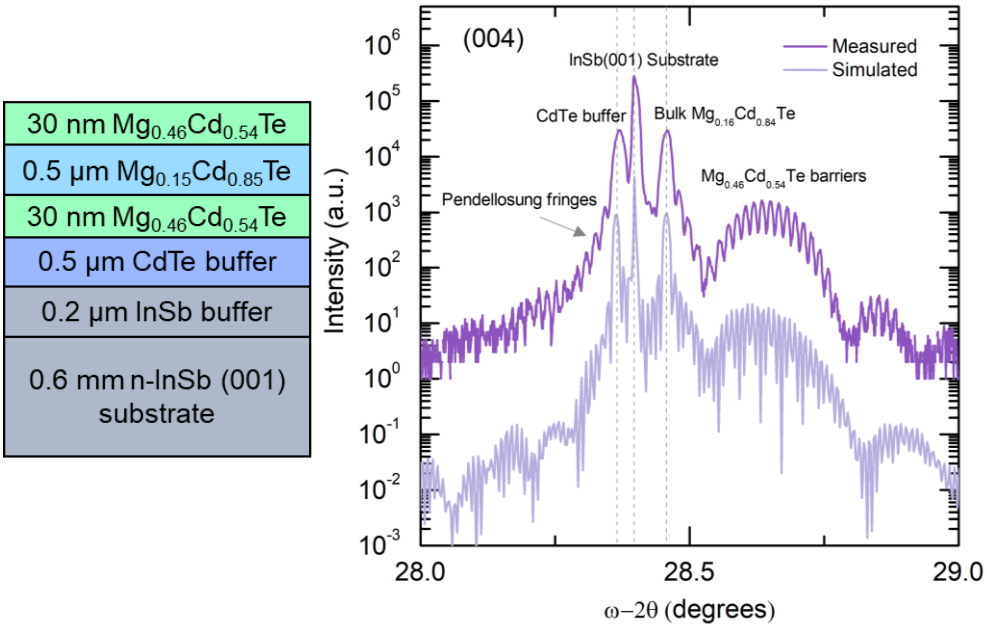

Fig. 2.13 High-resolution X-ray Diffraction Scan Around The (004) Peak of 1.7 eV $Mg_xCd_{1-x}Te$ Double Heterostructure on InSb(001) Featuring Abrupt Mg Composition Interfaces.

The CdTe, InSb and bulk $Mg_{0.16}Cd_{0.86}Te$ layers are thick enough (from 500 nm to several hundred microns) that they reveal themselves as distinct, sharp peaks in the scan. The full width at half max (FWHM) of each of these peaks is on the order of 2 orders of magnitude. The $Mg_{0.16}Cd_{0.86}Te$ film has a FWHM on the order of a CdTe film with similar thickness. This suggests that the crystallinity of the $Mg_{0.16}Cd_{0.86}Te$ is comparable to a highly-ordered CdTe film, revealing the quality of this ternary alloy.

The two 30 nm $Mg_{0.46}Cd_{0.54}Te$ layers reveal themselves to be one much broader peak. Pendellosung fringes, indicated in Fig. 2.13, are present when diffracted beams interfere at the mirror-like interfaces of coherently-strained films.[26]

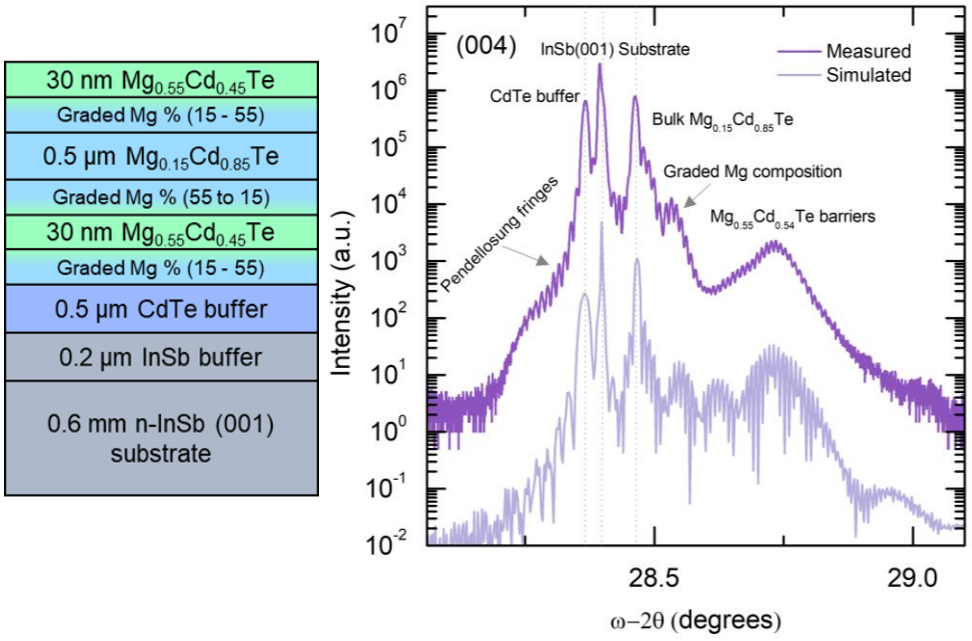

Fig. 2.14 High-resolution X-ray Diffraction Scan Around The (004) Peak of 1.7 eV $Mg_xCd_{1-x}Te$ Double Heterostructure on InSb (001) Featuring Graded Mg Composition Interfaces.

The Pendellosung fringes are also present in sample with graded layers, however they are dampened in amplitude. As shown in Fig. 2.14, between the $Mg_{0.15}Cd_{0.85}Te$ and $Mg_{0.55}Cd_{0.45}Te$, there are features which correspond to a grading in lattice constant, confirmed by curve fitting of simulations in X'Pert Epitaxy.

2.6 Characterization of the CdTe/InSb(001) Interface

2.6.1 Introduction to MBE-grown Interfaces[17]

A heterovalent interface is one which exists at the junction of two materials, each made up of one or more different elemental groups. Depicted by the left image of Fig. 2.15, the

growth of a thin film on a like substrate (homoepitaxy) is relatively simple, as there are no differences in lattice constant and/or bonding behavior between, for example, a GaAs film and a GaAs substrate. Added complexity is introduced in the form of an isovalent heteroepitaxial structure, wherein the valency of the grown film and substrate are the same however the lattice constant of each is different (Fig. 2.15 middle). As described in the sections above, if the lattice constants are different enough then misfit dislocations will accumulate beyond what may be considered practical and usable. Techniques such as grading the material from one to another or threading dislocation annihilation may help increase material quality of the epi-grown film but may be insufficient and/or impractical to the desired structure design and application. Additionally, differences in thermal expansion coefficients need to be considered as they may lead to dislocation formation as well.

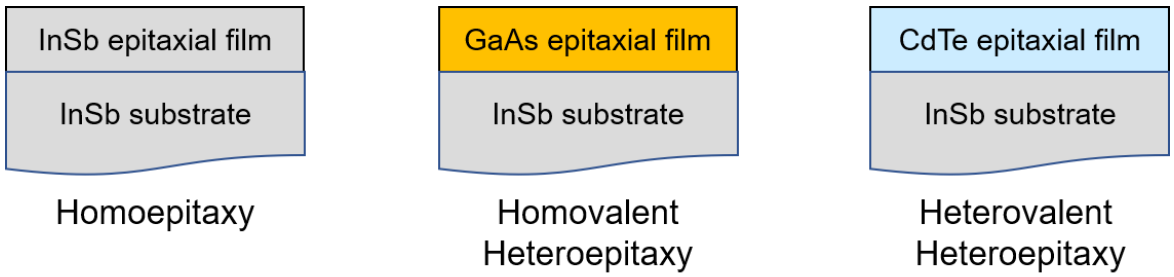

Fig. 2.15 A Schematic of Three Different Types of Epitaxial Interfaces (left) Homoepitaxy (center) Isovalent Heteroepitaxy (right) Heterovalent Heteroepitaxy.

Heterovalent heterostructures (Fig. 2.15 right) add another layer of complexity, as there is a chemical imbalance present at the interface between materials consisting of different elemental groups. A zincblende cubic compound semiconductor consists of atoms

bonded together to satisfying 8 electrons in their outermost orbital. A III-V material (i.e. InSb) consists of Group III (i.e. Ga, In, Al) and Group V (i.e. As, Sb, P) elements, which through covalent bonding contribute three and five electrons, respectively. The same is true for II-VI materials, such as CdTe, which consist of Group II (i.e. Cd, Mg, Zn) and Group VI (i.e. Te, Se, O) elements.

For bonds at the interface of a II-VI and a III-V material, it is not possible to achieve charge neutrality with a II-III, V-VI, II-V or III-VI covalent bond alone. The bonding of each binary will introduce a deficit of ¾ electrons, a surplus of ¾ electrons, a deficit of ¼ electrons or a surplus of ¼ electrons per bond respectively.

A II-V (Cd-Sb) or III-VI (In-Te) bond is closer to charge neutrality than that of the other two bond types, however more questions need to be asked about the bonding behavior of the resulting binary alloys. Consider the heat of formation of various compounds in a reaction:

$$H = H_p - H_r \tag{2.9}$$

where H_p and H_r are the added-up heat of formations of products and reactants, respectively. Table 2.1 below shows the heat of formation of various compounds. The more negative the H, the more energetically favorable the resulting compound.

Table 2.1 The Heat of Formations of Several Cd, In, Te, and Sb Containing Compounds.[24]

Compound	*H* (kcal/mol)
CdTe	-24.3
In_2Te	-19.0
InTe	-17.2
In_2Te_3	-45.8
In_2Te_5	-45.8
InSb	-7.5
Sb_2Te_3	-13.5
CdSb	-3.2
Cd_3Sb_2	-8.0

When indium and telluride bond, they can have a tendency to form In_2Te_3 compound, a material which has been shown to consist of many vacancies.[27] In a closed system (no species can escape) the formula for In_2Te_3 formation is:

$$2InSb(s) + 3CdTe(s) \rightarrow In_2Te_3(s) + Cd_3Sb_2(s) \quad (2.10)$$

for which $H = +34.1\ kcal$.

When considering a closed system, where volatile species can escape, the equation becomes:

$$2InSb(s) + 3CdTe(s) \rightarrow In_2Te_3(s) + 2Sb(s) + 3Cd(g) \quad (2.11)$$

for which $H = +61.6\ kcal$. At warmer growth temperatures above 200 ℃, the reaction becomes more negative. Additionally, it should be considered that Cd has a much higher vapor pressure and volatility of the other three species[28]. With that consideration, the equation becomes:

$$2InSb(s) + 3Te(s) \rightarrow In_2Te_3(s) + 2Sb(s) \quad (2.12)$$

for which $H = -30.8\ kcal$.

Therefore, under real-life MBE conditions, a defect-rich In_2Te_3 compound is probable at the interface of CdTe and InSb. However, since MBE does not require equilibrium conditions, the formation of CdTe and the suppression of In_2Te_3 can be driven by a large Cd overpressure during growth.[29] Thus, shown by Fig. 2.16, previous studies[30] empirically investigating the dependence of Cd overpressure on crystal quality have shown that a moderate Cd overpressure improves the smoothness of the growing layers at the CdTe/InSb interface and the crystal quality of the grown bulk material. The abruptness of the film was further confirmed using Transmission Electron Microscopy.

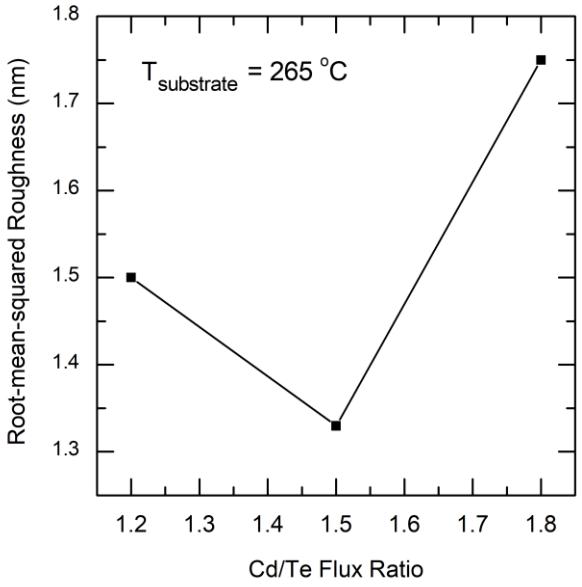

Fig. 2.16 The Root-mean-squared Roughness Versus Cd/Te Flux Ratio for a Substrate Temperature of 265 ^{o}C.[30]

2.6.2 X-ray Photoelectron Spectroscopy of CdTe/InSb(001)

The CdTe/InSb heterojunction has attracted considerable attention due to its almost perfect lattice match, making this a model system with which to analyze the heterovalent interface, including non-octal interface bonding, heterovalent band offsets, and electrical

field-induced interfacial topological insulators. In this study, MBE was used to grow several samples of CdTe on InSb(001) to study the growth, and determination of the band offset between these two materials was determined by X-ray Photoelectron Spectroscopy (XPS).[31]

XPS is a UHV, surface sensitive technique which measures the kinetic energy and number of electrons which escape the top 0-10 nm of a sample surface irradiated with X-rays. A schematic of this technique is presented in Fig. 2.17. Due to conservation of energy depicted below:

$$hv = E_{kinetic} + E_{binding} \tag{2.13}$$

wherein hv is the energy of the incident X-ray beam, $E_{kinetic}$ is the kinetic energy of the electron as measured by the analyzer and $E_{binding}$ is the binding energy of the electron, the binding energy can easily be calculated.

This measurement technique can be used to determine elemental composition, as well as the electronic and chemical states necessary to determine the configuration of energy bands at the interface of two materials.[32]

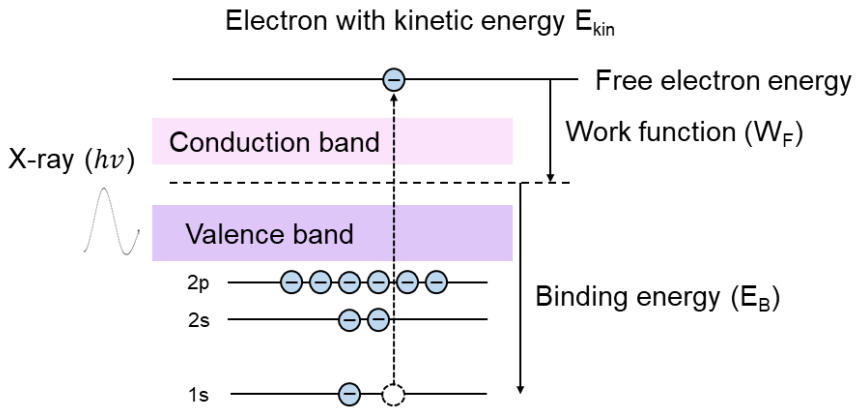

Fig. 2.17 The Features of Energy Levels in a Material Which Affect The Resulting Spectra of an XPS Measurement.

Two samples were used for this study, bare InSb and 5 nm CdTe on InSb(001). For the latter, a Cd flux is introduced to the InSb(001) surface 10 minutes prior to CdTe growth, which proceeded under Cd-rich (Cd:Te = 3:1) conditions and a substrate temperature of 280 ºC (measured by a pyrometer). This procedure is the exact same as growing larger thicknesses of CdTe on InSb(001).

The samples are transferred in atmosphere and characterized in a UHV surface analysis system which includes XPS with a high intensity monochromatized Al Kα X-ray source (1486.7 eV), and UPS optimized for He I radiation at 21.2 eV.

Prior to analysis, the samples are cleaned by a remote hydrogen plasma system, from which XPS scans clearly show in Fig. 2.18 the removal of the surface oxides and contaminants including carbon and oxides Fig. 2.18 (right) shows just how important this process is, as the Sb 3d peak cannot be resolved without the removal of the O 1s peak.

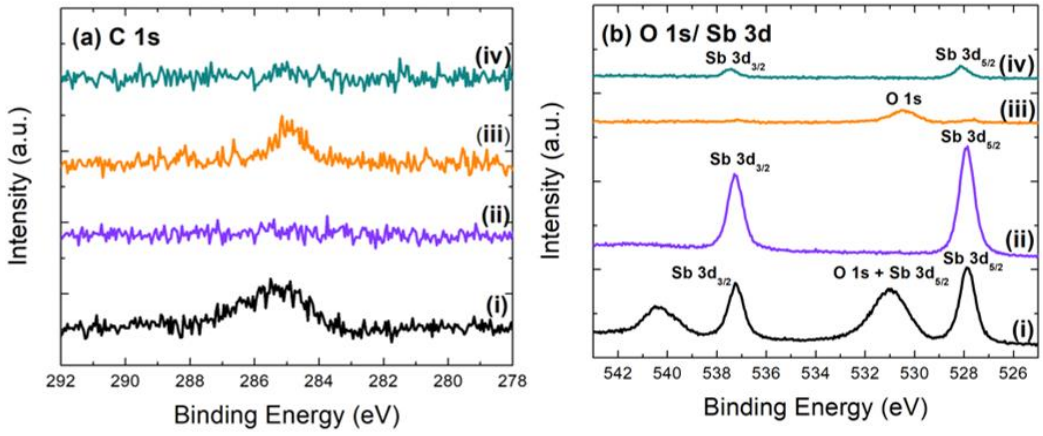

Fig. 2.18 X-ray Photoemission Spectroscopy Scans of a) The C 1s Peak and b) The O 1s and Sb 3d Peak of i) InSb Before The H-plasma Clean, ii) InSb After 5 Min., and b) CdTe/InSb i) Before and ii) After H-plasma Clean.[31]

The low binding energy regime is investigated using both ultraviolet photoemission spectroscopy (UPS) and XPS. The lower energy of the UPS source (21.2 eV) is able to probe close to the VBM in order to accurately determine its value in both samples, seen in Fig. 2.19 right. Using XPS, as shown in Fig. 2.19 left, the Sb 4d peaks from are lined up to accurately compare the spectra between both samples. The difference between the Sb 4d to valence band maximum of the two scans is 0.9 eV. XPS results (Fig. 2.19 left) reveal the VBM is at 0.11 eV below the Fermi level for the InSb surface and is located 1.2 eV below the Fermi level for the CdTe surface. Overall, a type-I alignment for the CdTe/InSb (001) interface is determined. These values are used to determine the valence band offset from the equation below:

$$VBO = (E_{CL}^{InSb} - E_{VBM}^{InSb}) - (E_{CL}^{CdTe} - E_{VBM}^{CdTe}) - \Delta E_{CL} \qquad (2.14)$$

where E_{CL}^{InSb} and E_{CL}^{CdTe} are the respective binding energies of the Sb and Cd 3d core levels, E_{VBM}^{InSb} and E_{VBM}^{CdTe} are the InSb and CdTe valence band maximums measured by UPS, and ΔE_{CL} is the Sb and Cd 3d core level difference at the interface. Plugging these values into the equation above, the *VBO* is calculated to be 0.89 eV.

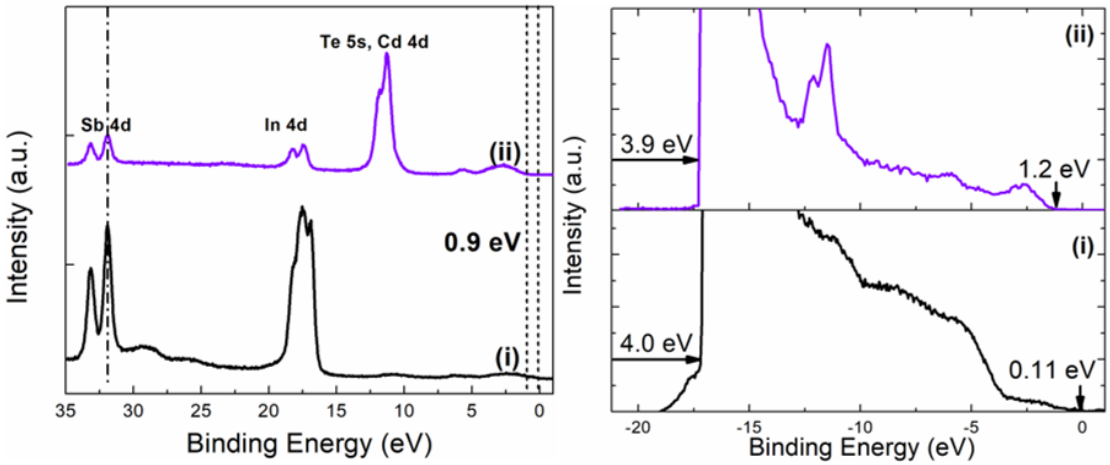

Fig. 2.19 (left) Ultra-violet Photoemission Spectra of i) InSb Surface and ii) CdTe on InSb (right) XPS Scans for Close to VBM Regime i) InSb Substrate ii) After CdTe Deposition.[31]

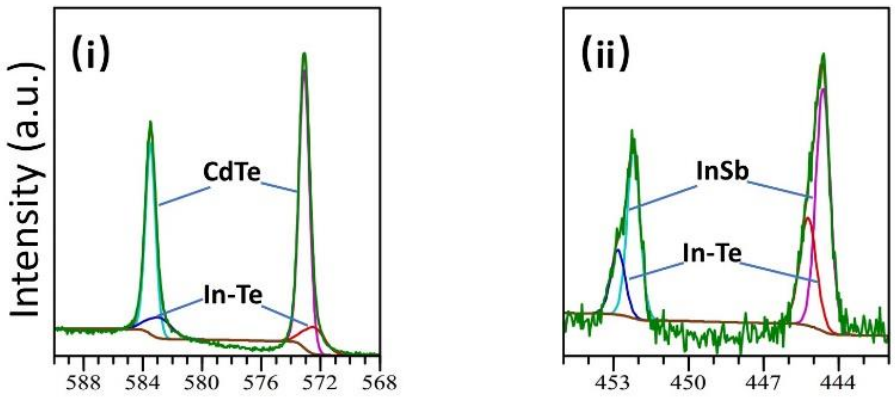

Fig. 2.20 Peak-fitting Analysis for XPS Spectra of Hydrogen-plasma Cleaned CdTe on InSb i) Te 3d and ii) In 3d Peaks.[31]

Fig. 2.20 depicts peak fitting analysis which shows Te 3d and In 3d shoulders indicative of an In_xTe_y interfacial layer. From the literature, it is highly likely that the species at the interface is a stoichiometric InTe compound. Meanwhile, an absence of shoulder peak is observed in the Cd 3d and Sb 3d spectra, which indicates the absence of Cd-Sb bonding. It is believed that the In-Te bonding of this layer contributes to downward band bending of the InSb side. This is likely due to excess electrons which are free to accumulate at the InSb side of the heterointerface, since the conduction band minimum (CBM) of InSb is lower than that of CdTe. This culminates in a band alignment as depicted in Fig. 2.21 below.

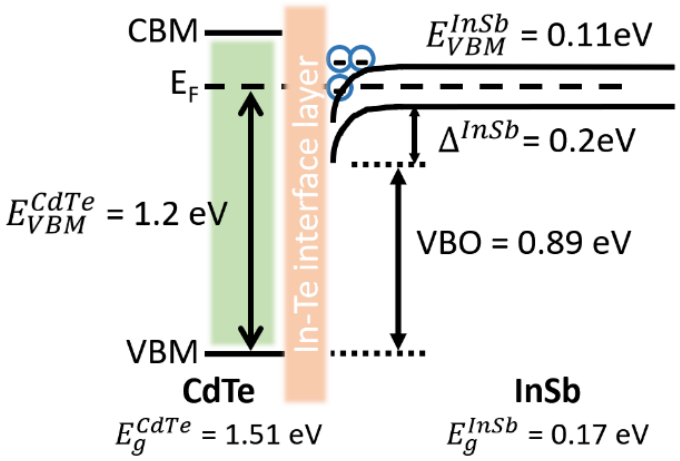

Fig. 2.21 Schematic Depicting The Band Alignment of The CdTe/InSb(001) Heterojunction.[31]

2.7 Ellipsometry of Bulk $Mg_xCd_{1-x}Te$ on InSb(001)

Ellipsometry is an optical measurement technique which measures the change of polarization in a sample upon reflection or transmission and compares it to a model (Fig. 2.22). This makes it useful for investigating the refractive properties of thin films. [33]

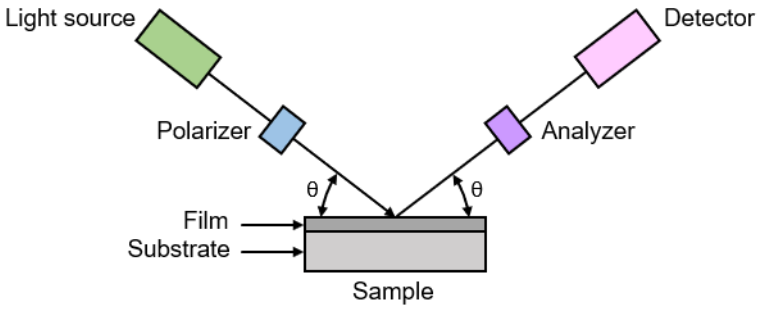

Fig. 2.22 Schematic of an Ellipsometry Measurement System.

Ellipsometry was carried out on a 500 nm MBE-grown bulk $Mg_xCd_{1-x}Te$ sample. As shown by Fig. 2.23, a very high absorption coefficient of 2.5×10^4 cm^{-1} is identified for

the $Mg_xCd_{1-x}Te$ alloy, suggesting this alloy can be an excellent material for use as a top cell absorber layer. The bandgap determined by ellipsometry was identified as 1.81 eV, slightly higher than the bandgap, indicated by PL and discussed in the following section.

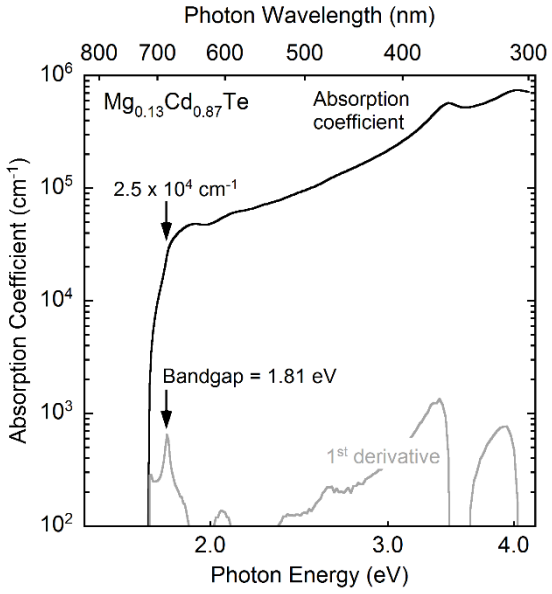

Fig. 2.23 Ellipsometry Spectrum of 500 nm Bulk $Mg_xCd_{1-x}Te$ Calibration Sample.

Additionally, ellipsometry of a bulk 500 nm $Mg_xCd_{1-x}Te$ sample revealed a high absorption coefficient of $\alpha = 2.5\times10^4\ cm^{-1}$ at the band edge. This corresponds to an estimated absorption depth ($1/\alpha$) of 400 nm.

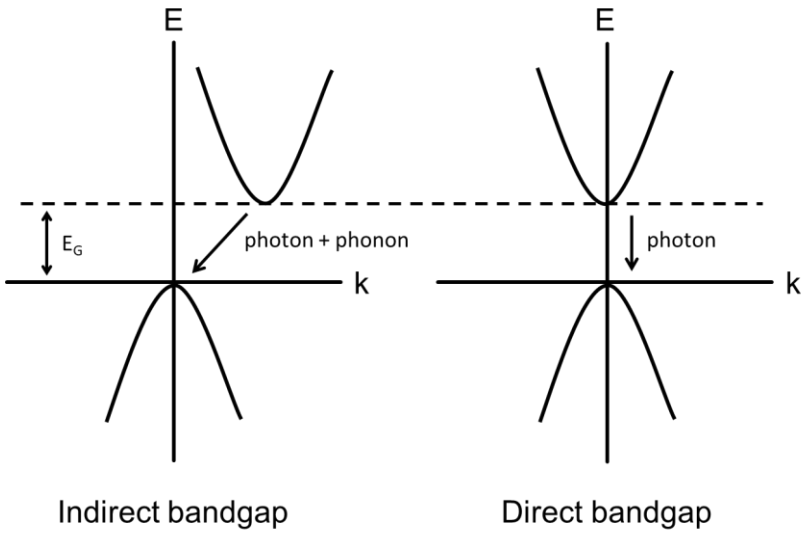

Fig. 2.24 A Comparison of The Feature of Indirect Bandgap (like Si) and a Direct Bandgap (like CdTe).

This is a similar value to that of binary CdTe, and illuminates the benefits of using a direct bandgap semiconductor (the difference is shown in Fig. 2.24)[11] for photovoltaic applications. In contrast, the absorption depth of indirect bandgap Si is several microns.

2.8 Optical Characterization

2.8.1 Steady-state Photoluminescence Spectroscopy

In order to probe the bulk material quality of $Mg_xCd_{1-x}Te/Mg_yCd_{1-y}Te$ double heterostructures, a photoluminescence (PL) spectroscopy collection system can be utilized to compare the optical quality of different sample structures. Photoluminescence is the process by which a material experiences excitation of its electrons by photons in laser light of a specific wavelength. As shown by Fig. 2.25, when excited electrons relax and recombine, they can do so either radiatively through spontaneous emission (produces

a photon) or non-radiatively through either defect-assisted (Shockley Read Hall) recombination and/or Auger recombination. SRH recombination is assisted by defects within the band gap, either donor-like (E_D), accepter-like (E_A) or a trap closer to the middle of the band (intrinsic) (E_i). Due to the intensity of incident light, Auger recombination is not considered during analysis.

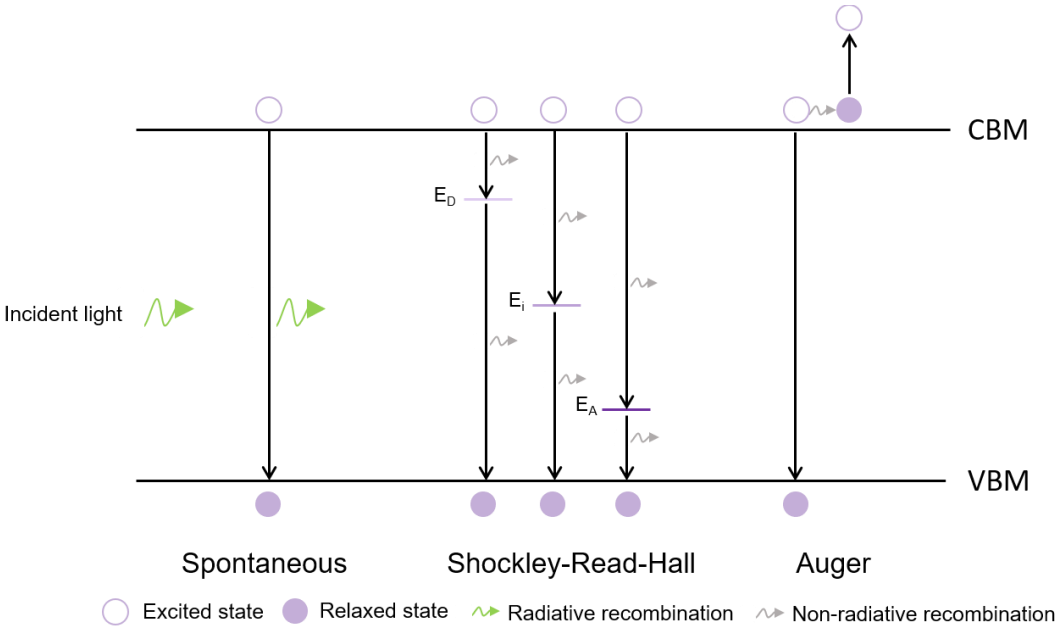

Fig. 2.25 Different Types of Recombination in a Semiconductor.

The steady-state PL system at Arizona State University consists of a spectrometer with a 0.85 m focal length, a photomultiplier tube (PMT), and a germanium detector. A 532 nm diode-pumped solid state (DPSS) 40 mW laser is used as the excitation source and the incident power is adjusted to 0.92 mW using a neutral density filter; the beam radius on the sample is measured to be 0.54 mm. This beam radius corresponds to a power density of 100 $mWcm^{-2}$, similar to one sun. A chopper is used to modulate the laser beam

and to send a reference signal to a lock-in amplifier, which in turn improves the signal-to-noise ratio.

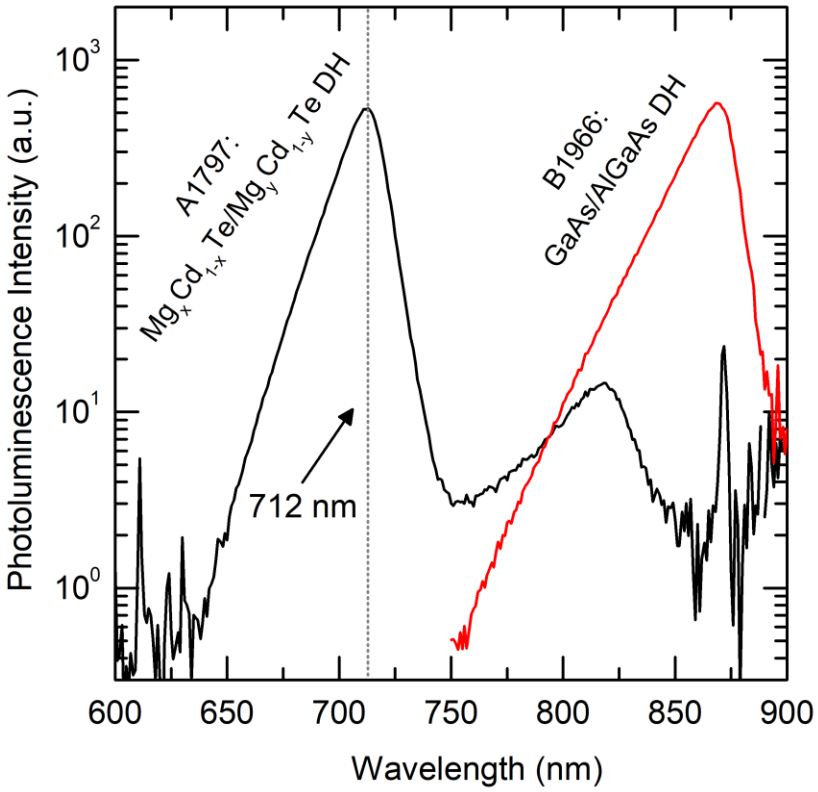

Fig. 2.26 Steady-state Photoluminescence Spectroscopy of 1.7 eV $Mg_xCd_{1-x}Te$.

In order to gauge the optical quality of a $Mg_xCd_{1-x}Te$ double heterostructure (DH) sample against DHs of both $CdTe/Mg_xCd_{1-x}Te$ DH and GaAs/AlGaAs, two samples are measured together under the same conditions, room temperature and with a laser wavelength of 532 nm as seen in Fig. 2.26. The use of reference samples is very important, because it is the best way to develop a standard by which samples can be compared even under slight variations in measurement conditions from scan to scan.

The peak intensity of the $Mg_xCd_{1-x}Te$ DH sample is ~712 nm, which corresponds to a bandgap of ~1.7 eV. There is a second peak around 820 nm which corresponds to the CdTe bandgap (1.5 eV). The peak intensity of the $Mg_xCd_{1-x}Te$ DH sample is comparable to that of a GaAs/AlGaAs reference sample, indicating a high degree of optical quality. This is an important metric to reach, because the presence of excellent optical quality, as describe in the introduction above, indicates minimal defects and non-radiative recombination in this random ternary alloy. It should be noted that there is a small amount of variability in the results due to the difference in refractive index of the compared materials, however not to a high enough degree to significantly affect the resulting scan data.

There is a difference in the bandgap determined by ellipsometry (1.8 eV) vs SSPL (1.72 eV). Though the growth conditions for both the bulk and DH samples were virtually identical. This difference is likely due to the detection by ellipsometry of both unoccupied and occupied states, whereas PL detects only occupied states as it is sensitive to the characteristic tail of the absorption spectrum. In order to probe a deeper understanding of into the optical properties of this $Mg_xCd_{1-x}Te$ material, time-resolved PL and photoluminescence efficiency are measured, as discussed below.

2.8.2 Time-resolved Photoluminescence Spectroscopy

Considerable work has been performed to optimize the carrier lifetime of $CdTe/Mg_xCd_{1-x}Te$ double heterostructures.[34][35][36][37] The carrier life time of carrier in semiconductors, introduced briefly in 2.8.1, can be described in more detail by the equation below:

$$\frac{1}{\tau_{eff}} = \frac{1}{\tau_{rad}} + \frac{1}{\tau_{nr}} = \frac{1}{\tau_{rad}} + \frac{1}{\tau_{SRH}} + \frac{1}{\tau_{Auger}} + \frac{2S_{int}}{d} + \frac{2S_{th}}{d} \quad (2.15)$$

where τ_{rad} is the radiative recombination, τ_{SRH} is defect-assisted Shockley-Read-Hall (SRH) recombination, and τ_{Auger} is high-injection assisted Auger recombination. Auger recombination is not considered during lifetime measurements of $CdTe/Mg_xCd_{1-x}Te$ DHs, as the measurement is taken in the low injection regime. In addition, there is an assumption that carriers are distributed evenly throughout the absorber. As such, the equation changes to accommodate only radiative and SRH recombination. Fleshed out, the equation is:

$$\frac{1}{\tau_{eff}} = \frac{1}{\tau_{rad}} + \frac{1}{\tau_{nr}} = \frac{1}{\tau_{rad}} + \frac{1}{\tau_{SRH}} + \frac{2S_{int}}{d} + \frac{2S_{th}}{d} \quad (2.16)$$

where τ_{SRH} is the defect-assisted SRH recombination, S_{int} is the recombination at the interface, S_{th} is the thermionic emission recombination resulting from carriers jumping over the barriers and recombining at either the surface or the CdTe/InSb interface and d is the thickness of the absorber.

The radiative recombination lifetime τ_{rad} can be calculated as:

$$\tau_{rad} = \frac{1}{(1-\gamma)Bn} \quad (2.17)$$

where B is the radiative recombination coefficient, n is the carrier concentration (both background doping concentration N_{doping} and excess carrier concentration δn) and γ is the photon recycling factor, a value which depends on thickness and the absorption coefficient of the absorber. From C-V measurements the background doping was determined to be an estimated ~5×10^{14} cm^{-3}.

$$\frac{1}{\tau_{nr}} = \frac{1}{\tau_{eff}} - \frac{1}{\tau_{rad}} = \frac{1}{\tau_{SRH}} + \frac{2S_{int}}{d} + \frac{2S_{th}}{d} \quad (2.18)$$

$$\frac{1}{\tau_{nr}} = \frac{1}{\tau_{SRH}} + \frac{2}{d}(S_{int} + S_{th})$$

$$\frac{1}{\tau_{nr}} = \frac{1}{\tau_{SRH}} + \frac{2}{d}(S_{eff})$$

$$S_{eff} = \frac{d}{2\tau_{nr}}$$

Therefore, the effective interface recombination can be determined by fitting the slope of $1/\tau_{nr}$ versus 2/d (Fig. 2.27 below).[34] The S_{eff} values of the sample are inversely proportional to the magnesium barrier composition, which appears to rule out lattice mismatch between $Mg_xCd_{1-x}Te$ and CdTe to be significant contributors to interface recombination. Instead, the theory to explain this suggests that a higher amount of recombination occurs from carriers jumping over lower $Mg_xCd_{1-x}Te$ barriers (thermionic emission). This theory was further confirmed by temperature-dependent PL measurement described next.[35]

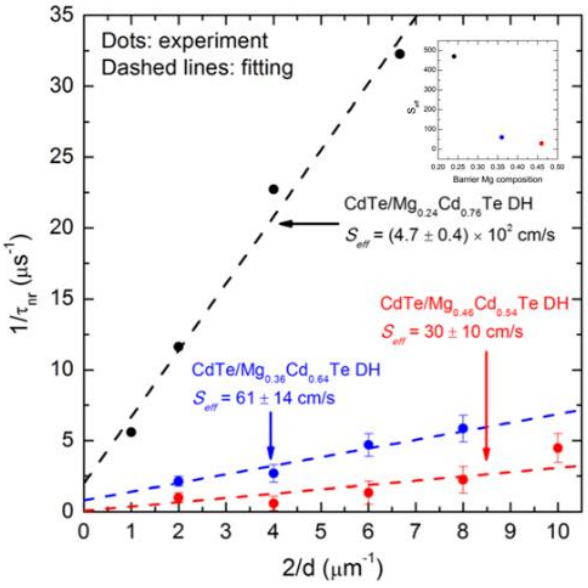

Fig. 2.27 Plots of Inversed Non-radiative Recombination Lifetime $\frac{1}{\tau_{nr}}$ Versus The Inversed Absorber Thickness $\frac{2}{d}$. From These Fitted Slopes The S_{eff} is Determined for $CdTe/Mg_xCd_{1-x}Te$ DH Samples of X = 0.24, 0.36, and 0.46.[34]

The thermionic emission equation is shown below:

$$\tau_{th} = \frac{d}{2} \times \sqrt{\frac{2\pi m^*}{kT}} \times e^{\frac{\Delta E_{C,V}}{kT}} \tag{2.19}$$

where m^* is the electron or hole effective mass and $\Delta E_{C,V}$ is the conduction or valence band offset.

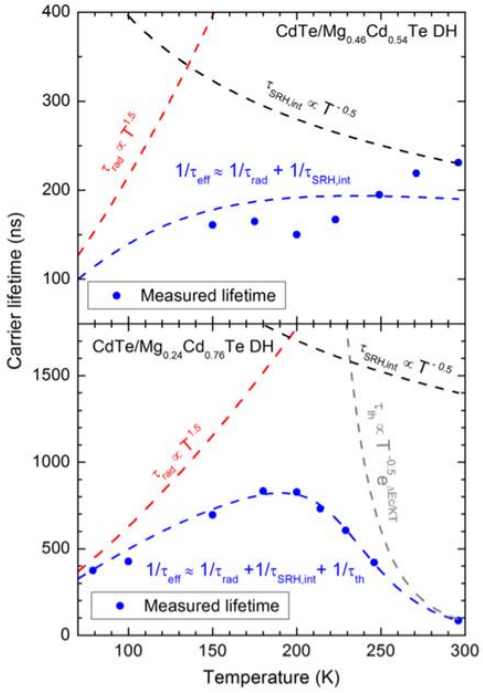

Fig. 2.28 Radiative, Shockley-Read-Hall, and Interface Lifetimes Versus Temperature Comparing $CdTe/Mg_xCd_{1-x}Te$ of X = 0.24 and 0.46.[35]

The bandgap of $Mg_xCd_{1-x}Te$ increases with additional Mg content, with 30% of the increase in the valence and 70% in the conduction band, as measured by X-ray Photoelectron Spectroscopy.[38] From the thermionic emission lifetime equation, it is clear that for a given temperature, an increase in band offset contributes to an increase in lifetime. This is evidenced by temperature dependent PL studies of $Mg_xCd_{1-x}Te$ with x = 0.24 and 0.46, shown by Fig. 2.28.

Through these thickness and temperature dependent PL studies, the lifetime of bulk single-crystal CdTe/$Mg_xCd_{1-x}Te$ DH was able to increase from 50 ns up to 3.6 us, higher than that of GaAs/AlGaAs (Fig. 2.29 below).

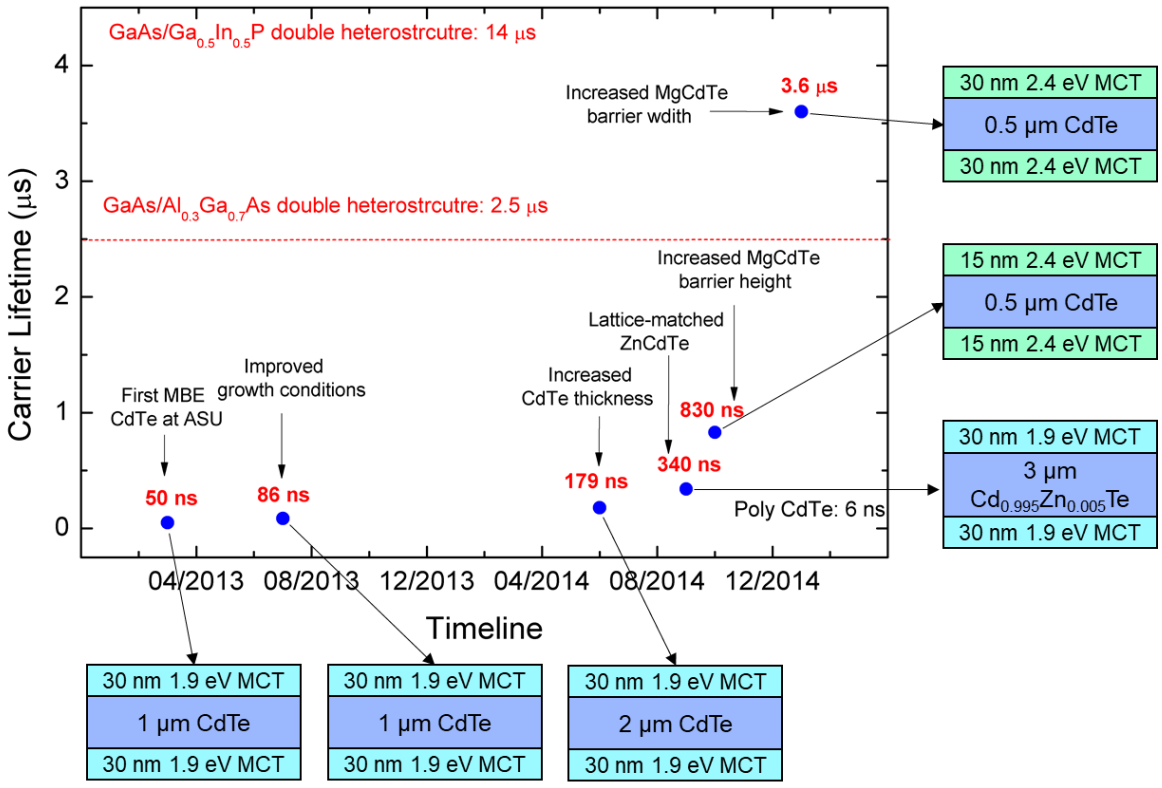

Fig. 2.29 Timeline of The Optimization of CdTe Minority Carrier Lifetime, up to a Record of 3.6 Microseconds.

The structure of $Mg_xCd_{1-x}Te/Mg_xCd_{1-x}Te$ double heterostructures was influenced by the deep understanding of $CdTe/Mg_xCd_{1-x}Te$ mechanisms. As shown by Fig. 2.30 below, the thickness of the barriers around the 1.7 eV absorber (30 nm) prevented tunneling, the 500 nm absorber provided optimum absorption and the higher barrier height of the 2.53 eV MCT barriers was considering the increase in absorber bandgap from 1.5 eV to 1.7 eV in order to minimize thermionic emission.

Another marked difference between the CdTe and the $Mg_xCd_{1-x}Te$ DH was the grading between the barrier $Mg_xCd_{1-x}Te$ and the $Mg_xCd_{1-x}Te$ absorber. This was because there is only one Mg cell which needs time to heat up and cool down in order to provide different Mg fluxes for difference $Mg_xCd_{1-x}Te$ compositions and thus bandgaps. In order to prevent growth interruption at the absorber/barrier interface (which can contribute to contaminants adsorbing and incorporating into that interface (maybe add contaminant growth rate equation) the temperature of the Mg cell was graded, and as such the composition between $Mg_xCd_{1-x}Te$ barrier and absorber was graded. Additionally, the interface between the CdTe buffer and the 2.53 eV barrier was graded to prevent possible defects resulting from lattice mismatch (which possibly was not an issue, consult critical thickness vs Mg composition). From these adjustments, a record $Mg_xCd_{1-x}Te$ lifetime of 560 us was achieved (Fig. 2.31 below).

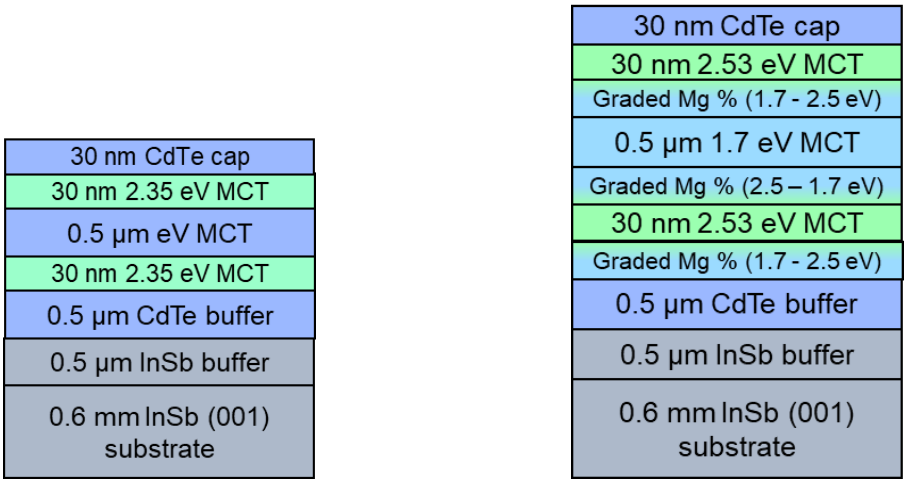

Fig. 2.30 A Comparison of The Record Lifetime Samples of (left) CdTe and (right) 1.7 eV $Mg_xCd_{1-x}Te$.

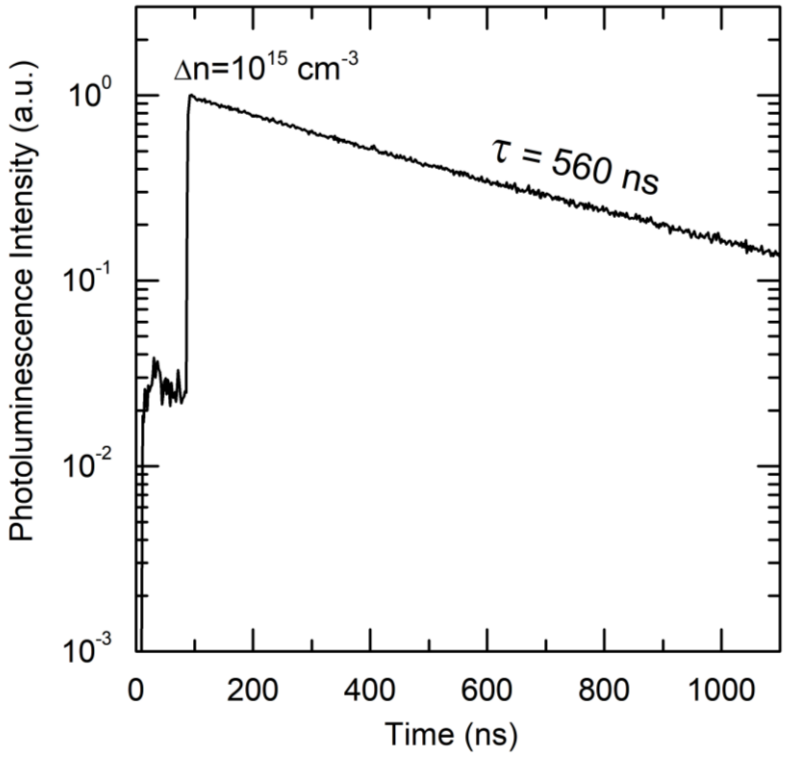

Fig. 2.31 Time-resolved Photoluminescence Spectra of 1.7 eV $Mg_xCd_{1-x}Te$.

2.8.3 Photoluminescence Quantum Efficiency

Like carrier lifetime, the photoluminescence quantum efficiency (PLQE) is an important metric for determining the viability of a film as a high efficiency solar cell. Also referred to as external luminescence quantum efficiency (η_{ext}), it refers to the light which escapes from the top surface of a sample into free space.[39] The Shockley-Quisser limit assumes that the is unity. Because the narrow escape cone of a recycled internal photon, sufficient η_{ext} requires a very high (>>90%) internal luminescence quantum efficiency.

The photon flux of the PL from the sample is:[40]

$$\phi_{PL} = R_{ref} \frac{S_{PL}/C_{PL}}{S_{ref}/C_{laser}} \quad (2.20)$$

Where R_{ref} is the reflectance of the reference, ϕ_{laser} is the photon flux of the laser, S_{PL} and S_{ref} are lock-in amplifier readings for the sample and reference, respectively, and C_{PL} and C_{laser} are the throughputs of the optical setup at the wavelengths of the sample PL and laser respectively.

The external luminescence efficiency η_{ext} is related to the ϕ_{PL} by:

$$\eta_{ext} = \frac{\phi_{PL}}{A_{DH}\phi_{laser}} \quad (2.21)$$

where A_{DH} is the absorptance of the sample at the laser wavelength, calculated with wave optics to be 55.3%. The maximum practical voltage at open circuit (implied V_{OC}) is related to the η_{ext} by:

$$V_{oc} = V_{db} + \frac{kT}{q}\ln(\eta_{ext}) \quad (2.22)$$

where V_{db} is theoretical detail-balance limited V_{OC} and T is temperature. The η_{ext} of the record lifetime $Mg_xCd_{1-x}Te$ sample was measured at room temperature and calculated for various power densities using the two set-ups shown in Fig. 2.32 below, featuring the use of a Lambertian reflector as a reference.

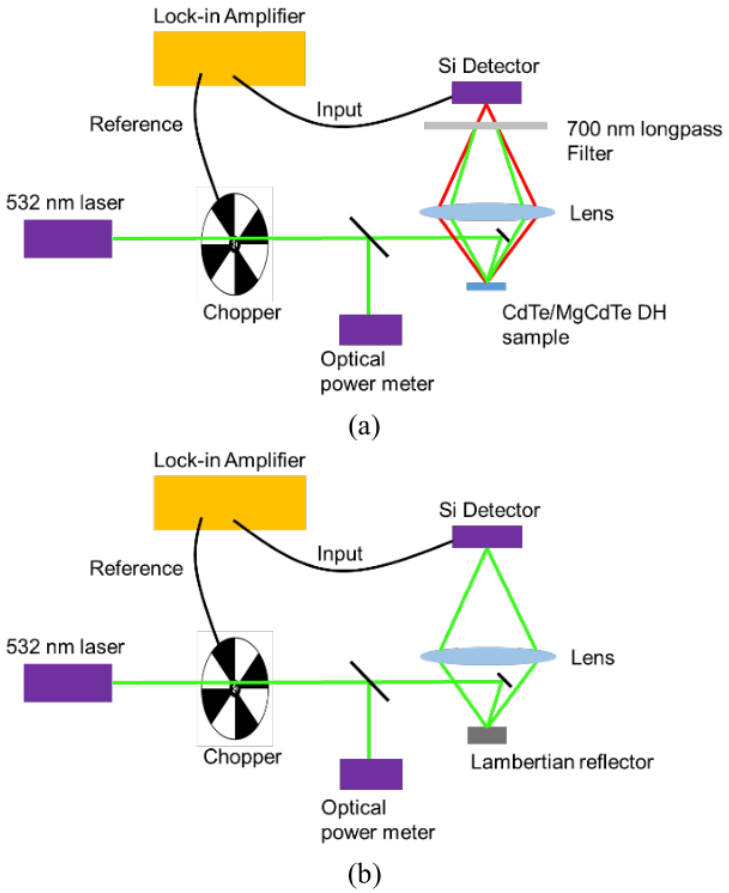

Fig. 2.32 The Photoluminescence Efficiency Setup (a) with a Sample and (b) with a Lambertian Reflector as a Reference[20].

As 20 mA/cm^2 is the power density corresponding to 1 sun, the η_{ext} value of 1.2% was extracted (Fig. 2.33). Thus, the implied V_{OC} of the record lifetime $Mg_xCd_{1-x}Te$ sample was calculated to be 1.3 V.

The bandgap-voltage offset (W_{OC}) is an important metric for determining the quality of a material as it can be applied to a high-performing device. As the absorber bandgap is the hard limit for the value of V_{OC} in a solar cell, the closer the implied V_{OC} then the closer the solar cell device is to theoretical limits. The W_{OC} can be calculated by the following simple equation:

$$W_{OC} = E_G - implied\ V_{OC} \tag{2.23}$$

and from this equation the W_{OC} can be estimated to be 0.4 eV. According to the standards from the industry, this value is within the range of what is considered high-performing[41]. In comparison, the W_{OC} of single crystal CdTe solar cells is close to 0.4 eV as well[42].

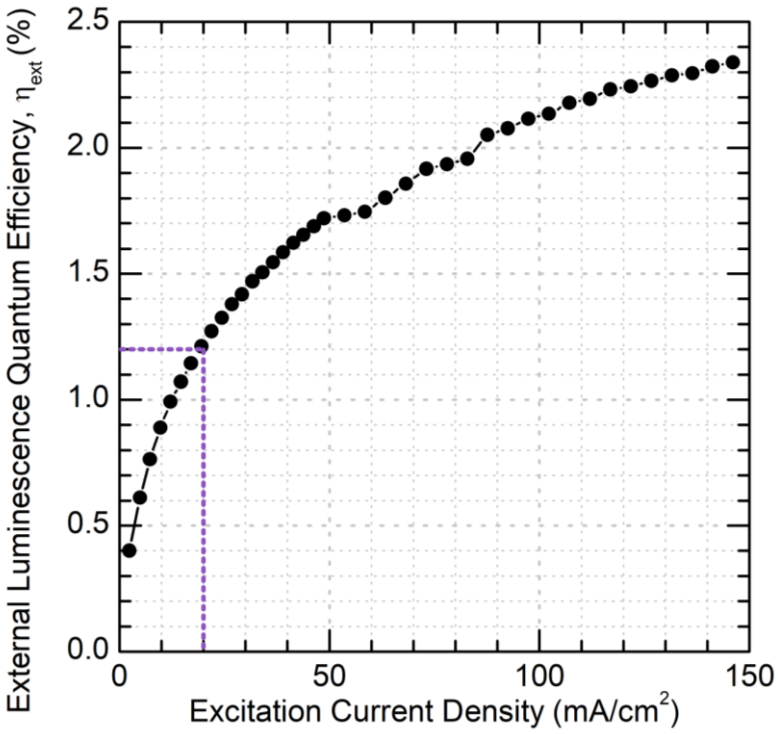

Fig. 2.33 A Measurement of The External Luminescence Efficiency as a Function of Excitation Current Density. Under 20 mA/cm^2 (1-sun illumination) The Efficiency is 1.2%.

Chapter Summary

This section discusses the study of the 1.7 eV $Mg_xCd_{1-x}Te/Mg_yCd_{1-y}Te$ double heterostructure. It begins by introducing molecular beam epitaxy and the in-situ characterization technique RHEED in order to grow the smooth single-crystal films. Structural (X-ray diffraction) confirms a high degree of crystalline order in the films both with abrupt and graded transitions between $Mg_xCd_{1-x}Te$ absorber and barrier layers. Ellipsometry is used to determine the absorption properties, notably revealing a high absorption coefficient of $\sim 2 \times 10^4$ cm^{-1}. XPS was used to measure the band offset values of CdTe/InSb, revealing more about this important film/substrate interface. Photoluminescence spectroscopy is used to determine the optical quality of the heterostructures, notably to ensure that a resulting solar cell will achieve a high V_{OC}. The record carrier lifetime (measured by TRPL) was measured to be 560 ns, and the implied V_{OC} of this structure is 1.3 V (measured by PLQE).

CHAPTER 3 - WIDE-BANDGAP 1.7 EV $Mg_xCd_{1-x}Te$ SOLAR CELL DEVICES

3.1 Introduction

This chapter introduces the design of an a-Si/$Mg_xCd_{1-x}Te$ DH remote junction solar cell layer structure and band diagram. Four different device structures with different top layers, absorber thicknesses and $Mg_xCd_{1-x}Te$ barrier dimensions are fabricated. The light I-V characteristics and the external quantum efficiency (EQE) of each device are analyzed and compared. Ultimately, the optimization of absorber thickness, barrier dimensions and anti-reflection layers lead to a record efficiency of 15.2%. A loss analysis in the EQE provides a path to further increases in conversion efficiency.

3.2 Design and Fabrication of 1.7 eV a-Si/$Mg_xCd_{1-x}Te$ Single Junction Solar Cells

The cell structure, a basic schematic of which is shown in Fig. 3.1, consists of a molecular beam epitaxy-grown $Mg_xCd_{1-x}Te$/$Mg_xCd_{1-x}Te$ DH on an n-type InSb (001) substrate, a PECVD (Plasma-enhanced chemical vapor deposition) deposited p-type (boron-doped) hydrogenated amorphous Si (a-Si:H) hole contact layer, and an indium tin oxide (ITO) top current spreading electrode. This design takes advantages of a remote junction type structure, in which the absorber in outside of the p-n junction and passivated by the $Mg_xCd_{1-x}Te$ top barrier.[42] This in turn enables a great amount of freedom in the selection of hole contact material and structure, including amorphous in the case of a-Si:H.

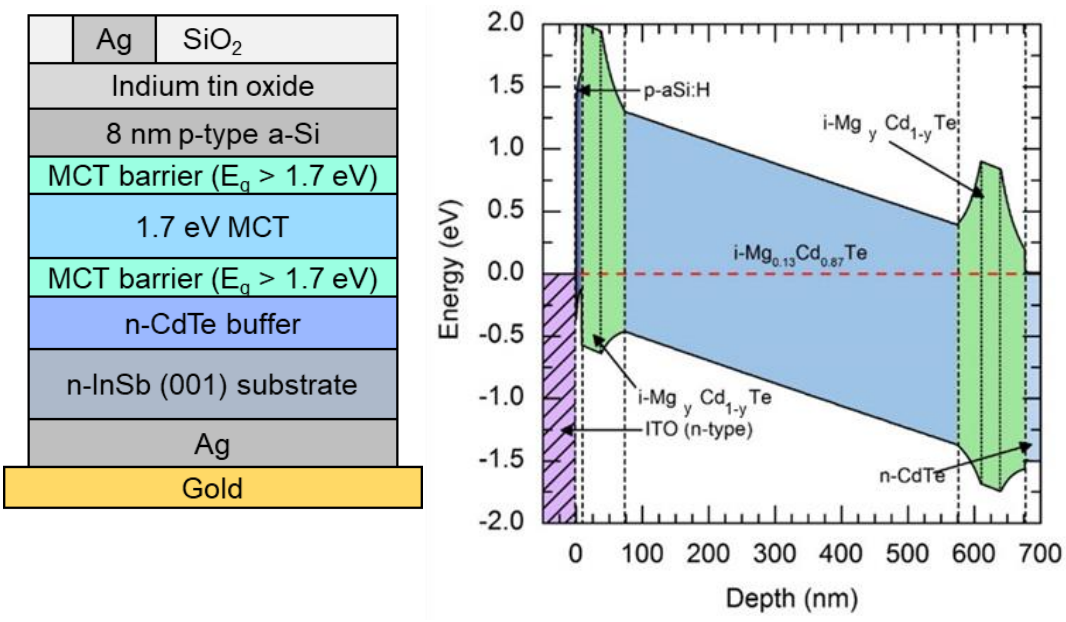

Fig. 3.1 (left) A Basic [a-Si:H]/[1.7 eV $Mg_xCd_{1-x}Te$] Solar Cell Layer Structure Made from Sample A and (right) Band Diagram of The Solar Cell.

3.3 Light Current-voltage Characterization Measurements

Current-voltage measurements were taken under an AM1.5G solar simulator at room temperature for four different solar cell structures A, B, C and D. As shown by Fig. 3.2 at the top, the MBE-grown part of Sample A is a repeat of the structure which achieved a record 560 ns carrier lifetime, with additional processing to add the a-Si hole contact, ITO current spreading layer and silver top contact.[43] Samples B-D, fabricated with identical contact layers, have some differences from sample A. Samples B-D were each consist of a 1.2 μm absorber. Sample B features 30 nm barriers with E_G = 2.2 eV, sample C features 30 nm barriers with E_G = 2.2 eV and an adrupt interface between the absorber and barriers, and sample D features 30 nm barriers with E_G = 2.0 eV and an abrupt interface between the absorber and barriers. Analyzing the samples together reveals

information illuminates the importance of different structural parameters which affect open circuit voltage (V_{OC}), short circuit current (J_{SC}), fill factor (FF) and efficiency (η).

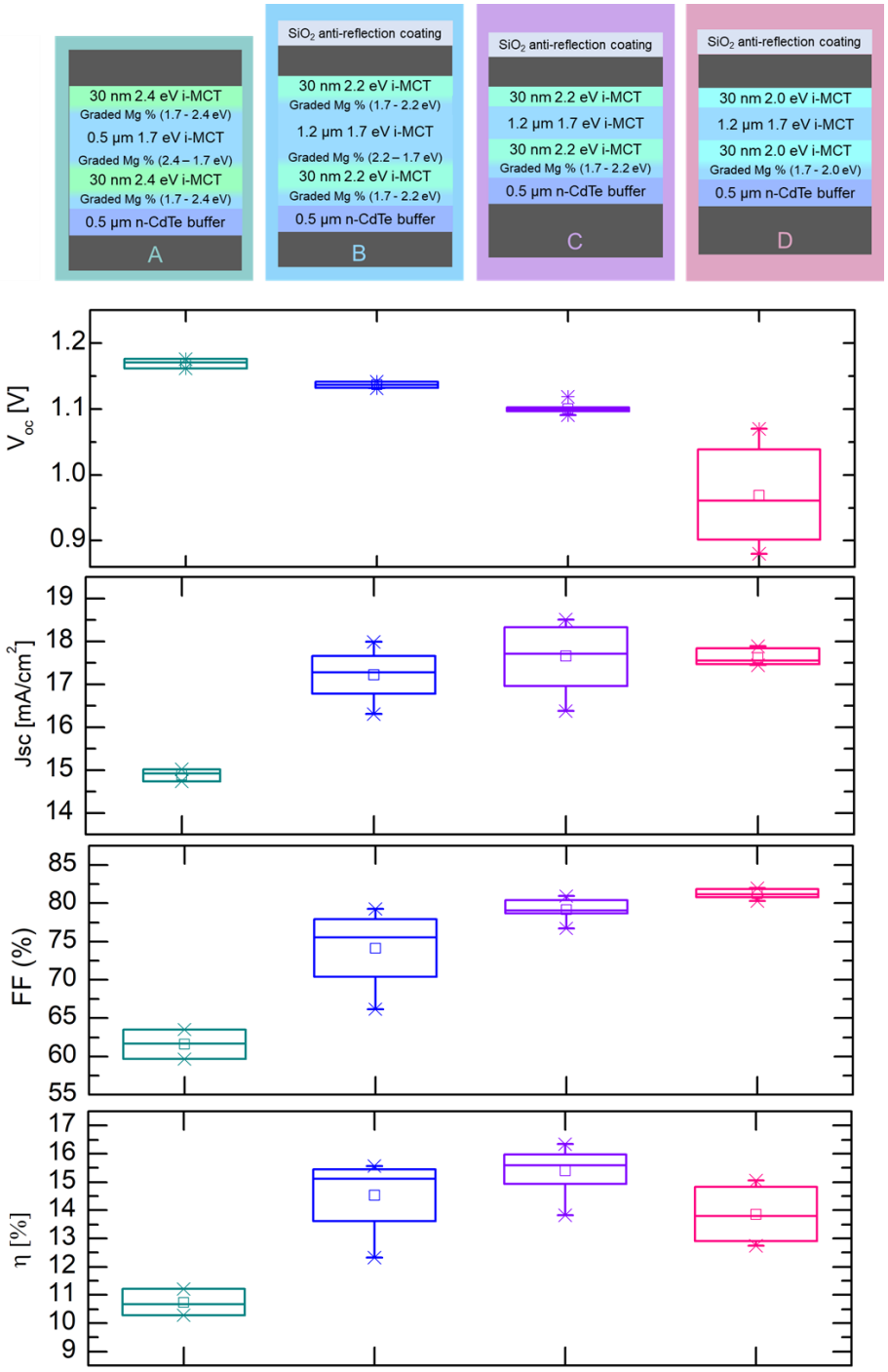

Fig. 3.2 Current-voltage Characteristics of Four Different 1.7 eV $Mg_xCd_{1-x}Te$ Solar Cell MBE-grown Absorber Designs.

The open circuit voltage (V_{OC}) of this set of samples trends down with a lowering of barrier height and thickness. As the open circuit voltage is limited by recombination mechanisms, it is understandable that lower, thinner barriers can contribute to a decrease in τ_{th} and thus a decrease in V_{oc}. The short circuit current (J_{SC}) is partially reliant on the photon flux and absorption of the material, as discussed in Section 2.7. The increased J_{SC} in Samples B, C and D in comparison to A may be attributed to two factors. The first is the thickening of the absorber from 500 nm (A) to 1200 nm (B-D). The second is the addition of an anti-reflection coating. Loss analysis of the structure of Sample A, further detailed in Section 4.4 below, concludes that there is a ~2 mA/cm^2 loss in J_{SC} from reflectance[15] as well as a ~2.1 mA/cm^2 loss in J_{SC} from transmittance; either or both of these changes could have contributed to the overall increase in device current.

The fill factor (FF) increases with each iteration in structure from Samples A through D. This trends proportionately with the thinning of height and thickness of the $Mg_xCd_{1-x}Te$ barriers. It is apparent that a reduction in barrier dimensions leads to better transport across the structure, and thus a higher fill factor. This behavior is confirmed by performing temperature-dependent measurements on Sample A[43]. Studies show that increases in temperature correspond to increases in thermionic emission which in turn correspond to increase FF. Thermionic emission is also increased with decreased barrier dimensions. It is a balancing act, as the same dimensional changes which increase fill factor can in turn reduce V_{OC}. This necessitates that each I-V parameter be optimized with respect to others until a maximum conversion efficiency is realized. In the case of this sample set, Sample C is the optimized design.

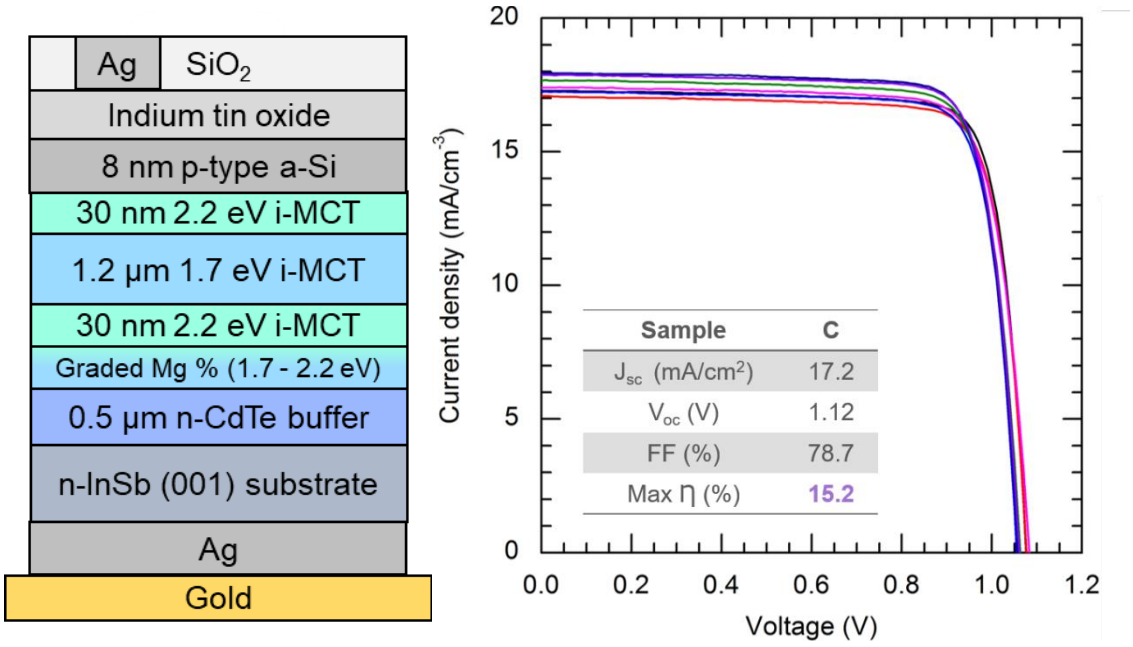

Fig. 3.3 (left) Hero 1.7-eV $Mg_xCd_{1-x}Te$ Solar Cell Structure and (right) Hero Current-voltage Characteristics Under 1-sun Condition.

As in Fig. 3.3 shown above, Sample C possesses not only a sufficiently-thick absorber layer moderately thin and low barriers and possesses a record efficiency of 15.2%. A moderate reduction in barrier thickness and height clearly benefits the transport of the carriers and thus the fill factor, while unlike Sample D, Sample C lets the V_{OC} survive.

3.4 Loss Analysis

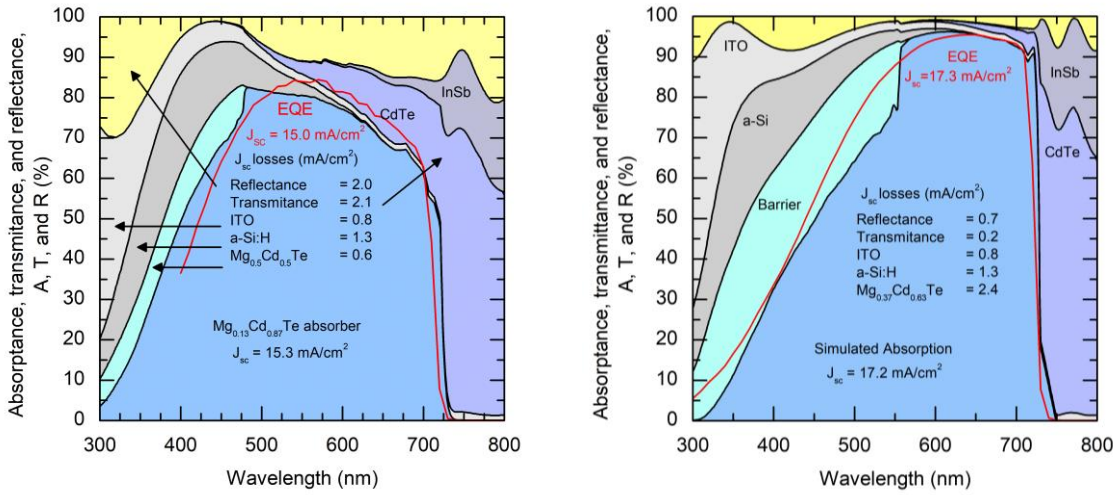

Fig. 3.4 Short-circuit Current Loss Analysis of (left) Sample A and (right) Sample C (the hero efficiency device).

The J_{sc} loss mechanisms are calculated and estimated using wave optics,[44] and are shown in Fig. 3.4 above. Parasitic absorption in the ITO, a-Si and top 2.2 eV $Mg_xCd_{1-x}Te$ barrier contribute to a total estimated J_{sc} loss of 4.5 mA/cm^2. It is possible that the discrepancy between the measured J_{SC} (red) and the slightly lower simulated J_{SC} is due to free carriers generated in the top barrier being swept into the absorber and collected as current. Thus, contrary to wave optics parameters, not all carriers generated in the top $Mg_xCd_{1-x}Te$ barrier are lost to parasitic absorption.

Iterations in device design can help to recoup the 4.5 mA/cm^2 reduction in current. Higher-bandgap layers above the absorber can help to reduce parasitic absorption loss. This includes the replacement of the 2.2-eV $Mg_xCd_{1-x}Te$ top barrier with that of a bandgap. Since it is important to optimize J_{SC}, FF, and V_{OC}, an asymmetrical barrier structure can be employed with a lower-bandgap bottom barrier, to ensure sufficient

carrier transport, matched with a more transparent, higher-bandgap top barrier. Additionally, the hole contact layer's bandgap can also serve to be greatly increased, using alternatives to a-Si. There are a variety of options to study, such as p-type zinc telluride (ZnTe),[45],[46] solution-processed CuZnS, and even organometallic materials such as PEDOT:PSS. As described in Section 4.2, the double heterostructure design of the solar cell allows for a wide degree of freedom in hole contact options.

When considering a practical maximum J_{SC} of 21.7 mA/cm^2, as well as a practical maximum V_{OC} of 1.3 V and a conservatively-high FF of 80%, a device with these parameters has a practical theoretical efficiency of 22.6%. This efficiency is higher than even the current record CdTe solar cell efficiency.

Chapter Summary

This chapter began by introducing the design of an a-Si/$Mg_xCd_{1-x}Te$ DH remote junction solar cell layer structure and band diagram. Four different device structures were fabricated, and the light I-V characteristics are analyzed and compared. Ultimately, the optimization of barrier dimensions in the double heterostructure leads to the optimization of the design and a record efficiency of 15.2%. Loss analysis of the short circuit current shows that the J_{SC} can be improved by up to 4.5 mA/cm^2. These improvements in J_{SC} alone would increase the in overall device efficiency to achieve up to 18.69%.

CHAPTER 4 - DOPING OF SINGLE-CRYSTAL $Mg_xCd_{1-x}Te$-BASED THIN FILMS

4.1 Introduction

This chapter discusses the n-type doping of 1.7 eV $Mg_xCd_{1-x}Te$ by indium. It begins with an introduction to dopant theory, and moves into a discussion of CdTe:In and compares it to $Mg_xCd_{1-x}Te$:In. The (Mg+Cd)/Te flux ratio is shown to be important when considering carrier concentration for $Mg_xCd_{1-x}Te$:In. A moderately high Group II rich overpressure enables the achievement of a higher carrier concentration better than that of a high Group II overpressure. The highest carrier concentration (with full activation) achieved is 1×10^{17} cm^{-3} which has a and a maximum implied V_{OC} 1.3 V. The highest carrier concentration in total is 5×10^{17} cm^{-3}, but this comes with degradations in optical quality.

4.1.1 Doping Theory

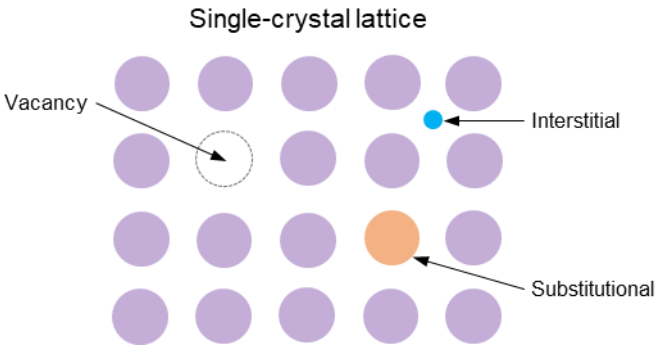

Fig. 4.1 Three Basic Point Defects in Single-crystal Lattices Which Can Contribute to Doping.

When doping in a compound semiconductor, several different point defects (shown in Fig. 4.1) are capable of changing the number of free electrons and/or holes. A simple way

to begin is to consider the oxidation states (a number assigned to an element in chemical combination that represents the number of electrons lost (or gained, if the number is negative) by an atom of that element in the compound) of each species within a proposed materials system, both of the intrinsic and extrinsic type. In CdTe, Cd has a fully ionized oxidation state of +2 while Te has a fully ionized oxidation state of -2. Thus, from using the simple equation for effective charge (q_e)[47]:

$$q_e = z_d - z_s \tag{3.1}$$

where z_d is the charge of the defect and z_s is the normal charge of the lattice site, one would think that, for example, Te-rich lattice conditions may easily result in p-type CdTe material, since Te-rich conditions would create Te_i and/or V_{Cd}. defects resulting in negatively charged acceptor defects. To note, the defect terminology is as follows: Te and V (vacancy) describe the defect species, and the subscript (i [interstitial] and Cd) describes the site in the lattice which the species occupies.

To continue with the example, the situation for Te_i and/or V_{Cd} is complex, and other parameters have to be taken into account. One such parameter is the transition energy level of a defect, which determines where each defect state, at a given degree of ionization, will sit within the bandgap of a semiconductor, and thus how probable they are to be ionized at a given Fermi energy. Fig. 4.2 shows various donor and acceptor transition energy levels of point defects in CdTe, calculated by Wei *et. al.*[48] using the all electron, general potential, linearized augmented plane wave method within the local density approximation.

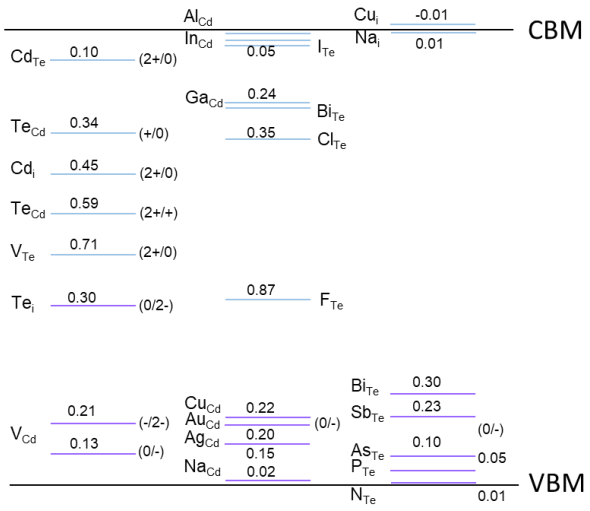

Fig. 4.2 Calculated Transition Energy Levels for Various Point Defects in CdTe.

Table 4.1 Calculated Formation Energies of Tetrahedrally Coordinated Point Defects at Neutral Charge State.

Defect	Formation energy (eV)	Defect	Formation energy (eV)
V_{Cd}	2.67	Cd_{Te}	3.92
V_{Te}	3.24	Te_{Cd}	3.70
Te_i^a	3.52	Cd_i^a	2.26
Te_i^c	3.41	Cd_i^c	2.04
Na_{Cd}	0.45	Al_{Cd}	1.17
Cu_{Cd}	1.31	Ga_{Cd}	1.23
Ag_{Cd}	1.32	In_{Cd}	1.23
Au_{Cd}	1.30	F_{Te}	−0.08
N_{Te}	2.62	Cl_{Te}	0.48
P_{Te}	1.83	Br_{Te}	0.62
As_{Te}	1.68	I_{Te}	0.99
Sb_{Te}	1.72	Cu_i^a	2.14
Bi_{Te}	1.96	Cu_i^c	2.24
Na_i^a	0.60	Na_i^c	0.45

Upon considering Te-rich conditions again and now addressing these calculated transition energy values, one can see that the interstitial defect Te_i is a deep trap, making it very difficult to activate to high hole densities. V_{Cd} sits at a comparatively shallow

acceptor state, though simulations suggest it is not shallow enough to reach high hole densities at room temperature[48]. It is also helpful to predict the defect formation energy, which determines the equilibrium solubility of a point defect into a host matrix. As shown by Table 3.1, also calculated by Wei *et. al.* [48], both Te_i and V_{Cd} exhibit relatively large defect formation energies.

It is important to note that simulations in equilibrium, while an extremely useful wealth of information, are always taken with a grain of salt, since the introduction of kinetics brought on by factors including temperature and deposition through non-equilibrium techniques (such as molecular beam epitaxy described below), can increase point defect solubility[49].

For a semiconductor material to have a high carrier concentration the doping species must, at least, be a shallow donor with a sufficient solubility in CdTe. Due to CdTe being a II-VI compound semiconductor, the go-to elemental groups for CdTe p-type doping are from Group I and Group V of the periodic table.

In Group I, as shown by Fig 4.2, there are several elements which create shallow acceptor states in CdTe, including silver (Ag), gold (Au), Cu (copper), and Na (sodium), whose transition energy levels are at 0.15, 0.20, 0.22 and 0.02 eV above the VBM, respectively. These may seem like they would be perfect donors for CdTe, however their small size is their downfall. These tiny Group I elements have a propensity toward diffusing through the bulk CdTe material, dissolving device junction quality at operation temperatures[50].

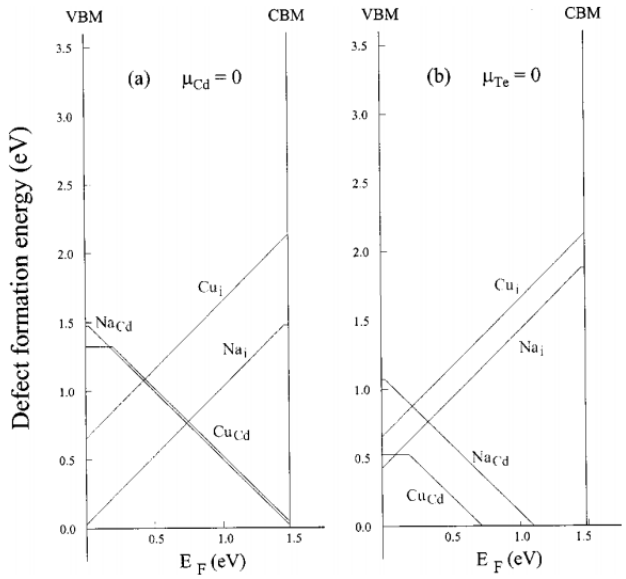

Fig. 4.3 Calculated Defect Formation Energy of Na and Cu Defects as They Change with Fermi Energy.

In addition, it is important to consider the stabilities of these small atoms sitting in interstitial versus substitutional sites. For example, simulations displayed in Fig. 4.3 predict that Na would make a bad acceptor element since, with increasing hole concentrations, the Fermi level would decrease and make the n-type interstitial defect Na_i more stable than p-type substitutional defect Na_{Cd}. This has been further confirmed by experimental studies[51]. Thus, in monocrystalline CdTe, these elements simply are not practical p-type dopants.

Many Group V elements are shown to be shallow acceptors in CdTe and experimental studies shown they do not have the diffusion problems exhibited by Group I elements[52]. Looking again at Fig. 4.2, it is easy to see that N, P, and As substituting Te have shallow acceptor transition energy levels in CdTe, however relatively high formation energies (shown by Table 1) make them a challenge to incorporate and

dissociate into active sites. Non-equilibrium growth techniques like MBE have been able to address this challenge[53],[54],[55].

Groups III and VII possess notable dopants for n-type extrinsic doping of CdTe. Group III dopants for CdTe, including aluminum (Al), gallium (Ga) and indium (In), have shallow donor-like transition energies, however, they prefer to produce DX centers which compensate donors. Using the equation:

$$\Delta E(DX) = E(DX, q) - E(\alpha, q) \quad (3.2)$$

wherein *E(DX,q)* is the total energy of the *DX* at the charge state q (most often q = -1) and *E(α,q)* is the total energy of the corresponding tetrahedrally-coordinated defect α at the same charge state. Point defects Al_{Cd}^{-}, Ga_{Cd}^{-}, and In_{Cd}^{-} have negative *E(DX,q)* values of -0.50, -0.41 and -0.49 eV respectively. Negative *E(DX,q)* values indicate that the formation of these *DX* centers is stable- the more negative the more stable - and thus donor-like defects are metastable.[56],[57],[58] In comparison, shallow-donor Group VII dopants Cl_{Te}^{-}, Br_{Te}^{-}, and I_{Te}^{-} are 0.55, 0.28 and -0.17 eV respectively. Thus, *DX* center formation is not a limiting factor in Group VII dopants with the exception of I_{Te}^{-}. MBE and other non-equilibrium techniques are also useful for n-type doping of CdTe.

3.1.2 In-situ Doping During MBE Growth

To reiterate details from Chapter 2, MBE is an ultra-high vacuum, surface-sensitive material growth method which produces ultra-high quality, ultra-low defect semiconductor thin films. High crystal quality in MBE is achieved through the careful optimization of several parameters 1) The substrate temperature needs to be high enough to allow for movement of surface ad-atoms to preferred sites in the lattice, while low

enough to prevent bulk diffusion and vacancy formation 2) the growth rate needs to be very low (on the order of ~1 μm/hr) in order to allow time for ad-atoms to find their preferential sites 3) the pressure needs to be ultra-low (~10^{-10} Torr) in order to suppress the adsorption rate of contaminant species on the surface and 4) the ratio of fluxes of effusion source cells need to be tuned in order to account for the differences in bonding relationships between the source elements[17].

When performing substitutional *in situ* doping of MBE-grown layers, consideration of these parameters is also essential to maximize the incorporation and activation of dopant species. Incorporation is defined by the concentration of a certain atom which is present in the host material, while activation is the amount of this atom which is in a lattice position where it forms a shallow donor or acceptor dopant contributing to the overall carrier concentration[54].

There is a big advantage to being able to *in situ* dope, since it can help maintain the integrity of the crystal lattice in ways that other methods, such as ion implantation, cannot[59]. The parameters which commonly factor into dopant incorporation and activation, regardless of dopant species, are the flux ratio of source cells and dopant cell, and the temperature and type of the substrate.

4.1.3 Techniques for Measuring Dopant Incorporation and Activation

4.1.3.1 Secondary Ion Mass Spectroscopy

A technique to measure incorporation of dopants is secondary ion mass spectrometry, or SIMS. In SIMS, as shown by Fig. 4.4, a beam of ions hits a sample surface. These ions hitting the sample knock out secondary ions from the sample itself. These secondary ions

are analyzed by a mass spectrometer. As ions are continuously knocked out deeper and deeper into the bulk material, a dopant concentration versus depth profile is established[60].

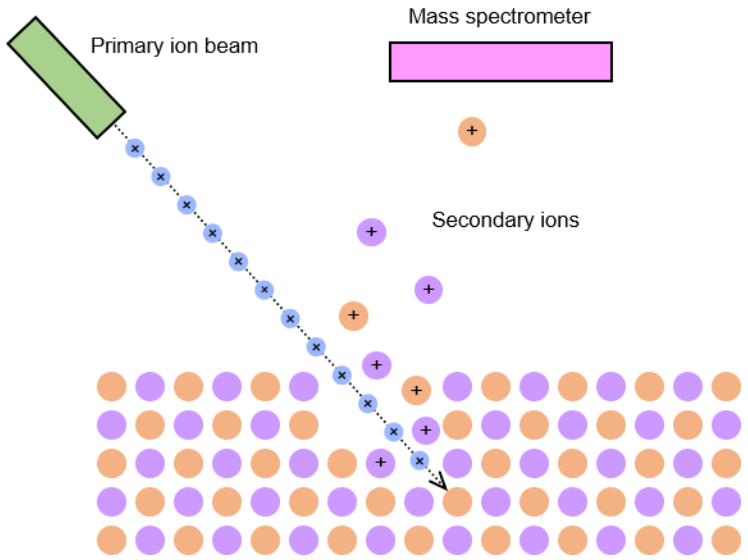

Fig. 4.4 Basic Secondary Ion Mass Spectrometry Schematic[60].

Fig. 4.5 depicts a structure for sample A1645, a first-generation single-crystal ZnTe/CdTe solar cell[30] which features a doped CdTe buffer and a bottom $Mg_xCd_{1-x}Te$ barrier on top of an InSb(001) substrate. Note that there is a dip in the indium concentration in the $Mg_xCd_{1-x}Te$ barrier. It appears that indium does not incorporate as readily into $Mg_xCd_{1-x}Te$ as it does into CdTe. The indium from the bulk InSb layers and indium dopant cell is highly mobile and diffuses into CdTe and $Mg_xCd_{1-x}Te$. This has been seen elsewhere in single-crystal CdTe fabricated by both MBE and the Bridgman method[61],[62].

It is possible that indium does not incorporate as easily into $Mg_xCd_{1-x}Te$ because there is a preference for Mg to incorporate over that of indium. A possible reason is that the sticking coefficient of Mg in the system is higher than that of indium, suppressing In incorporation into the lattice. Fig. 4.6 shows that there is a lower indium concentration for a given cell temperature for $Mg_xCd_{1-x}Te$ when compared to CdTe.

The SIMS profile of an indium-doped $Mg_xCd_{1-x}Te$ sample on InSb is shown by Fig. 4.7. Notice that indium appears to diffuse in both thick CdTe as well as thick $Mg_xCd_{1-x}Te$, at concentrations of indium at or above 1×10^{16} cm^{-3}, resulting in a smearing of the profile rather than defined steps. Below this concentration, the steps of different indium concentrations are more abrupt, suggesting a lower amount of movement and diffusion of indium at lower indium concentrations.

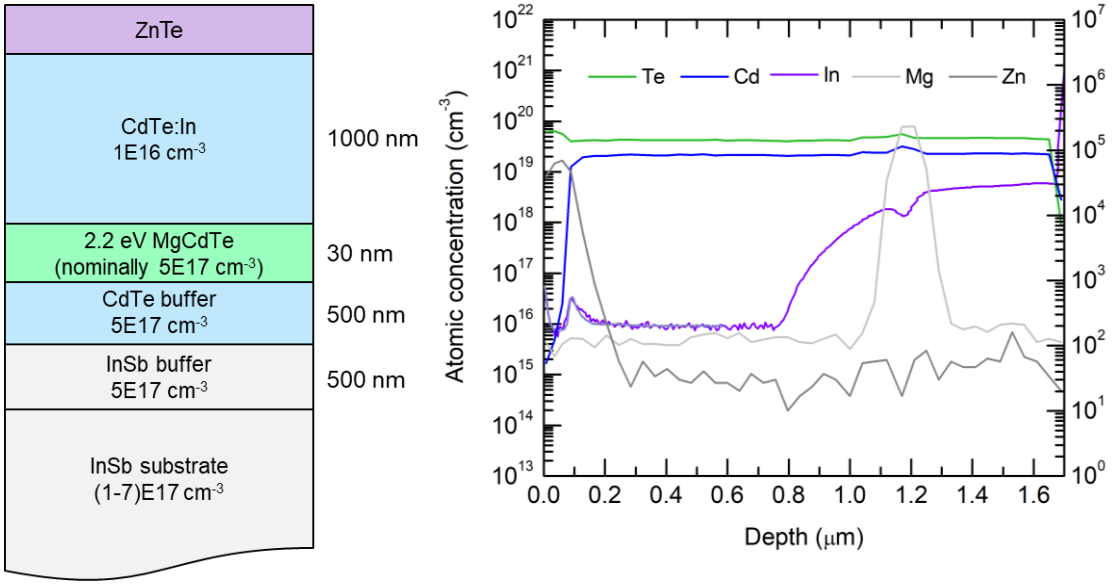

Fig. 4.5 A SIMS Profile of an Indium-doped CdTe Sample Featuring a $Mg_xCd_{1-x}Te$ Bottom Barrier, on an InSb Substrate and Buffer Layer.

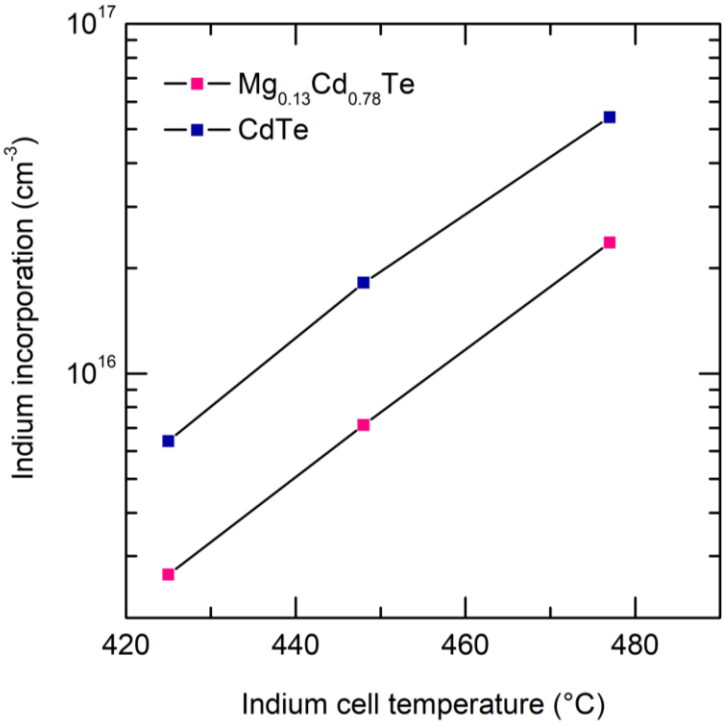

Fig. 4.6 A Comparison of In Incorporation (measured by SIMS) of CdTe and $Mg_xCd_{1-x}Te$ for a Given In Cell Temperature.

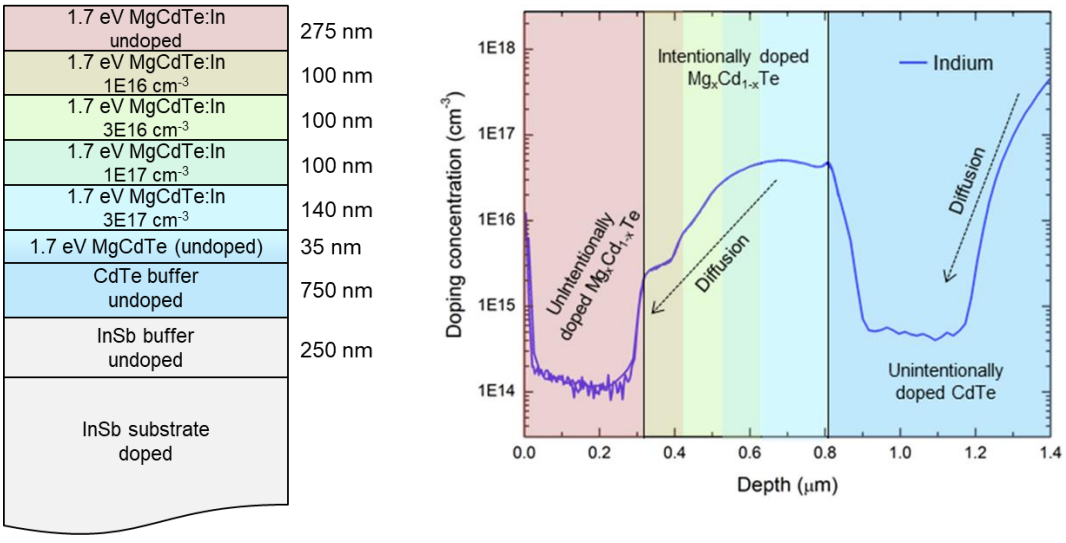

Fig. 4.7 SIMS Profile of Indium-doped Layers of $Mg_xCd_{1-x}Te$ on an InSb Substrate and Buffer Layer.

4.1.3.2 Capacitance-voltage Profiling

In the capacitance-voltage (C-V) profiling technique a metal–semiconductor, p-n junction, or MOSFET is formed to create a depletion region. With a bulk semiconductor, connections can be made using mercury (mercury probe C-V) or an electrolyte (electrochemical C-V).

In C-V profiling, the depletion region is empty of conducting electrons and holes, however, it may contain ionized donors and electrically active defects or traps which enable this region to act as a capacitor. The capacitance can be measured as a function of applied voltage, and whether the material is p-type or n-type can be determined by the trend of the capacitance as the voltage is swept from negative to positive values. The relationship between capacitance at a given voltage and the carrier concentration is shown by the equation below[63]:

$$N_{A,D} = \frac{C^3}{q\varepsilon_s A^2 \frac{dC}{dV}} \tag{3.3}$$

where C is the capacitance, ε_s is the dielectric constant of the measured semiconductor, A is the cross-section of the measurement contact area, and $\frac{dC}{dV}$ is the slope of the C-V curve whose positive or negative value determines the dominant carrier type in the material. For each value of $N_{A,D}$, the depth into the material at that carrier concentration can be determined by using the equation:

$$d = \frac{\varepsilon_s A}{C} \tag{3.4}$$

whose values can generate a doping profile into the bulk semiconductor material. An example of such results is shown below in Fig. 4.8, where on the left is given the values from a C-V scan and at the right a doping profile is generated from these results.

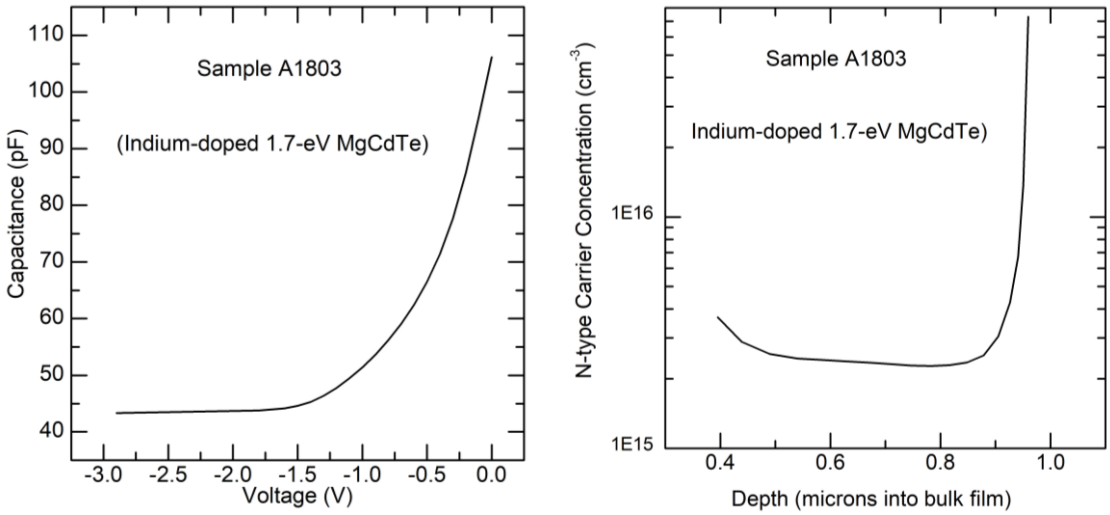

Fig. 4.8 An Example of Carrier Concentration Versus Depth Using Capacitance-voltage Measurements for Sample A1803, One of the Indium-doped 1.7 eV MgCdTe Samples Discussed in the Following Sections.

4.2 In-situ Doping of CdTe with Indium During MBE

MBE growth of CdTe under Cd-rich conditions, using flux ratio calibrations performed using RHEED as discussed in Chapter 2, is shown to product films with the lowest amount of surface roughness[30]. Under Cd-rich conditions, as shown by Fig. 4.9, there is possibly present Cd_{Te}, Cd_i and V_{Te} dopants due to a higher abundance of Cd versus Te and the growing surface. Note that while each of these dopants is at the level of a deep trap, it is likely that they do not exist in high concentrations, since the vapor pressure of Cd is higher than that of Te. Plus, the optical quality of MBE-grown CdTe is relatively high, suggesting there are minimal deep-level defect states. Both these defects, plus

indium diffusion from the InSb substrate, likely contribute to the slightly n-type [~5 $\times 10^{14} cm^{-3}$] nature of MBE-grown CdTe.

When indium incorporates as a substitutional defect sitting in a Group 2 (Cd) site, it is a very shallow n-type defect. The resulting material can reach n-type carrier concentrations of up to ~10^{18} cm^{-3}[64]. Further analysis of indium-doped CdTe is provided in the following sections.

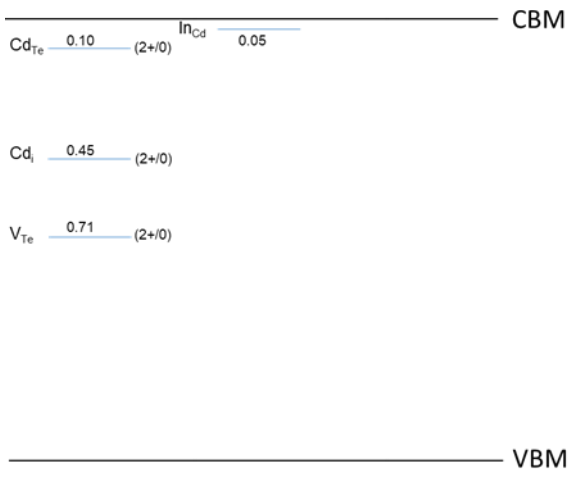

Fig. 4.9 Defect Levels Present During a Cd-rich CdTe Growth with In-situ In Doping.[2]

4.2.1 Carrier Concentration Versus Dopant Activation in CdTe

Using the growth conditions described above, CdTe is able to be doped n-type with indium (In). As shown by Fig. 4.10, a plotting of SIMS and C-V data reveals that the carriers are fully activated until 1×10^{17} cm^{-3}. This is directly proportional to the trend of the photoluminescence intensity, indicating the importance of carrier activation for optical quality.

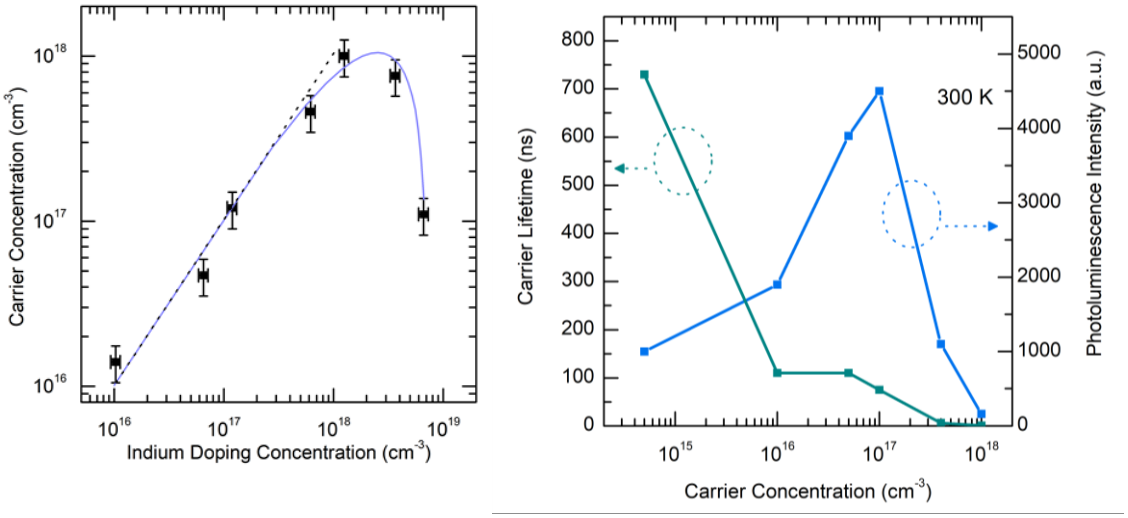

Fig. 4.10 (left) Doping Species Theoretically Present Under MBE Growth Conditions of *In-situ* In Doping of CdTe Under Cd-rich Growth Conditions and (right) Carrier Activation of In-doped CdTe. Note There is 100% Activation up Until ~1 × 10^{17} cm^{-3}.[65]

4.3 Dependence of Mg and Cd Overpressure on Carrier Incorporation and Concentration in $Mg_xCd_{1-x}Te$

Doping a ternary alloy of 1.7-eV $Mg_xCd_{1-x}Te$ n-type with *in-situ* In proves to require some slight changes to the growth conditions relative to CdTe:In or undoped $Mg_xCd_{1-x}Te$. The procedure for the growth of undoped $Mg_xCd_{1-x}Te$, described in 3.2 above, involves using the substrate temperature (265 ºC), Te-limited growth rate (9.6 nm/min) and Cd/Te flux ratio (1.5) of CdTe, with the only change to the process being the addition of a Mg flux supplied by heating a Mg cell. Remembering that molecular beam flux is proportional to the species-limited growth rate, the Group 2 over Group 6 flux ratio ($\Gamma_{II/VI}$) can be determined by:

$$\Gamma_{II/VI} = \frac{\Gamma_{II}}{\Gamma_{VI}} + \frac{\Gamma_{Mg} + \Gamma_{Cd}}{\Gamma_{Te}} \quad (3.5)$$

where Γ_{Mg} is the Mg-limited growth rate, Γ_{Cd} is the Cd-limited growth rate and Γ_{Te} is the Te-limited growth rate. Thus, for the growth conditions mentioned above, the $\Gamma_{II/VI}$ is 1.65.

For the first stage of the 1.7-eV $Mg_xCd_{1-x}Te$ DH *in-situ* In doping study, the growth conditions listed above are utilized, along with the addition of In flux from an In doping cell. From carrier concentration data extracted from capacitance-voltage measurements as shown in Fig 3.11, these growth conditions do not contribute to a highly-doped n-type material, even with increases in In flux brought on by an increase in In cell temperature.

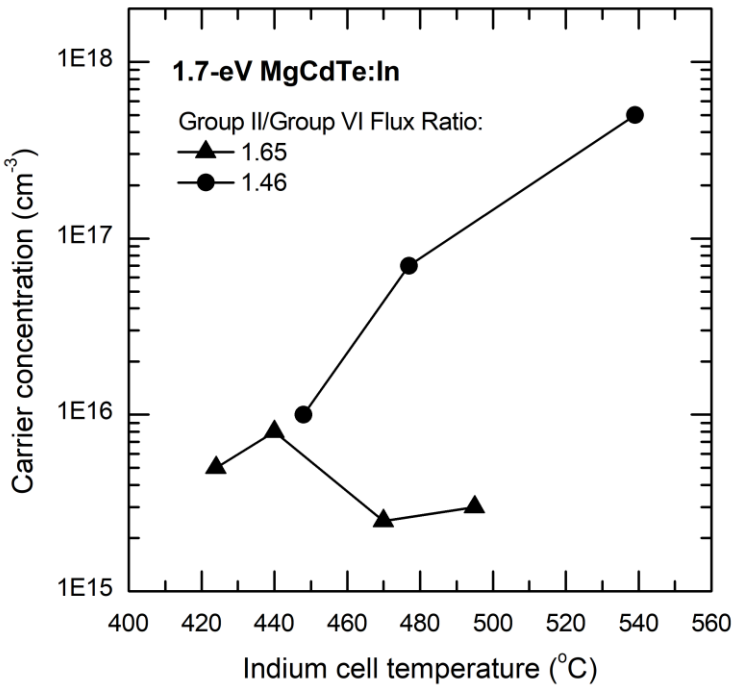

Fig. 4.11 N-type Carrier Concentration Versus Indium Cell Temperature for CdTe:In and 1.7 eV $Mg_xCd_{1-x}Te$:In for Two Different Group II over Group VI Flux Ratios.

It is possible that the low trend in carrier concentration is caused by the high (Mg + Cd) Group 2 (Mg + Cd) overpressure during growth. An increase in $\Gamma_{II/VI}$ can lead to a decrease in available Group 2 lattice site for indium to fill in order to become an In_{Cd} shallow donor. Thus, it is hypothesized that a lower $\Gamma_{II/VI}$ allows for a higher n-type carrier concentration. To test this hypothesis, samples were grown with a lowered Group 2 overpressure resulting in a $\Gamma_{II/VI}$ of 1.46. These updated growth conditions lead to an increase in the carrier concentration in 1.7-eV $Mg_xCd_{1-x}Te$ for a given In cell temperature, as seen by Fig. 4.11. An activation of 100% is achieved as shown by comparing SIMS and C-V results for several samples. As shown in Fig. 4.12 below, these results are on par with the trends seen in CdTe:In.

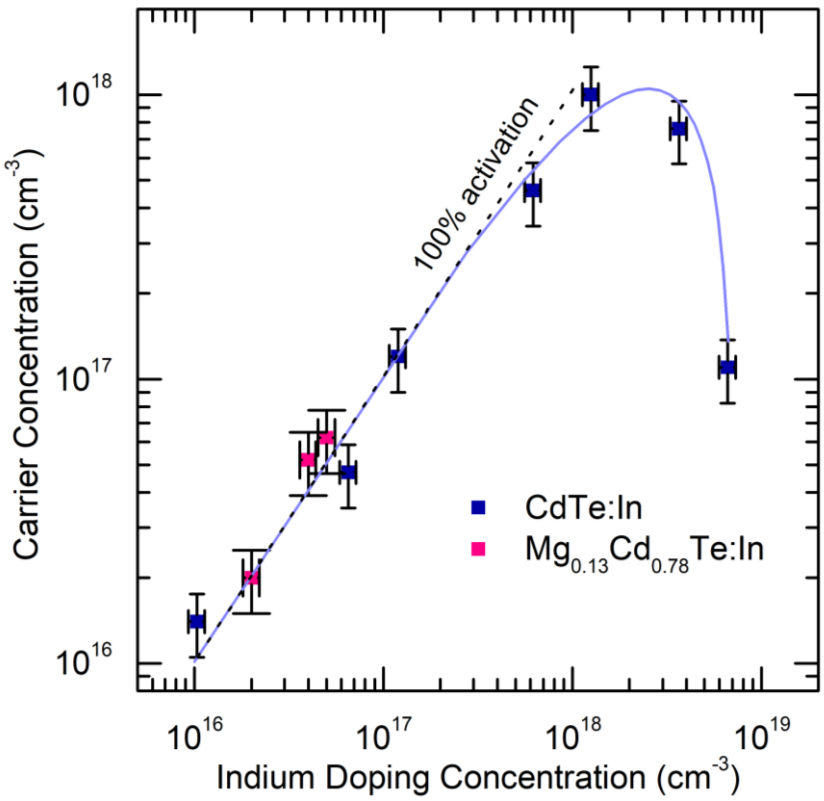

Fig. 4.12 (left) MBE-grown Indium-doped Structure Design and (right) a Comparison of In Incorporation and Activation Using SIMS, Hg-probe Capacitance-voltage.

4.4 Dependence of Temperature on Carrier Incorporation and Concentration in $Mg_xCd_{1-x}Te$

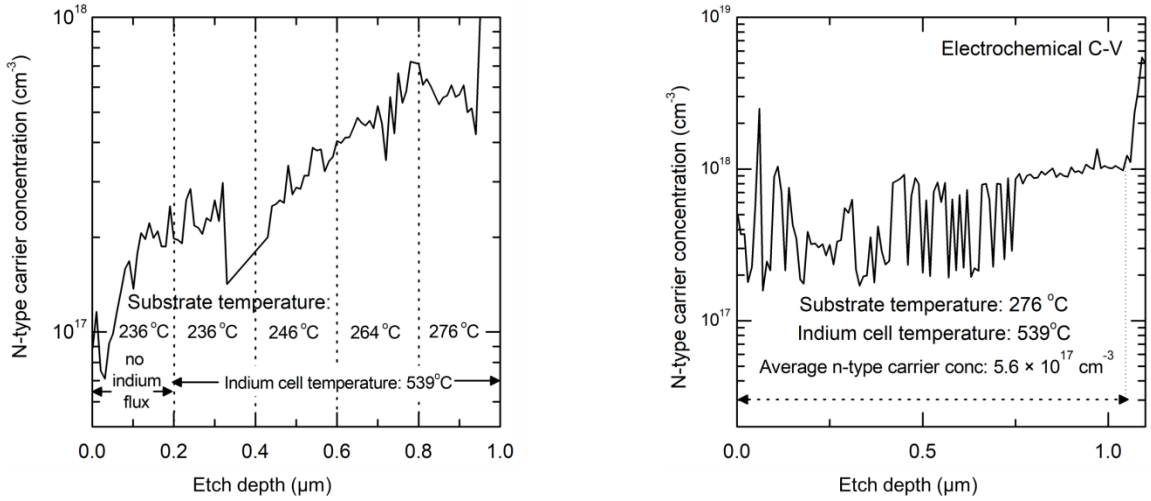

Fig. 4.13 (left) MBE-grown Indium-doped Structure Design and (right) a Comparison of In Incorporation and Activation Using SIMS, Hg-probe Capacitance-voltage and Electrochemical Capacitance-voltage.

A sample was grown under a constant indium flux, wherein different layers of the $Mg_xCd_{1-x}Te$ were grown at various substrate temperatures ranging from 276 ℃ (the traditional substrate temperature) down to 236 ℃ (substrate temperatures above 276 ℃ where not attempted as this temperature is already very close to the temperature at which CdTe sublimates congruently [source]. A schematic of this sample is shown in Fig. 4.13, in parallel with the data from an electrochemical C-V measurement. The decrease in substrate temperature trends with a decrease in the carrier activation of indium in

$Mg_xCd_{1-x}Te$. Possibly at lower temperatures the Mg sticking coefficient becomes even stronger and can preferentially drive out indium at an even greater degree. Thus, it is concluded that the traditional growth temperature of CdTe and $Mg_xCd_{1-x}Te$ (~276℃) is also the ideal temperature for high indium dopant activation.

4.5 Determination of Implied Open-circuit Voltage by PLQE of Indium-doped 1.7 eV $Mg_xCd_{1-x}Te$

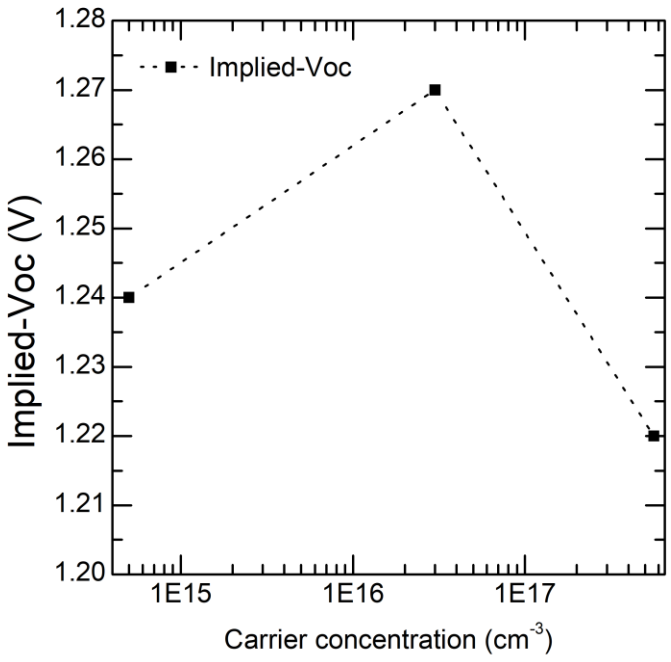

Fig. 4.14 Implied V_{OC} of Three Solar Cell Structures with Different Levels of N-type Carrier Concentration in The Absorber.

Using the PLQE technique introduced in Chapter 2, the implied V_{OC} of three different samples were compared. As shown by Fig. 4.14, doping increased the implied V_{OC} of the 1.7 eV $Mg_xCd_{1-x}Te$ by up to a record of 1.27 V, 30 mV higher than that of an undoped

version of the same structure. This is made possible because the internal quantum efficiency (IQE) is related to the radiative and non-radiative recombination in an absorber by the equation below[65]:

$$IQE = \frac{R_{rad}}{R_{total}} = \frac{R_{rad}}{R_{rad} + R_{non-rad}} = \frac{R_{rad}}{R_{rad} + R_{SRH} + R_{int}} \quad (3.6)$$

where R_{rad} is the radiative recombination $R_{non-rad}$ is the non-radiative recombination, which can be broken down into R_{SRH} (the rate of Shockley-Read-Hall recombination) and R_{int} is the rate of the interface recombination at the $Mg_yCd_{1-y}Te$ barriers. At lower doping concentrations, there is an increase in PL efficiency with doping due to stronger band bending, with carriers which may be recombined non-radiatively being swept into the absorber to be combined radiatively. This in turn brings down the $R_{non-rad}$ thus increasing the IQE. Above a certain doping threshold, ~10^{17} cm^{-3} in the case of 1.7 eV $Mg_xCd_{1-x}Te$, there is a high likelihood that indium-induced defects within the bandgap are increased, serving as non-radiative recombination traps which in turn increase $R_{non-rad}$ and decrease the IQE. This trends very similarly with the behavior of CdTe:In as shown in Section 3.2.1. In conclusion it is apparent that, within limits, it is possible that doping can increase the V_{OC} – and subsequently conversion efficiency – of a 1.7 eV $Mg_xCd_{1-x}Te$ solar cell.

Chapter Summary

This chapter discussed the n-type doping of 1.7 eV $Mg_xCd_{1-x}Te$ by indium. It began with an introduction to dopant theory, and moved into a discussion of CdTe:In. Then, CdTe:In and $Mg_xCd_{1-x}Te$:In are compared. The (Mg+Cd)/Te flux ratio is shown to be important when considering carrier concentration. Ultimately, a moderate Group II rich

overpressure is better than a high Group II overpressure, additionally a substrate temperature of ~276℃, ultimately leading to a carrier concentration (with full activation) of 1×10^{17} cm^{-3} with indium, optimizing the i-V_{OC} of a given structure with doping.

CHAPTER 5 - MGTE-BASED EPITAXIAL LIFT-OFF OF CDTE AND $MG_XCD_{1-X}TE$ SOLAR CELLS

Motivation

Though an InSb(001) substrate has proven an essential element in the growth of high-quality single-crystal CdTe and $Mg_xCd_{1-x}Te$ films, it is beneficial to be able to free these films from their substrates post-growth. This chapter discusses the study of II-VI-based epitaxial lift off (ELO) using water-soluble magnesium telluride (MgTe).

When light enters a CdTe film (n = 3) it can be transmitted and or reflected at the air/CdTe interface. With the InSb (n = 4.4) substrate intact, light transmitted through the CdTe is absorbed in the InSb substrate where it recombines nonradiatively and is loses its contribution to the current of the device. For this reason, in traditional substrate-intact devices wherein the InSb substrate is incorporated as a back contact, the thickness options for the CdTe absorber are limiting. In this situation, the CdTe absorber thickness must be high enough to sufficiently reduce transmission losses and not throttle the J_{SC}. While a thicker film can maximize the J_{SC}, the V_{OC} is throttled in turn.

A way to hack this path to optimization and achieve a high J_{SC} without compromising V_{OC} is through a device architecture which allows for internal reflection and enhanced photon recycling. A free-standing CdTe absorber allows for the adhesion of back reflectors (such as silver, whose n = 0.13) which take the place of the less reflective and more absorptive InSb substrate. This back reflection can in turn enhance the photon recycling effect in the solar cell, leading to a maximized J_{SC}, a higher V_{OC} and an overall increased conversion efficiency. Several GaAs/AlGaAs DH thin film solar cells have been fabricated using AlAs-based ELO,[66],[67],[68] including the state-of-the-art world

record 29.1% single-junction solar cells fabricated by Alta Devices.[14] The high degree of heat dissipation available in thin film solar cells also allows them to hold great promise in concentrated solar power (CSP) set-ups.[69]

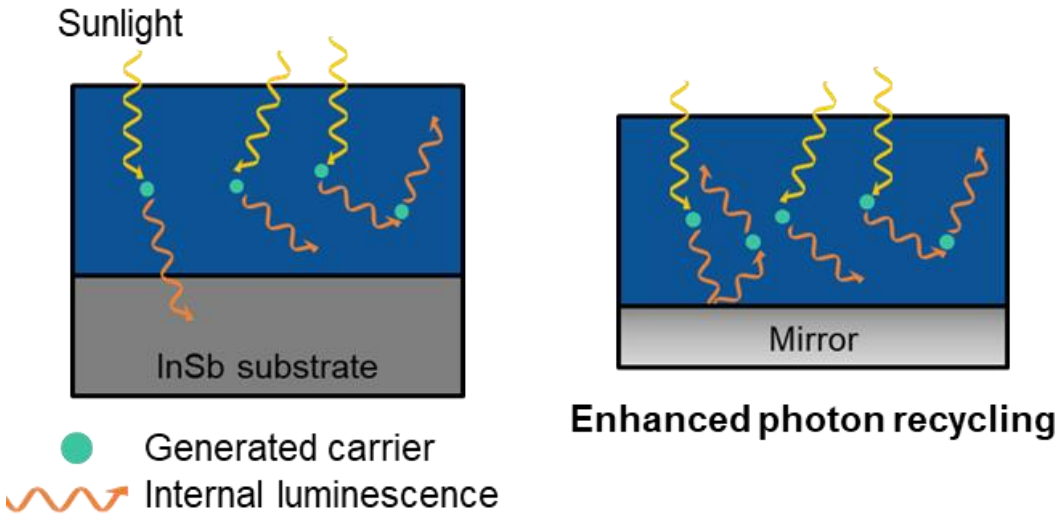

Fig. 5.1 A Schematic of The Enhanced Photon-recycling Effect Provided by a Reflective Mirror as Opposed to an Absorptive Low-bandgap Substrate.

Films freed from substrates can also be monolithically integrated into tandem devices. CdTe and MgCdTe alloys can also be integrated into high-efficiency and low cost tandem solar cells, notably the 1.7 eV/1.1 eV MgCdTe/Si tandem cells described in Section 1.4. The absence of a thick low-bandgap substrate is essential to allow longer-wavelength light to pass into a Si bottom cell in a monolithic, two-terminal design. In its place can be added a tunnel junction and a bonding medium.[70] ELO and wafer bonding has contributed to the development of multi-junction GaInP/GaAs//GaInAsP/GaInAs solar cells with the highest recorded efficiency of any photovoltaic device to date, 46%.[71]

Another benefit to II-VI ELO is that a free-standing thin film can be transferred onto lighter and/or more flexible substrates. This can open single-crystal CdTe solar cells to use in applications which require high efficiency coupled with minimal payload and/or flexible topography such as satellites. Currently, NASA is in the process of testing world-record GaAs thin film solar cells for use in space applications,[72] however the radiation resistance of CdTe-based solar cells[73] primes them to be an even better candidate for space than GaAs-based solar cells.

There are practical limitations to II-VI based ELO. Compound semiconductor III-V substrate materials including InSb and GaAs are chemically more stable than their II-VI counterparts. This makes the selective etching of the InSb substrate virtually impossible without damaging the II-VI films above and limits the use of even relatively weak etchants. Thankfully, MgTe is dissolvable in one of the most neutral etchants available: water.

5.1 State-of-the-Art Epitaxial Lift-Off (ELO) Technologies and Motivation for CdTe-based ELO

5.1.1 Aluminum Arsenide (AlAs) Epitaxial Lift Off

The practice of ELO (first coined Peeled Film Technology) was first applied to GaAs-based solar cells by the selective etching away of a sacrificial $Ga_{0.3}Al_{0.7}As$ layer[66]. Since AlAs is closely (99.9%) lattice-matched to gallium arsenide (GaAs), $Al_xGa_{1-x}As$ (x = 0 to 1) can be grown coherently on top of GaAs substrates.

Compared to GaAs, AlAs has an etch selectivity in 10% hydrogen fluoride (HF) solution of $\sim 10^5$. The AlAs-based ELO process begins with the application of a

supporting superstrate to the surface of an epitaxially-grown film. The sample is then immersed in HF solution where the reaction below commences as follows:[74]

$$AlAs + 3HF \rightarrow AlF_3 + AsH_3 \quad (5.1)$$

The percent of HF in the solution is very important because of the hydrogen gas (H_2) product because as the reaction progresses into the film interface radially, the diffusion of the gas bubbles out from the AlAs/HF interface must be as fast of the reaction rate at the interface which produces the bubbles. If the reaction proceeds to quickly for the bubbles to efficiently diffuse away, they end up collecting underneath the thin film and forming stress cracks as they float upward. For this reason, it is imperative that the concentration of HF in solution be as low as 10%. The ELO of a 4-in diameter circular wafer in 10% HF takes ~12 hours to complete, leaving behind an intact GaAs thin film absorber (attached to a superstrate) and a reusable GaAs substrate[67]. Interestingly, the presence of oxygen in sufficient quantities proves necessary, as without it elemental As can build up at the reaction interface, rather than be diffused away as Al_2O_3 under high enough P_{O_2} conditions.[74]

The superstrate must be chosen carefully, since for the thin film sample to become fabricated into a device structure, the superstrate needs to either be cleanly removed (without damaging the thin film sample in the process) or incorporated into the final device design. A widely-used sacrificial superstrate for AlAs-based ELO is Apiezon black wax, which is resistant to HF etching however can be dissolved away with tetracyanoethylene (TCE). The wax is heated for it to cure and harden. With the hardening of a circular drop of this black wax, the dimensions of the wax shrink and cause the wax to compress radially. This radial compressive strain acts on the thin film

below it, applying a lifting force as shown in Fig. 5.2. Such a lifting force has been shown to encourage the diffusion of hydrogen bubbles out from underneath the thin film, where if it remained it would collect and cause stress forces on the thin film above it.[75]

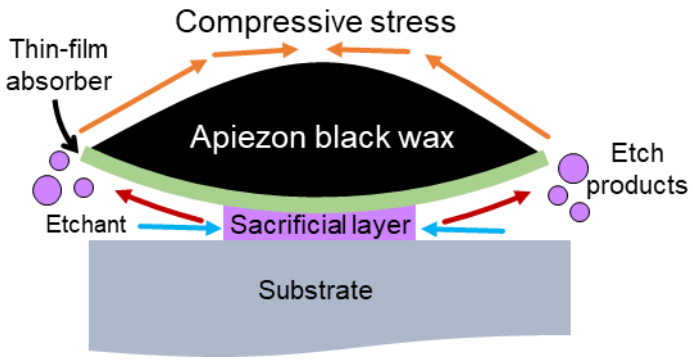

Fig. 5.2 Schematic of an Epitaxial Lift Off Process Using a Cured Superstrate to Lift The Edges of The Film, Enhancing The Diffusion of Etch Products Away from The Reaction Interface.[75]

The process of a strain being placed on the film is used not only for freeing hydrogen bubbles, but also to theoretically increase the etching rate of the sacrificial layer. This is commonly called weight-induced epitaxial lift-off (WI-ELO). To understand the effect of strain on the etching rate, first the basic parameters of AlAs ELO etching are defined. Studies have empirically shown that the rate of AlAs lateral etching (L_e) is the addition of two components, both constant:

$$L_e = V_{i,e} + V_{e,n} \tag{5.2}$$

the first being an intrinsic etch rate ($V_{i,e}$). is dependent upon several factors, including composition (of both the sacrificial layer and the adjacent epitaxial layers), the sacrificial layer thickness, and even dopant species present in the material system.

In $Al_xGa_{1-x}As$, $V_{i,n}$ increases linearly with increasing aluminum concentration from x = 0.7 to 1[76]. It is also important to consider the composition of the adjacent species, because it has been shown that an increase in misfit dislocations at both interfaces (for example if the films surrounding AlAs (a = 5.66 Å) are GaAs ((a = 5.65 Å) alloyed with too much InAs (a = 6.06 Å) and/or GaP (a = 5.45 Å)) causes not only more roughness of the resulting thin film, but also a slower $V_{i,n}$.[77]

The thickness of the sacrificial layer is also a factor. Studies show that the lateral etch rate increases linearly from an AlAs layer thickness reduction from 40 nm down to 3 nm. From a peak in lateral etch rate at 3 nm, the etch rate falls exponentially until it is non-existent at only a nanometer thinner of AlAs.[78] While theory states the thinner the sacrificial film the better,[75] in practice at thicknesses as low as 2 nm, even small-scale interface variability of a few monolayers can effectively reduce the AlAs layer down to zero, eliminating its ability to be etched away.[76]

Additionally, while the reason is inconclusive, doping in a materials system can sometimes affect the etch rate of the sacrificial AlAs layer. While n-type doping with Si does not show any effect on $V_{i,e}$, there is evidence of a linear relationship between an increasing p-type Zn concentration in the AlAs layer (or sandwiching layers due to diffusion) from ~10^{16} to 10^{18} cm^{-3} and an increase in $V_{i,e}$.[76]

The second term of the two-component lateral etch rate L_e is the faster "nominal" etch rate ($V_{e,n}$) which is dependent upon the radius of curvature of the materials system being acted upon. If there is no strain being acted upon the sample, $L_e = V_{i,e}$.

By using a flexible plate to change the radius of curvature of a sample during the ELO process, it is revealed that when the sacrificial layer is under tensile strain $V_{e,n}$ is larger.

Since AlAs has a larger lattice constant than GaAs, it is necessary to induce a curvature on the film in order to change the strain from compressive to tensile.[79] As such, the need for the induction of curvature in AlAs-based ELO is two-fold, both to free hydrogen bubbles produced as well as speed up the total etching away of the sacrificial layer.

5.1.2 Magnesium sulfide-based Epitaxial Lift-Off

Magnesium sulfide (MgS) is used in ELO of II-VI materials in the 5.6 Å material family grown on indium phosphide (InP), gallium phosphide (GaP) and GaAs substrates[80]. Notably, MgS is used as a sacrificial layer for lifting off ZnSe-based epitaxially-grown films, including ZnSe/ZnCdSe quantum wells[81],[82] and ZnMgSSe/ZnSe quantum wells[83].

MgS can be grown epitaxially by MBE using a Mg source and a ZnS source. During growth, the Mg displaces Zn in the lattice at the growing surface,[84],[82] achieving a metastable zinc blende MgS structure up to a thickness of 140 nm before reverting to a rock salt structure[85].

Apiezon black wax is used in a similar fashion to that of AlAs studies, being applied to the epi-grown film and cured by heating to 80 ℃[82]. The etch rate of MgS in 30% HCl solution is ~10^8 times that of ZnSe[81], and is up to 300 times higher than that of AlAs in 10% HF solution[86]. The reaction of MgS and HCl is theorized to proceed as follows[82]:

$$MgS + HCl \rightarrow Mg_{aq}^{2+} + H_2S \tag{5.3}$$

wherein H_2S is water-soluble. The wax superstrate is less dense than the solvent and floats to the top. After this, the epi-grown film is gently pressed onto a flat, smooth

surface where it is held in place by Van der Waals bonding[82]. Photoluminescence spectroscopy shows that the optical quality of the epi-films survives MgS-based ELO[81][87].

5.1.3 Magnesium Telluride (MgTe) Epitaxial Lift Off

CdTe and MgTe are binaries with a difference in lattice constant of only 1%, from which a Matthews-Blakeslee[18] critical thickness of 10 nm can be calculated. This epitaxially-compatible relationship allows for CdTe and MgTe and every composition of $Mg_xCd_{1-x}Te$ to be grown monolithically by MBE on lattice-matched InSb(001) substrates. This would allow for the monolithic growth of any CdTe and/or $Mg_xCd_{1-x}Te$-based absorber atop InSb substrates to incorporate a MgTe sacrificial layer. The highly-selective solubility rate of MgTe in water [88] means this material is primed to be the CdTe contemporary to AlAs in a GaAs-based solar cell.

5.2 MBE Growth of II-VI Films on InSb with MgTe Layer

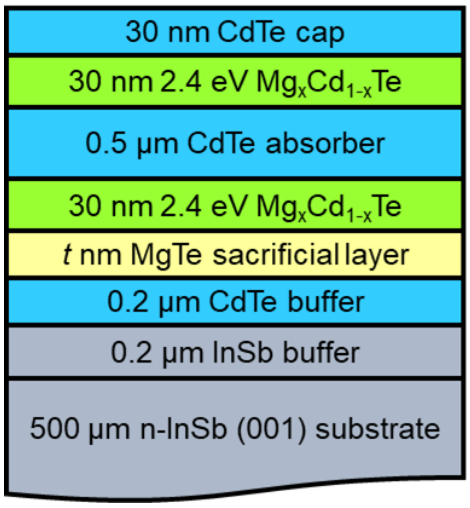

Fig. 5.3 Layer Structure for MBE-grown Double-heterostructure CdTe/Mg_xCd_{1-x}Te/MgTe on InSb(001).

Table 5.1 MBE Grown Samples Featuring Different MgTe Thicknesses and Compositions

Sample	Sacrificial layer Thickness	Cadmium alloyed into sacrificial layer
	t nm	%
A	10	trace
B	20	trace
C	130	trace
D	130	22

The samples used for the study feature a record-lifetime design for a CdTe/Mg_xCd_{1-x}Te DH absorber. These layers sit atop a sacrificial MgTe layer, grown monolithically on InSb(001) substrates. This layer structure detailed by the schematic shown above in Fig. 5.3. During MBE growth, streaky RHEED patterns indicate smooth layer growth throughout the MgTe film and the following II-VI layers above it. The growth rate, determined by RHEED oscillations, was calculated to be an estimated 0.761 Angstroms per second. Four samples are used, shown in Table 5.1. Three of the samples include 10 nm, 20 nm or 130 nm MgTe with trace amounts of CdTe. The fourth sample is 130 nm and features MgTe alloyed with 22% CdTe to form $Mg_{0.88}Cd_{0.22}$Te. Structural and optical characterization of both as-grown and free-standing samples is illustrated in the following sections. More sensitive electron measurement techniques should be used to very

accurately determine the MgTe thickness, however for comparison purposes the RHEED-estimated growth rate suffices for this study.

5.3 Optical Microscopy of As-grown Films

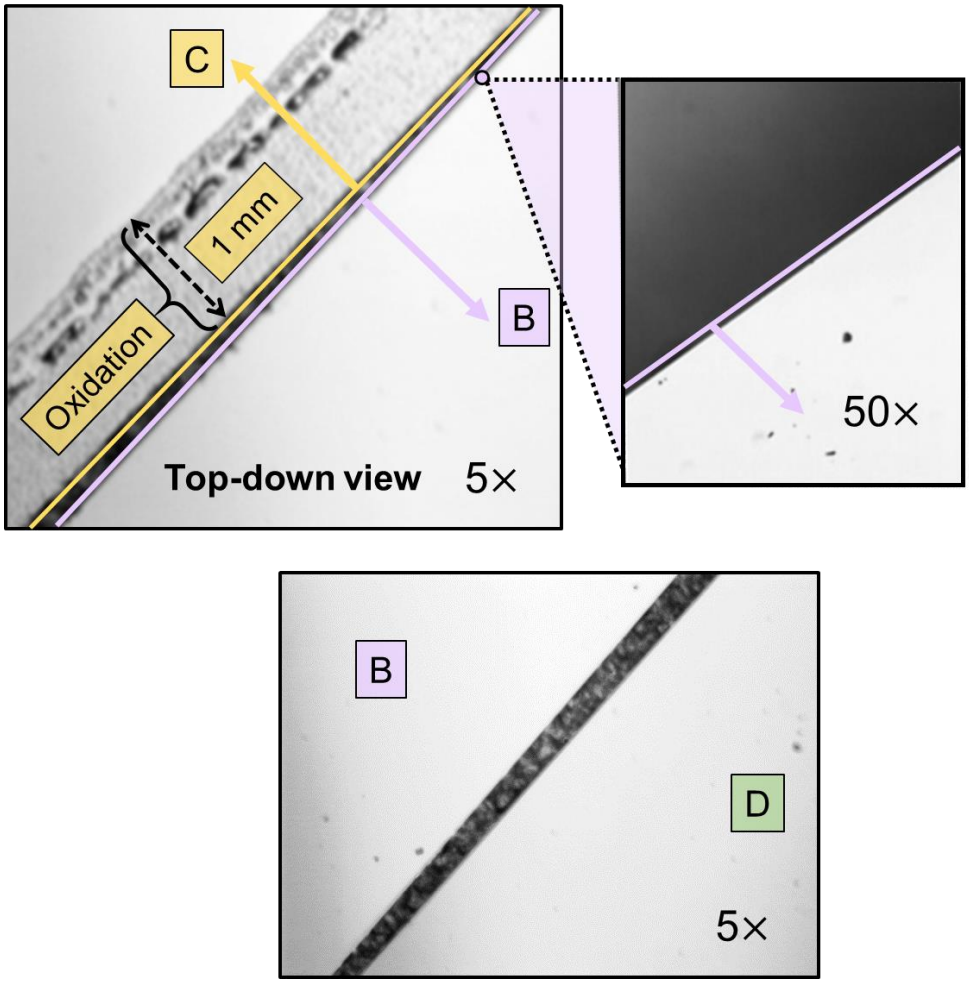

Fig. 5.4 Optical Microscopic Image Depicting a ~1 mm Oxidized MgTe Layer Near The Edge of Sample A and Smooth As-grown Surfaces of Samples C and D.

Once removed from ultra-high vacuum, samples are observed in atmosphere. Stability in atmosphere is important for the utility of the process, with higher stability allowing greater variability in processing options. A film which is robust to different atmospheric

conditions and temperatures allows, for example, for a degree of pre-processing to happen prior to the ELO process.

The MgTe films in sample B and C are of different thicknesses, 20 nm and 130 nm, respectively. The "sacrificial" layer in sample D is 130 nm and consists of 22% in the Group II lattice site. The top left corner of Fig. 5.4 shows a side-by-side, top-down microscopic image at a magnification of 5× of both sample B and C 30 minutes after removal from ultra-high vacuum. Sample B exhibits a smooth as-grown surface from the center to the very edge, even up to 50× magnification, shown by the top right image of Fig. 5.4.

Sample C, on the other hand, transitions from a smooth as-grown surface into developing about 1 mm of roughness on all four edges of a square piece of sample C mere minutes after being removed from vacuum. This is an indication that the exposed edges of this 130 nm thick MgTe layer have oxidized, in stark contrast to the ever-smooth surface of sample B. Additionally, sample D is also stable in atmosphere as evident by the smooth edges of the sample shown in the bottom image of Fig. 5.4. This shows that even relatively small amount of Cd in MgCdTe cause the alloy to be stable in atmosphere.

Samples B, C and D are heated to temperatures up to 250 ºC for 30 minutes. Sample C will quickly oxidize all the way through to the center of the sample when exposed to temperatures of 250℃. The edges of samples B and D remain unchanged. These results suggest that the oxidization processes in the Mg_xCd_yTe ($x >> y$) layers are thickness-dependent and composition-dependent.

5.4 High-resolution X-ray Diffraction of As-grown Films

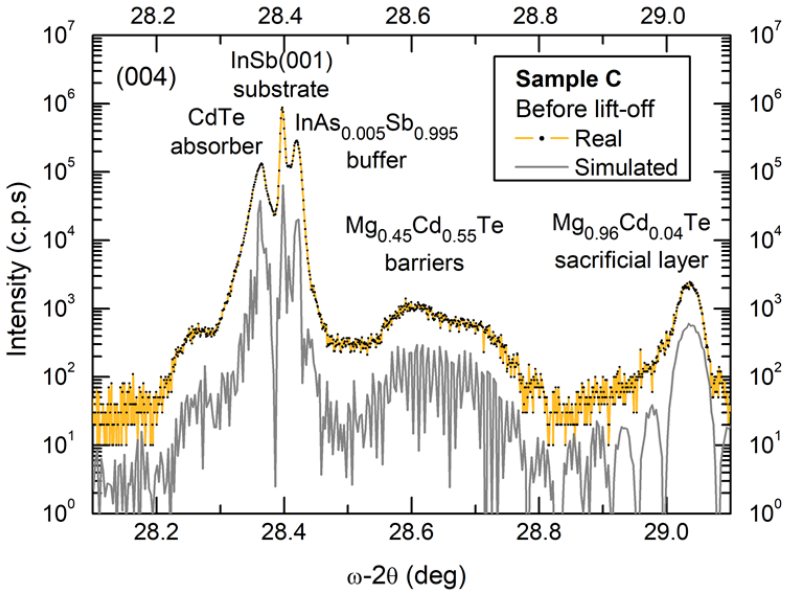

Layer	FWHM (arcseconds)
InSb	21
CdTe	57
MgTe	123

Fig. 5.5 X-ray Diffraction Along The (004) Peak of As-grown Sample A, Featuring a 130-nm MgTe Layer.

Fig. 5.5 depicts a (004) Omega-2θ X-ray diffraction scan of sample A immediately after removal from UHV and prior to ELO. The scan features are fit using X'pert Epitaxy Software. Evident in the scan are the typical peaks of a CdTe/$Mg_xCd_{1-x}Te$ double heterostructure on InSb(001), with the addition of a peak at ~29° corresponds to the single-crystal MgTe layer with a full width at half max of 123 arcseconds.

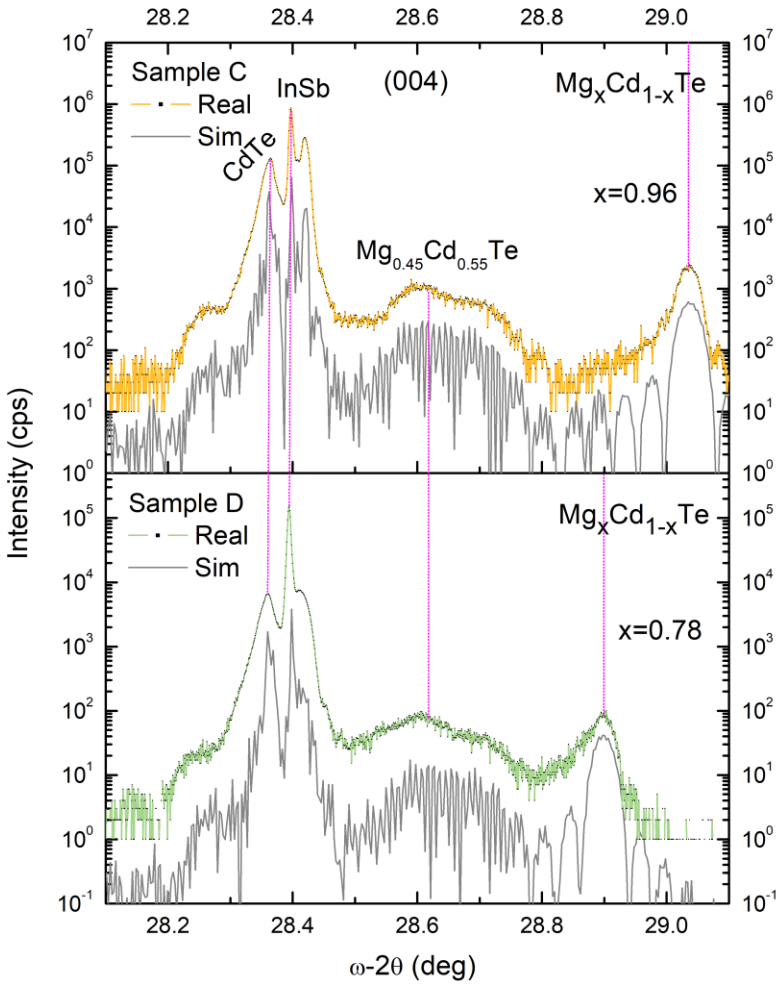

Fig. 5.6 X-ray Diffraction Along The (004) Peak of As-grown Sample A (top), Featuring a 130-nm MgTe Layer and Sample B (bottom) Featuring a 130-nm $Mg_{0.78}Cd_{0.22}Te$ Layer.

Comparing the (004) scans of samples C and D as shown in Fig. 5.6, one difference between them is apparent. The furthest right peak shifts 0.1° left between sample C and D. Curving fitting using X'pert Epitaxy depicts a shift in "sacrificial" layer composition from $Mg_{0.96}Cd_{0.04}Te$ to $Mg_{0.78}Cd_{0.22}Te$ between sample C to D. There is no

apparent difference in the order of magnitude of the FWHMs between peaks of samples C and D.

5.5 Steady-state Photoluminescence Spectroscopy of As-grown Films

Fig. 5.7 shows the room-temperature, 532 nm photoluminescence (PL) spectra of two as-grown samples B (20-nm MgTe) and C (130-nm MgTe). A GaAs/AlGaAs DH sample is used for reference. There is one peak exhibited by both samples, which corresponds to the bandgap of CdTe (820 nm wavelength). The intensity of the sample C peak is approximately twice as high as that of sample A.

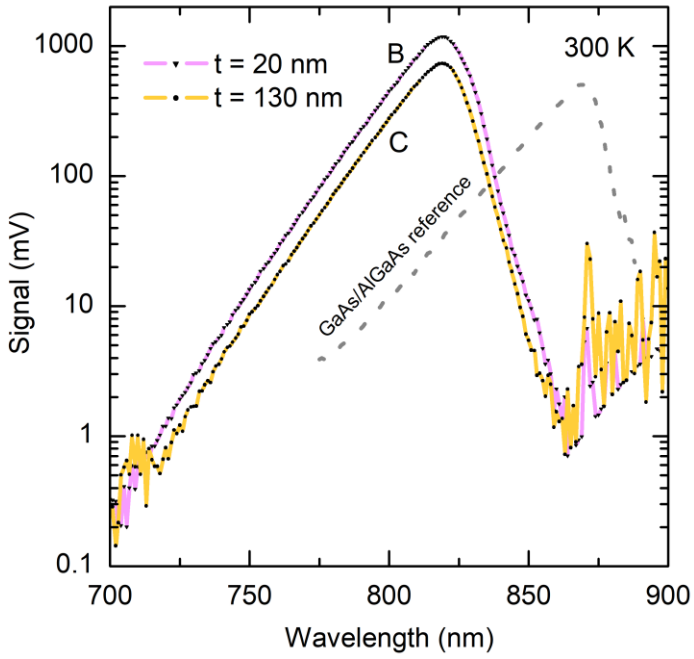

Fig. 5.7 Room-temperature Photoluminescence (PL) Showing a Trend of Higher PL Intensity with a Thinner MgTe Layer.

A likely culprit for the lowered PL intensity in sample C is the 130-nm thickness of the MgTe layer, since the Matthews-Blakeslee (M-B) critical thickness of MgTe on CdTe is ~10 nm[18]. Since the M-B critical thickness is calculated under equilibrium conditions and MBE in a non-equilibrium deposition process, 10 nm is a conservative estimate for this MBE-grown material system. That being said, 20 nm is a much closer value to the M-B critical thickness than 130 nm, and so misfit dislocations have likely formed at the MgTe/CdTe interface in the presence of thicker MgTe. These misfit dislocations propagate as threading dislocations through the layers grown atop the MgTe/CdTe interface and generate regions of increased defect-assisted non-radiative recombination. Additionally, as noted in section 5.3 above, sample C exhibits a higher degree of oxidation after exposure to atmosphere. This can introduce disorder to the layers above the oxidizing MgTe layer, and thus can contribute to a greater rate of nonradiative recombination as well.

5.6 Characterization of Free-standing CdTe/$Mg_xCd_{1-x}Te$ DH Films

5.6.1 Lift-off Process

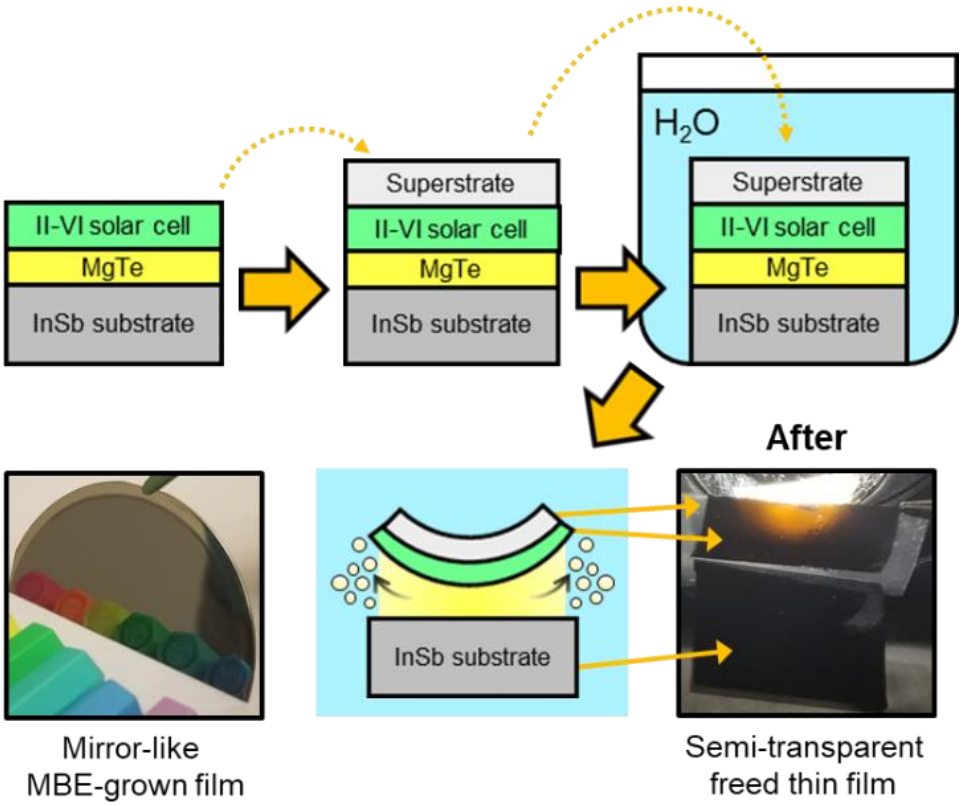

Fig. 5.8 Schematic of The II-VI MgTe-based Epitaxial Lift Off Process.

Fig. 5.8 depicts the basic process of epitaxial lift off. Upon removal from UHV after MBE growth, an adhesive is placed on the sample before it is immersed in water for a period of time. The reaction of MgTe in water likely features the reaction below:

$$MgTe + 2H_2O \longrightarrow Mg(OH)_{2(aq)} + H_2Te_{(g)} \quad (5.4)$$

where the reactants are MgTe and water and the products are magnesium hydroxide $Mg(OH)_2$ and hydrogen telluride H_2Te. H_2Te is highly volatile subsequently is likely to break down via the equation below:

$$H_2Te \longrightarrow H_2 + Te \tag{5.5}$$

where H_2Te separates into H_2 gas and Te particles. There is evidence of this chemical reaction seen during the ELO process.

During ELO, the pH of the water changes from 6 (typical of DI water) to 7. This change to a more basic pH is evidence of a hydroxide in the water after ELO, notably $Mg(OH)_2$. Additionally, black particles are present in the water after ELO, possibly Te particulates. Further spectrometry is needed to confirm the nature of the particles in the water post-ELO.

Table 5.2 Lift Off Results for Each Sample, with Considerations for Water Temperature and the Duration of Immersion

Sample	Water Temperature (ºC)	Completion of ELO Time in H_20	
		1 hour	2 hours
A	25	None	None
	75	None	None
B	25	Partial	Full
	75	Full	Full
C	25	Partial	Partial
	75	Partial	Partial
D	25	None	None
	75	None	None

As shown by Table 5.2, sample A (10 nm MgTe) did not lift off, even with a longer period of immersion and higher water temperature. The same is true for sample D, which is 130 nm thick and composed with 22% cadmium. The 130 nm MgTe (Sample C) is only partially lifted off, however shows roughness and pinholes when it is peeled away from the substrate. Sample B (20 nm MgTe) exhibited complete ELO and did not need to

be peeled away both at room temperature after 2 hours and 75 ℃ after only 1 hour. A comparison of films from Sample B and C is shown in Fig. 5.9 below.

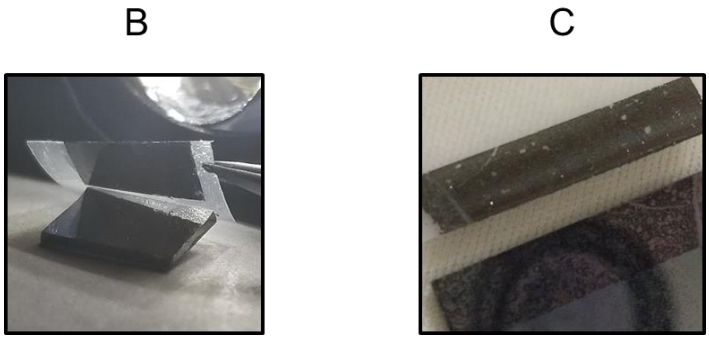

Fig. 5.9 A Comparison of Films from Sample B and D After Room-temperature ELO.

This behavior is similar to that seen in AlAs-based ELO[78]. Studies show a bell curve wherein the lateral etch rate of AlAs increases with the thinning of the release layer from 100 nm to 3 nm and slows down significantly once the layer becomes even one nanometer thinner. Since the ELO thickness cut-off for MgTe (10 nm) is higher than that of AlAs, this could be for several reasons, including the etching mechanism of H_2O acting on MgTe vs HF acting on AlAs. Also, the thickness of MgTe needs to be more accurately characterized by techniques such as scanning electron microscopy (SEM). The results of sample B suggest that the reduction in thickness necessary for mitigation of oxidation processes increases the efficiency of ELO. Additionally, studies show that there is an exponential increase in lateral etch rate with an increase in temperature, from 2.5 mm/hr at room temperature up to 11.2 mm/hr at 80 ℃.[78]

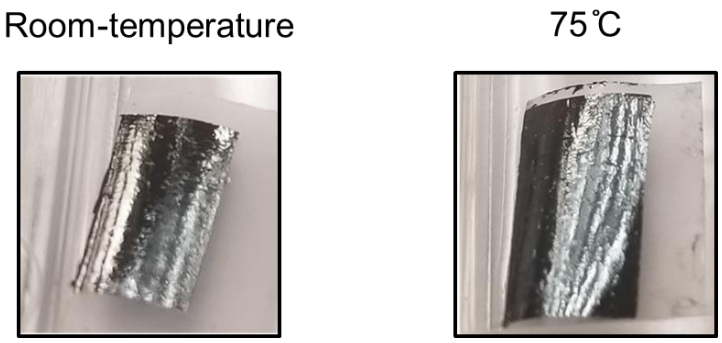

Fig. 5.10 A Comparison of Films from Sample B Immersed in Room-temperature vs. 75 ^{o}C Water for ELO.

It is important to note that the structural integrity of CdTe DH films on tape becomes degraded after immersion in 75 ^{o}C water. As shown by Fig. 5.10 (right), the resulting films show precipitates around the edges as well as a warped tape superstrate. Thus, it is likely that the slightly longer time for ELO in room-temperature water is worth it to maintain the integrity of the material system, at least when on a tape superstrate.

A ZeScope optical profilometer was used to measure the surface of the free-standing sample B on tape. Shown by Fig 5.11, sheets of thin film on the order of 1-mm across are seen across the tape superstrate. Note that the tilt of the height profile is due to the uneven tape surface. Dimensions below this are seen even from graphene on tape[89]. Thus, while achieving these dimensions of smoothness are no small feat, it is clear that to get film smoothness on the scale of even a relatively small 2- to 3-mm^2 device, other smoother, harder superstrates should be used.

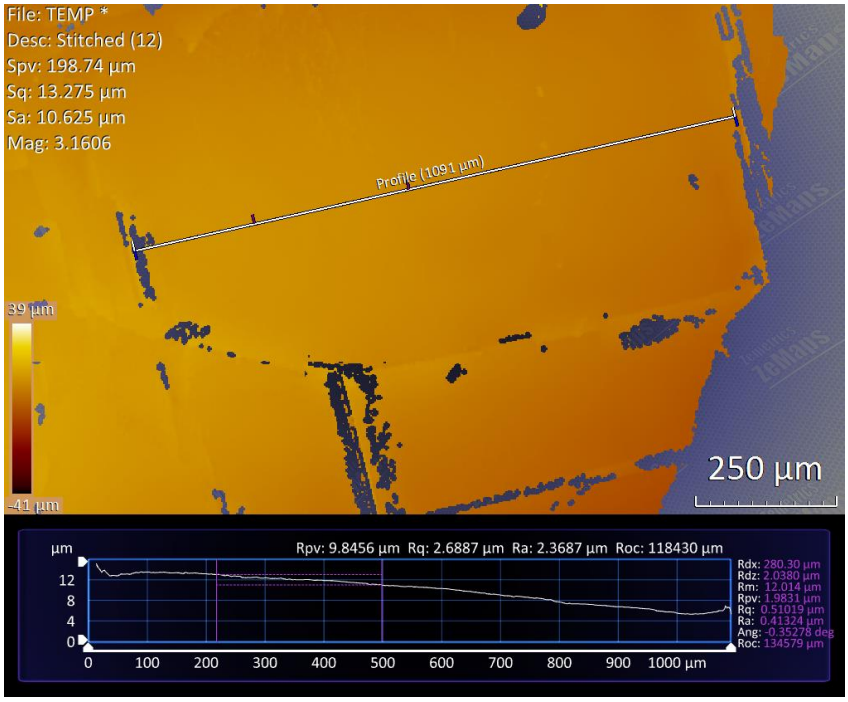

Fig. 5.11 – An Optical Profilometer Image of a Thin-film Piece of Sample B on Tape.

5.6.2 High-resolution X-ray Diffraction Comparing the As-grown and Free-standing Films

The first step in assessing the quality of lifted-off, free-standing films is high-resolution X-ray diffraction. Building from the data described in Section 5.4, Fig. 5.12 compares the (004) X-ray diffraction spectra between as-grown and freestanding films of sample C, using a high-resolution X-ray diffraction system as described in Section 2.5. The spectra of the free-standing film is devoid of both the MgTe and InSb peaks. However, the CdTe and $Mg_xCd_{1-x}Te$ barrier features are still intact.

From the differences between these two sample scans, it is evident that the substrate and MgTe layers have disappeared, leaving a CdTe/MgCdTe double heterostructure behind. The broadening of the CdTe peak from the as-grown sample to the free-standing

sample may be a result of the thinning of the layer after the removal of the CdTe buffer layer. Additionally, peak broadening may be introduced bending in the flexible film during mounting and the XRD measurement process.

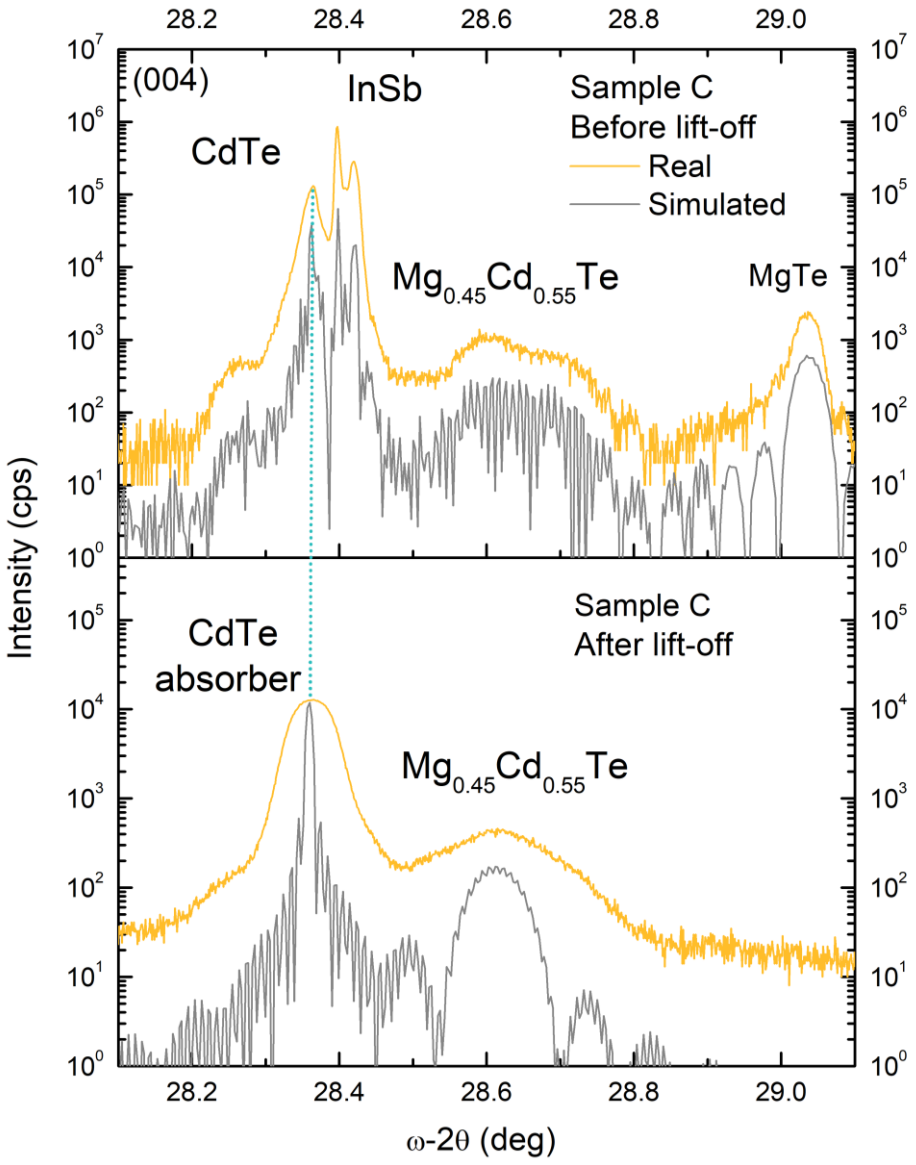

Fig. 5.12 Omega-2θ (004) Scan of As-grown Sample B (top) on InSb Substrate and The Scan of The CdTe/$Mg_xCd_{1-x}Te$ Double-heterostructure Thin Film After The Lift-off (bottom).

5.6.3 Steady-state Photoluminescence Spectroscopy

Fig. 5.13 depicts the room-temperature, 532 nm PL spectra of sample B, both the as-grown sample and the CdTe/$Mg_xCd_{1-x}Te$ double-heterostructure thin-film after release from the InSb substrate. The PL of the free-standing film is much stronger (on the order of 400%) than that of the as-grown sample as well as a high-quality GaAs/AlGaAs DH reference sample. The dramatic increase in PL is regulated predominantly to the edges of the sample. For this reason, it is likely that luminescence concentration[90] is at least partially responsible for the increase in PL. While this phenomenon can paint an unrealistically inflated picture of the optical quality of the bulk film, it is to be expected in thin layers which feature a reflective back mirror and a high degree of photon recycling. Thus, it is clear from the PL that the optical and structural integrity of the CdTe/MgCdTe DH remains intact after ELO.

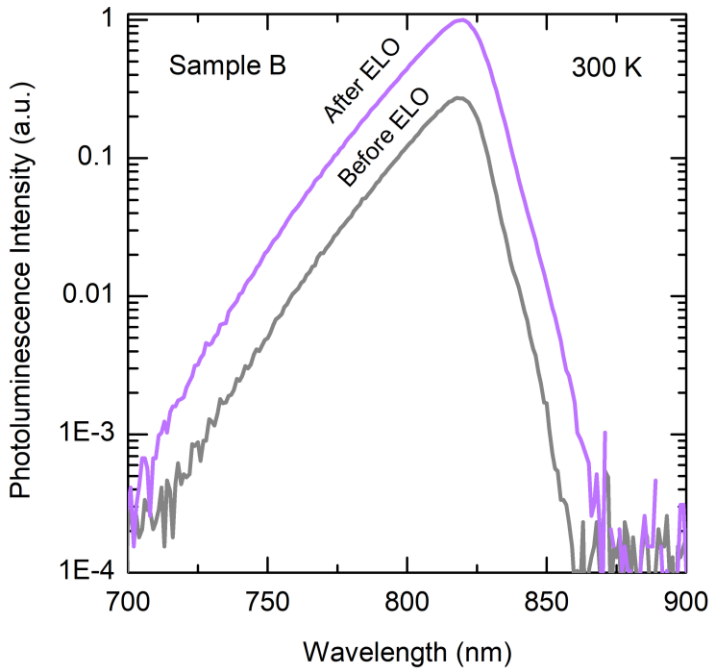

Fig. 5.13 Comparison of The PL Spectra Between Intact and Free-standing CdTe/$Mg_xCd_{1-x}Te$ DH Absorbers.

Chapter Summary

This chapter has presented an epitaxial-lift-off technology using water-soluble MgTe for free-standing single-crystal CdTe/$Mg_xCd_{1-x}Te$ DHs grown on lattice-matched InSb(001) substrates. This low-cost technology can be used to lift off CdTe and 1.7-eV $Mg_xCd_{1-x}Te$ solar cells in order to enhance light management and freedom in device processes. CdTe/$Mg_xCd_{1-x}Te$ DHs with MgTe sacrificial layers of several thicknesses were grown by MBE. MgTe thickness proves to significantly affect crystal morphology, stability in atmosphere, and completion of ELO.

CHAPTER SIX - CONCLUSIONS AND FUTURE WORK

The long-term vision for this work is to further the progress toward a II-VI 1.7-eV thin-film solar cell which offers a practical pathway to further cost-reduction of solar power generation single-junction and multijunction PV applications. This dissertation details the path taken to produce MBE-grown single-crystal II-VI material that probes the fundamental limits of wide-bandgap $Mg_xCd_{1-x}Te$ semiconductor quality and PV device performance. A first step was the growth of monocrystalline 1.7 eV $Mg_xCd_{1-x}Te/Mg_yCd_{1-y}Te$ (y>x) double heterostructures (DHs), whose dimensions were optimized in order to maximize structural and optical material quality, culminating in a design with a record carrier lifetime of 560 ns. Drawing on previous CdTe DH solar cell studies, several 1.7 eV $Mg_xCd_{1-x}Te/Mg_yCd_{1-y}Te$ (y>x) DH solar cells were grown and fabricated with an a-Si hole contact. By iterating both the MBE-grown DH absorber design and the subsequent contact and anti-reflection layers, the V_{OC}, J_{SC} and FF were optimized to produce a single-junction device with a record active-area efficiency of 15.2% and a record open-circuit voltage of 1.176 V. Future enhancements in the device performance of these cells will require the fabrication of cells with asymmetrical barriers and more transparent hole contacts than that of those made with a-Si. The motivation for barriers with asymmetrical composition is such that at each of the two interfaces of the absorber, different dimensions of barrier are optimal, as seen from mono-CdTe SC studies. A thinner, wider-bandgap top barrier can lead to less parasitic absorption and thus a higher J_{SC} while reduced dimensions in the bottom barrier can maximize transport and FF. The motivation

for wider-bandgap hole contacts is their ability to improve J_{SC} by mitigating parasitic absorption seen in a-Si.

With the intent of maximizing the V_{OC} of this 1.7-eV material, a study of the n-type doping behavior of indium in 1.7-eV $Mg_xCd_{1-x}Te$ was performed which included the production of several *in-situ* doped MBE-grown samples. From varying the II/VI flux ratio between several samples, it could be determined that this Group II overpressure during growth had a huge impact on carrier activation. Measured using Hg probe and electrochemical C-V measurement, the carrier concentration in a 1.7 eV absorber jumped orders of magnitude with only slight variations in flux ratio. Ultimately a 1.7 eV $Mg_xCd_{1-x}Te$ absorber with a fully-activated carrier concentration of 1×10^{17} cm^{-3} was measured using SIMS, Hg probe C-V, electrochemical C-V, and PLQE, and was determined to have an i-V_{OC} of 40 mA higher than that of an equivalent undoped design. A logical next step for these samples is their being processed into solar cells, transferring an increase in i-V_{OC} to an increase in efficiency for a power-generating device. Future work in this area should also include studies which probe into the nature of the defect species using characterization techniques like Deep Level Transient Spectroscopy to better understand the effects of growth conditions on the behavior of *in-situ* doped $Mg_xCd_{1-x}Te$:In.

Finally, this paper details the study of II-VI epitaxial lift off (ELO) using water-soluble MgTe for free-standing single-crystal CdTe-based absorbers. The application of this technology makes possible a drastic increase in cell conversion efficiency through improved light management, along with allowing for freedom in device design, enabling CdTe-based solar cells to be integrated into high-efficiency thin, flexible, lightweight and multijunction devices. Samples with different thicknesses of MgTe or Mg_xCd_yTe ($x>>y$)

were grown by MBE sandwiched between a hero-lifetime CdTe DH and an InSb substrate. Through structural and optical characterization, it was determined that a thinner MgTe film provided higher PL intensity and was resistant to oxidation like that of a thicker $Mg_{0.78}Cd_{0.22}Te$ film. ELO in room-temperature water revealed that 20-nm thick MgTe provided the fastest, smoothest lift-off, while the ELO of thicker films was patchy and the ELO of thinner MgTe as well as 130-nm $Mg_{0.78}Cd_{0.22}Te$ was non-existent. Both X-ray diffraction and photoluminescence spectroscopy reveal the structural and optical quality of the thin films survive ELO.

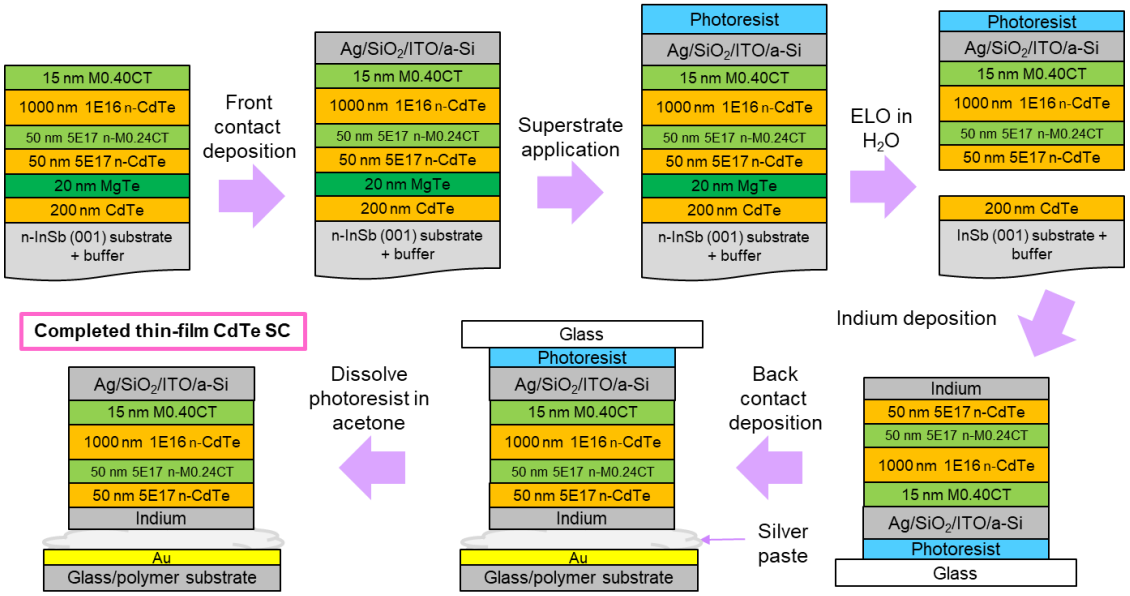

Fig. 6.1 Schematic of The II-VI MgTe-based Epitaxial Lift Off Process Integrated with Device Fabrication.

In order to better understand the nature of the MgTe dissolution must, mass spectrometry can be used for the determination of product species in the reaction, and structural characterization including atomic force microscopy can characterize the surface

morphology of the free-standing films and the substrate after the ELO process for various dimensions.

Future work will evolve into the fabrication of devices from free-standing CdTe and/or $Mg_xCd_{1-x}Te$ double heterostructure absorbers. While pressure-sensitive tape serves as an excellent medium with which to explore material parameters, it is non-ideal for fabrication of these free-standing films into PV devices. Such a goal requires in depth study of alternative superstrates, such as sacrificial black wax or photoresist, or conductive films which can be integrated into the final device. Partially processing the MBE-grown films into devices may be beneficial to the ELO process. An example of this shown in Fig 6.1 above, wherein top contacts are deposited onto the epi-grown sample to increase its overall structural integrity prior to undergoing ELO and additional processing. The stability of 20-nm MgTe in atmosphere and at elevated temperatures will help to make this freedom of processing order possible. The smooth, quick ELO of a large-area, transferrable CdTe-based thin film will be a disruptive evolution in the CdTe community.

REFERENCES

[1] "Inventory of U.S. Greenhouse Gas Emissions and Sinks." [Online]. Available: https://www.epa.gov/ghgemissions/inventory-us-greenhouse-gas-emissions-and-sinks.

[2] "Advantages and Challenges of Wind Energy | Department of Energy." [Online]. Available: https://www.energy.gov/eere/wind/advantages-and-challenges-wind-energy.

[3] R. Pichs Madruga *et al.*, "Renewable Energy Sources and Climate Change Mitigation Special Report of the Intergovernmental Panel on Climate Change Edited by Ottmar Edenhofer Youba Sokona," 2012.

[4] "Bioenergy | Department of Energy." [Online]. Available: https://www.energy.gov/science-innovation/energy-sources/renewable-energy/bioenergy.

[5] "The History of Solar," 2012. [Online]. Available: https://www1.eere.energy.gov/solar/pdfs/solar_timeline.pdf.

[6] "History of Solar Power - IER." [Online]. Available: https://instituteforenergyresearch.org/analysis/history-of-solar-power/.

[7] Peter Diamandis, "Solar Energy Revolution: A Massive Opportunity." [Online]. Available: https://www.forbes.com/sites/peterdiamandis/2014/09/02/solar-energy-revolution-a-massive-opportunity/#3619299a6c90.

[8] M. Woodhouse *et al.*, "Perspectives on the pathways for cadmium telluride photovoltaic module manufacturers to address expected increases in the price for tellurium," *Sol. Energy Mater. Sol. Cells*, vol. 115, pp. 199–212, Aug. 2013.

[9] "Reference Air Mass 1.5 Spectra | Grid Modernization | NREL." [Online]. Available: https://www.nrel.gov/grid/solar-resource/spectra-am1.5.html.

[10] T. Tiedje, E. Yablonovitch, G. D. Cody, and B. G. Brooks, "Limiting efficiency of silicon solar cells," *IEEE Trans. Electron Devices*, vol. 31, no. 5, pp. 711–716, 1984.

[11] S. M. Sze and K. K. Ng, *Physics of Semiconductor Devices*. Wiley-Interscience, 2007.

[12] S. P. Bremner, M. Y. Levy, and C. B. Honsberg, "Analysis of tandem solar cell efficiencies under AM1.5G spectrum using a rapid flux calculation method," *Prog. Photovoltaics Res. Appl.*, vol. 16, no. 3, pp. 225–233, 2008.

[13] D. Ding, S. R. Johnson, S.-Q. Yu, S.-N. Wu, and Y.-H. Zhang, "A semi-analytical model for semiconductor solar cells," *J. Appl. Phys.*, vol. 110, no. 12, p. 123104, 2011.

[14] M. A. Green *et al.*, "Solar cell efficiency tables (Version 53)," *Prog. Photovoltaics*

Res. Appl., vol. 27, no. 1, pp. 3–12, 2019.

[15] C. M. Campbell *et al.*, "1.7 eV MgCdTe double-heterostructure solar cells for tandem device applications," in *2017 IEEE 44th Photovoltaic Specialist Conference*, 2018, p. 9781509056057.

[16] M. J. DiNezza, X. H. Zhao, S. Liu, A. P. Kirk, and Y. H. Zhang, "Growth, steady-state, and time-resolved photoluminescence study of CdTe/MgCdTe double heterostructures on InSb substrates using molecular beam epitaxy," *Appl. Phys. Lett.*, vol. 103, p. 193901, 2013.

[17] M. Henini, *Molecular beam epitaxy : from research to mass production*. Elsevier, 2013.

[18] J. W. Matthews and A. E. Blakeslee, "Defects in epitaxial multilayers: I. Misfit dislocations," *J. Cryst. Growth*, vol. 27, pp. 118–125, 1974.

[19] A. Braun, K. M. Briggs, and P. Böni, "Analytical solution to Matthews' and Blakeslee's critical dislocation formation thickness of epitaxially grown thin films," *J. Cryst. Growth*, vol. 241, no. 1–2, pp. 231–234, May 2002.

[20] W. D. Callister, *Fundamentals of Materials Science and Engineering: an integrated approach.* John Wiley, 2015.

[21] S. Adachi, *Handbook on Physical Properties of Semiconductors*. Dordrecht: Kluwer Academic Publishers, 2004.

[22] W. Braun, *Applied RHEED*, vol. 154. Berlin, Heidelberg: Springer Berlin Heidelberg, 1999.

[23] T. Litz, T. Behr, D. Hommel, A. Waag, and G. Landwehr, "Growth mechanisms of CdTe during molecular beam epitaxy," *J. Appl. Phys.*, vol. 72, no. 8, pp. 3492–3496, Oct. 1992.

[24] J. M. Hartmann *et al.*, "CdTe/MgTe heterostructures: Growth by atomic layer epitaxy and determination of MgTe parameters," *J. Appl. Phys.*, vol. 80, no. 11, pp. 6257–6265, 1996.

[25] W. L. Bragg, "The diffraction of short electromagnetic waves by a crystal," *Proc. Camb. Philol. Soc.*, 1913.

[26] M. Wormington, "High-Resolution X-ray Diffraction of Epitaxial Thin-Films and Patterned Nanostructures," *Front. Charact. Metrol. Nanoelectron.*, 2015.

[27] K. J. Mackey, D. R. T. Zahn, P. M. G. Allen, R. H. Williams, W. Richter, and R. S. Williams, "InSb–CdTe interfaces: A combined study by soft x-ray photoemission, low-energy electron diffraction, and Raman spectroscopy," *J. Vac. Sci. Technol. B Microelectron. Nanom. Struct.*, vol. 5, no. 4, p. 1233, Jul. 1987.

[28] R. E. Honig and D. A. Kramer, "Vapor Pressure for the Solid and Liquid Elements," *RCA Rev.*, vol. 30, no. 2, pp. 285–305, 1969.

[29] K. J. Mackey, P. M. G. Allen, W. G. Herrenden-Harker, R. H. Williams, C. R. Whitehouse, and G. M. Williams, "Chemical and electronic structure of InSb-CdTe interfaces," *Appl. Phys. Lett.*, vol. 49, no. 6, pp. 354–356, 1986.

[30] M. J. DiNezza, “Monocrystalline ZnTe/CdTe/MgCdTe Double Heterostructure Solar Cells Grown on InSb Substrates by Molecular Beam Epitaxy,” Arizona State University https://repository.asu.edu/items/26867, 2014.

[31] X. Wang, C. Campbell, Y.-H. Zhang, and R. J. Nemanich, “Band alignment at the CdTe/InSb (001) heterointerface,” *J. Vac. Sci. Technol. A Vacuum, Surfaces, Film.*, vol. 36, no. 3, p. 031101, 2018.

[32] J. M. Hollander and W. L. Jolly, “X-Ray Photoelectron Spectroscopy,” *Acc. Chem. Res.*, vol. 3, no. 6, pp. 193–200, 1970.

[33] “What is Ellipsometry? - J.A. Woollam,” 2018. [Online]. Available: https://www.jawoollam.com/resources/ellipsometry-tutorial/what-is-ellipsometry.

[34] X.-H. Zhao, S. Liu, C. M. Campbell, Y. Zhao, M. B. Lassise, and Y.-H. Zhang, “Ultralow interface recombination velocity (∼1 cm/s) in CdTe/MgxCd1-xTe double-heterostructures,” *IEEE J. Photovoltaics*, vol. 7, no. 3, pp. 913–918, 2017.

[35] S. Liu, X.-H. Zhao, C. M. Campbell, M. B. Lassise, Y. Zhao, and Y.-H. Zhang, “Significantly improved carrier lifetime and reduced interface recombination velocity for CdTe/MgCdTe double heterostructures,” in *2015 IEEE 42nd Photovoltaic Specialist Conference*, 2015, p. 15664817.

[36] X.-H. Zhao, M. J. Dinezza, S. Liu, C. M. Campbell, Y. Zhao, and Y.-H. Zhang, “Determination of CdTe bulk carrier lifetime and interface recombination velocity of CdTe/MgCdTe double heterostructures grown by molecular beam epitaxy,” *Appl. Phys. Lett.*, vol. 105, no. 25, 2014.

[37] S. Liu, X.-H. Zhao, C. M. Campbell, M. B. Lassise, Y. Zhao, and Y.-H. Zhang, “Carrier lifetimes and interface recombination velocities in CdTe/MgxCd1-xTe double heterostructures with different Mg compositions grown by molecular beam epitaxy,” *Appl. Phys. Lett.*, vol. 107, no. 4, 2015.

[38] B. Kuhn-Heinrich *et al.*, “Optical investigation of confinement and strain effects in CdTe/(CdMg)Te quantum wells,” *Appl. Phys. Lett.*, vol. 63, no. 21, pp. 2932–2934, Nov. 1993.

[39] O. D. Miller, E. Yablonovitch, and S. R. Kurtz, “Strong internal and external luminescence as solar cells approach the Shockley-Queisser limit,” *IEEE J. Photovoltaics*, vol. 2, no. 3, pp. 303–311, 2012.

[40] Y. Zhao, X.-H. Zhao, and Y.-H. Zhang, “Radiative Recombination Dominated Monocrystalline CdTe/MgCdTe Double-Heterostructures,” *IEEE J. Photovoltaics*, vol. 7, no. 2, pp. 690–694, 2017.

[41] P. S. Eric Toberer, A. C. Tamboli, M. Steiner, S. Kurtz, and E. S. Toberer, “Analysis of Solar Cell Quality Using Voltage Metrics: Preprint,” 2012.

[42] Y. Zhao *et al.*, “Monocrystalline CdTe solar cells with open-circuit voltage over 1 V and efficiency of 17%,” *Nat. Energy*, vol. 1, no. 6, p. 16067, 2016.

[43] J. J. Becker *et al.*, “Monocrystalline 1.7-eV-Bandgap MgCdTe Solar Cell With 11.2% Efficiency,” *IEEE J. Photovoltaics*, vol. 8, no. 2, pp. 581–586, Mar. 2018.

[44] J. J. Becker *et al.*, “Loss Analysis of Monocrystalline CdTe Solar Cells with 20% Active-Area Efficiency,” *IEEE J. Photovoltaics*, vol. 7, no. 3, 2017.

[45] J. J. Becker *et al.*, “Monocrystalline CdTe/MgCdTe Double-Heterostructure Solar Cells With ZnTe Hole Contacts,” *IEEE J. Photovoltaics*, vol. 7, no. 1, pp. 307–312, Jan. 2017.

[46] Z.-Y. He *et al.*, “CdTe nBn photodetectors with ZnTe barrier layer grown on InSb substrates,” *Appl. Phys. Lett.*, vol. 109, no. 12, 2016.

[47] D. K. Chakrabarty, *An introduction to physical chemistry*. Alpha Science International Ltd, 2001.

[48] S.-H. Wei and S. B. Zhang, “Chemical trends of defect formation and doping limit in II-VI semiconductors: The case of CdTe,” *Phys. Rev. B*, vol. 66, no. 15, p. 155211, 2002.

[49] S. B. Zhang and S.-H. Wei, “Nitrogen Solubility and Induced Defect Complexes in Epitaxial GaAs:N,” *Phys. Rev. Lett.*, vol. 86, no. 9, pp. 1789–1792, 2001.

[50] J. Ma, J. Yang, S.-H. Wei, and J. L. F. Da Silva, “Correlation between the electronic structures and diffusion paths of interstitial defects in semiconductors: The case of CdTe,” *Phys. Rev. B*, vol. 90, no. 15, p. 155208, 2014.

[51] M. Emziane, K. Durose, D. P. Halliday, N. Romeo, and A. Bosio, “SIMS depth profiling of CdTe-based solar cells grown on sapphire substrates,” *Thin Solid Films*, vol. 511–512, pp. 66–70, 2006.

[52] E. Hoonnivathana, E. D. Jones, I. V. F. Viney, and L. J. Duckers, “Diffusion of phosphorus in CdTe,” *J. Electron. Mater.*, vol. 27, no. 6, pp. 610–614, 1998.

[53] S. Farrell, T. Barnes, W. K. Metzger, J. H. Park, R. Kodama, and S. Sivananthan, “In Situ Arsenic Doping of CdTe/Si by Molecular Beam Epitaxy,” *J. Electron. Mater.*, vol. 44, no. 9, pp. 3202–3206, 2015.

[54] J. H. Park *et al.*, “Incorporation and Activation of Arsenic Dopant in Single-Crystal CdTe Grown on Si by Molecular Beam Epitaxy,” *J. Electron. Mater.*, vol. 43, no. 8, pp. 2998–3003, 2014.

[55] E. Colegrove, B. Stafford, Wei Gao, T. Gessert, and S. Sivananthan, “Arsenic doped heteroepitaxial CdTe by MBE for applications in thin-film photovoltaics,” in *2014 IEEE 40th Photovoltaic Specialist Conference (PVSC)*, 2014, pp. 3261–3265.

[56] E. V. Rabenok, M. V. Galanovich, G. F. Novikov, and I. N. Odin, “Effect of self-compensation on the electron lifetime in gallium-doped cadmium telluride,” *Semiconductors*, vol. 43, no. 7, pp. 846–851, 2009.

[57] E. Placzek-Popko, Z. Gumienny, J. Szatkowski, E. Płaczek-Popko, and J. Trzmiel, “Evidence for metastable behavior of Ga-doped CdTe,” *Opt. Appl.*, vol. 38, no. 3, 2008.

[58] S. H. Song, J. Wang, Y. Ishikawa, S. Seto, and M. Isshiki, “Photoluminescence study on compensating defects in CdTe:Al,” *J. Cryst. Growth*, vol. 237–239, pp.

1726–1730, 2002.

[59] A. J. Moll, K. M. Yu, W. Walukiewicz, W. L. Hansen, and E. E. Haller, “Coimplantation and electrical activity of C in GaAs: Stoichiometry and damage effects,” *Appl. Phys. Lett.*, vol. 60, no. 19, pp. 2383–2385, 1992.

[60] A. Benninghoven, F. G. Rüdenauer, and H. W. Werner, *Secondary ion mass spectrometry : basic concepts, instrumental aspects, applications, and trends*. J. Wiley, 1987.

[61] F. Bassani *et al.*, “Indium doping of CdTe and Cd1-xZnxTe by molecular-beam epitaxy: Uniformly and planar-doped layers, quantum wells, and superlattices,” *Cit. J. Appl. Phys.*, vol. 72, p. 2927, 1992.

[62] H. Kato and S. Takayanagi, “Diffusion of Indium in Cadmium Telluride,” *Japan J. Appl. Phys.*, vol. 2, pp. 250–251, 1963.

[63] “ECV Profiling.” [Online]. Available: https://www.probion.fr/en/tutorials/ecvp/ecvprofiling.html. [Accessed: 29-Jul-2018].

[64] X.-H. Zhao *et al.*, “Optical properties of indium-doped CdTe/MgCdTe double heterostructures,” in *2015 IEEE 42nd Photovoltaic Specialist Conference, PVSC 2015*, 2015.

[65] X.-H. Zhao *et al.*, “Electrical and Optical Properties of n-Type Indium-Doped CdTe/Mg0.46Cd0.54Te Double Heterostructures,” *IEEE J. Photovoltaics*, vol. 6, no. 2, 2016.

[66] M. Konagai, M. Sugimoto, and K. Takahashi, “High efficiency GaAs thin film solar cells by peeled film technology,” *J. Cryst. Growth*, vol. 45, pp. 277–280, 1978.

[67] C. Youtsey *et al.*, “Epitaxial Lift-Off of Large-Area GaAs Thin-Film Multi-Junction Solar Cells,” in *CS MANTECH Conference*, 2012.

[68] J. J. Schemer, P. Mulder, G. J. Bauhuis, P. K. Larsen, G. Oomen, and E. Bongers, “Thin-film GaAs epitaxial lift-off solar cells for space applications,” *Prog. Photovoltaics Res. Appl.*, vol. 13, no. 7, pp. 587–596, 2005.

[69] M. Y. Feteha and G. M. Eldallal, “The effects of temperature and light concentration on the GaInP/GaAs multijunction solar cell’s performance,” *Renew. Energy*, vol. 28, pp. 1097–1104, 2003.

[70] E. Yablonovitch *et al.*, “Van der Waals bonding of GaAs on Pd leads to a permanent, solid-phase-topotaxial, metallurgical bond,” *Appl. Phys. Lett.*, vol. 59, no. 24, pp. 3159–3161, Dec. 1991.

[71] F. Dimroth *et al.*, “Four-Junction Wafer-Bonded Concentrator Solar Cells,” *IEEE J. Photovoltaics*, vol. 6, no. 1, pp. 343–349, Jan. 2016.

[72] “Alta Devices Sets Solar World Record - NASA Selects Alta Devices,” *www.altadevices.com*, 2018. [Online]. Available: https://www.altadevices.com/solar-world-record-nasa-selects-alta-devices/.

[73] J. R. Woodyard Wayne and G. A. Landis, “Radiation Resistance of Thin-Film Solar Ceils for Space Photovoltaic Power,” 1991.

[74] A. T. J. van Niftrik *et al.*, “HF Species and Dissolved Oxygen on the Epitaxial Lift-Off Process of GaAs Using AlAsP Release Layers,” *J. Electrochem. Soc.*, vol. 155, no. 1, p. D35, 2008.

[75] E. Yablonovitch, T. Gmitter, J. P. Harbison, and R. Bhat, “Extreme selectivity in the lift-off of epitaxial GaAs films,” *Appl. Phys. Lett.*, vol. 51, p. 2222, 1987.

[76] M. M. A. J. Voncken, J. J. Schermer, G. J. Bauhuis, P. Mulder, and P. K. Larsen, “Multiple release layer study of the intrinsic lateral etch rate of the epitaxial lift-off process,” *Appl. Phys. A Mater. Sci. Process.*, vol. 79, no. 7, pp. 1801–1807, 2004.

[77] A. T. J. Van Niftrik, J. J. Schermer, G. J. Bauhuis, J. Van Deelen, P. Mulder, and P. K. Larsen, “The Influence of InxGa1-xAs and GaAs1-yPy Layers Surrounding the AlAs Release Layer in the Epitaxial Lift-Off Process,” *Cryst. Growth Des.*, vol. 7, no. 12, p. 2472, 2007.

[78] P. K. Larsen *et al.*, “High rate epitaxial lift-off of InGaP films from GaAs substrates,” *Appl. Phys. Lett.*, vol. 76, no. 15, pp. 2131–2133, 2002.

[79] M. M. A. J. Voncken, J. J. Schermer, G. J. Bauhuis, A. T. J. van Niftrik, and P. K. Larsen, “Strain-accelerated HF etching of AlAs for epitaxial lift-off,” *J. Phys. Condens. Matter*, vol. 16, no. 21, pp. 3585–3596, Jun. 2004.

[80] A. Rajan, R. T. Moug, and K. A. Prior, “Growth and stability of zinc blende MgS on GaAs, GaP, and InP substrates,” *Appl. Phys. Lett.*, vol. 102, no. 3, p. 32102, 2013.

[81] A. Balocchi, A. Curran, T. C. M. Graham, C. Bradford, K. A. Prior, and R. J. Warburton, “Epitaxial liftoff of ZnSe-based heterostructures using a II-VI release layer,” *Appl. Phys. Lett.*, vol. 86, no. 1, p. 11915, 2005.

[82] C. Bradford, A. Curran, A. Balocchi, B. C. Cavenett, K. A. Prior, and R. J. Warburton, “Epitaxial lift-off of MBE grown II-VI heterostructures using a novel MgS release layer,” *J. Cryst. Growth*, vol. 278, pp. 325–328, 2005.

[83] R. Moug *et al.*, “Development of an epitaxial lift-off technology for II-VI nanostructures using ZnMgSSe alloys,” *Microelectronics J.*, vol. 40, no. 3, pp. 530–532, 2009.

[84] K. A. Prior, C. Bradford, I. A. Davidson, and R. T. Moug, “Metastable II-VI sulphides: Growth, characterization and stability,” *J. Cryst. Growth*, vol. 323, no. 1, pp. 114–121, 2011.

[85] C. Bradford *et al.*, “Growth of zinc blende MgS/ZnSe single quantum wells by molecular-beam epitaxy using ZnS as a sulphur source,” *Appl. Phys. Lett.*, vol. 76, no. 26, pp. 3929–3931, Jun. 2000.

[86] A. Curran, S. Brown, R. J. Warburton, and K. A. Prior, “Determination of the etching mechanism in MgS and ZnMgSSe epitaxial lift-off layers,” *Phys. status solidi*, vol. 247, no. 6, pp. 1399–1401, Mar. 2010.

[87] A. Rajan, I. A. Davidson, R. T. Moug, and K. A. Prior, “Epitaxial lift-off of II–VI semiconductors from III–V substrates using a MgS release layer,” *J. Appl. Phys.*, vol. 114, no. 24, p. 243510, Dec. 2013.

[88] B. Seredyński, P. Starzyk, and W. Pacuski, “Exfoliation of epilayers with quantum dots,” in *Materials Today: Proceedings*, 2017, pp. 7053–7058.

[89] P. Patel, “How to Make Graphene - MIT Technology Review,” 2008. [Online]. Available: https://www.technologyreview.com/s/409900/how-to-make-graphene/.

[90] V. Ganapati, M. A. Steiner, and E. Yablonovitch, “The Voltage Boost Enabled by Luminescence Extraction in Solar Cells,” *IEEE J. Photovoltaics*, vol. 6, no. 4, p. 801, 2016.

APPENDIX A - BINARY MATERIAL PARAMETERS[21]

	InSb	CdTe	MgTe
a (nm)	0.679	0.6481	0.6420
ε	17.7	10.4	7.0
E_G (eV)	0.17	1.51	3.46
X (eV)	4.59	4.28	
c_{11} (10^{11} dyn/cm^2)	-	5.35	5.28
c_{12} (10^{11} dyn/cm^2)	-	3.69	3.66
v	-	0.408	0.409